SERDP

FINAL REPORT

Enhanced EMI Models and Systems for Underwater UXO Detection and Discrimination

Fridon Shubitidze
Dartmouth College

Benjamin Barrowes
CRREL

April 2022

SERDP Project MR-2728

REPORT DOCUMENTATION PAGE

Form Approved
OMB No. 0704-0188

1. REPORT DATE *(DD-MM-YYYY)*	**2. REPORT TYPE**	**3. DATES COVERED** *(From - To)*
12-04-2022	SERDP Final Report	6/28/2017 - 6/29/2022

4. TITLE AND SUBTITLE

Enhanced EMI Models and Systems for Underwater UXO Detection and Discrimination

5a. CONTRACT NUMBER
W912HQ-17-C-0033

5b. GRANT NUMBER

5c. PROGRAM ELEMENT NUMBER

6. AUTHOR(S)

Dr. Fridon Shubitidze
Benjamin Barrowes

5d. PROJECT NUMBER
MR-2728

5e. TASK NUMBER

5f. WORK UNIT NUMBER

7. PERFORMING ORGANIZATION NAME(S) AND ADDRESS(ES)

Dartmouth College,
Thayer School of Engineering,
14 Engineering Dr.
Hanover, NH, 03755

8. PERFORMING ORGANIZATION REPORT NUMBER

MR-2728

9. SPONSORING / MONITORING AGENCY NAME(S) AND ADDRESS(ES)

Strategic Environmental Research and Development Program
4800 Mark Center Dr, Suite 16F16
Alexandria, VA 22350-3605

10. SPONSOR/MONITOR'S ACRONYM(S)

11. SPONSOR/MONITOR'S REPORT NUMBER(S)
MR-2728SERDP

12. DISTRIBUTION / AVAILABILITY STATEMENT

DISTRIBUTION STATEMENT A. Approved for public release: distribution unlimited.

13. SUPPLEMENTARY NOTES

14. ABSTRACT

This project investigates electromagnetic induction (EMI) signals behaviors in underwater (UW) conducting environments. The analytical, numerical, and limited-experimental studies have showed that marine environments distort both the primary and secondary magnetic fields at early times/high frequencies; water-air and water-sediment boundaries produce non-negligible EMI responses; and the direct signal from the Tx current to Rx coils (i.e. salt water effects) influence a target's EMI responses disproportionately. To mitigate these effects, enhanced EMI models are developed. The enhanced models account for UW environmental effects accurately and extract target specific classification feature parameters from actual UW EMI data sets. The enhanced UW EMI data inversion and classification algorithms were applied to single-pass UltraTEMA data sets collected at Sequim Bay, WA UW calibration and blind grids. The blind grid data analyzes have showed that the enhanced EMI models can classy all detected targets of interests with high confidence.

15. SUBJECT TERMS
UXO; underwater; electromagnetic induction; forward and inverse EMI models; multi-layer; detection; classification; sensors; blind areas; saltwater.

16. SECURITY CLASSIFICATION OF:			**17. LIMITATION OF ABSTRACT**	**18. NUMBER OF PAGES**	**19a. NAME OF RESPONSIBLE PERSON**
a. REPORT	**b. ABSTRACT**	**c. THIS PAGE**			Fridon Shubitidze
UNCLASS	UNCLASS	UNCLASS	UNCLASS	124	**19b. TELEPHONE NUMBER** *(include area code)* 603-646-3671

Table of Contents

List of Figures

List of tables

List of Acronyms

AF	Air Force
cm	Centimeter
DE	Differential Evolution
EM	Electromagnetic
EMCos, LLC	Electromagnetic Consulting and Software, LLC
EMI	Electromagnetic induction
ESTCP	Environmental Security Technology Certification Program
ET	Early time
FDTD	Finite difference time domain
JD	Joint Diagonalization
LT	Late Time
μs	Microsecond
MAS	Method of auxiliary source
MHz	Mega Hertz
mm	Millimeter
MM	MetalMapper
MPV	Man-Portable Vector
ms	Millisecond
MS/S	Mega samples per second
MT	Mid-time
MuST	Multi-Sensor Towbody
NSMS	Normalized surface magnetic source
ONVMS	Orthogonal normalized volume magnetic source
ONV/SMS	Orthonormalized volume or surface magnetic source models
PNN	Probabilistic Neural Network
SERDP	Strategic Environmental Research and Development Program
TD	Time domain
TEMTADS	Time Domain Electromagnetic Towed Array Detection System
TDIM	Time Domain Image Method
UltraTEMA	Ultra transient electromagnetic Array
UXO	Unexploded ordnance
UAS	Unmanned aerial system
VET	Very early time

Executive Summary

The research described in this final report was conducted in fulfillment of Project MR-2728, "**Enhanced EMI Models and Systems for Underwater UXO Detection and Discrimination",** submitted to the Strategic Environmental Research and Development Program (SERDP) in response to Statement of Need # MRSON-17-01 Detection, Classification and Remediation of Military Munitions Underwater (UW)".

The main objective of this final report is threefold:

1. to model, analyze, and mitigate conducting environment electromagnetic responses that can affect the performance of advanced electromagnetic induction (EMI) sensor arrays in the marine environment.
2. to develop enhanced physically complete EMI models that will accurately account for EMI responses from marine environments, for UW targets detection and classification.
3. to demonstrate applicability of the enhanced model for UW targets classification by processing and analyzing UW data sets.

To achieve these objectives, first, the numerical methods, such as the unconditionally stable Crank-Nicolson finite different time domain (FDTD), the method of auxiliary sources (MAS), and a semi-analytical cylindrical plane wave expansion model are adapted to UW EMI sensing problem; then the studies are done for the primary, secondary and reflected electromagnetic fields in conducting and permeable multilayer structures; third, comparisons between modeled and experimental data sets are given for an advanced transient EMI sensor placed in marine environment; fourth, the enhanced UW transient EMI models (such as updated dipole model, transient image technique) are developed and illustrated for accurate modeling of UW geophysical data sets; and finally an EMI data set, that was collected via an advanced EMI array in the marine environment, is processed and targets classification feature parameters are extracted and analyzed.

In contrast to EMI sensing in air, the complex marine environments introduce additional EMI effects that need to be understood before EMI sensors and signal processing approaches are deployed for UW UXO detection and classification. The first effect is a change of the primary field at the receiver and at target, and a change of secondary magnetic field back to the receiver due to dispersions of transient signals in conducting media. The second is transient responses from water-air and water-sediment boundaries. The third is the EM coupling between the conductive object and the surrounding medium, including magnetic sediments. And the fourth effect is a transient response from the conducting seawater itself, i.e. direct signal from the Tx current to Rx coils. Here all these effects are analyzed using 3D EMI solvers based on the MAS, cylindrical plane wave expansion technique and FDTD methods. Namely, studies are presented for: the induced eddy currents distributions for vertical and horizontal Tx coils; the Tx coils behavior in UW environment in terms of sensor size and position; air-water-sediment effects on the EMI signals; the effects of salt water on time domain electromagnetic induction sensing of submerged metallic objects with respect to target distances and disposition on TD responses.

The analytical, numerical, and limited-experimental studies have shown: 1) marine environments distort both the primary and secondary magnetic fields at early times/high frequencies, that signal distortion is a function of separation distances between the target and the

Tx coil and between the target and observation points. As the distance between target and sensor increases, distortion of the target's EMI signals at later times is observed; 2) water-air and water-sediment boundaries produce non-negligible EMI responses, which vary with respect to the transmitter loop size, sediment conductivity and magnetic susceptibility, as well as the distances between the loop and water-air and water-sediment boundaries; 3) direct signal from the Tx current to Rx coils (i.e. salt water effects) influence a target's EMI responses disproportionately. The effects depend on the target's properties and its distance from the Tx and Rx; the comparisons between reflected (secondary) signals and the response from a conducting, permeable and non-permeable sphere/105mm projectile illustrate that the background signals (total response from layer boundaries and direct signals from Tx) are higher than the response from the sphere/projectile at early times. 4) the surrounding marine environment produces time domain EMI signals (Lenz' Law), which can outweigh the target's responses for large separations between the target and Tx/Rx. Among these effects, the distortions of the primary magnetic fields at receiver (direct coupling from Tx to Rx) have a dominant influence on the UW target's EMI responses. To mitigate these effects, enhanced EMI models are developed. The enhanced models account for UW environmental effects accurately and extract target specific classification feature parameters from actual UW EMI data sets.

The enhanced UW EMI data inversion and classification algorithms were applied to single-pass UltraTEMA data sets collected at Sequim Bay, WA UW calibration grid. First, background levels are removed from the survey line data for each time channel using detrend algorithm with 10 m window. Once EMI data are leveled, then two approaches are deployed to pick anomalies for further interrogations: (1) The traditional method that utilizes signal amplitudes on a 2D map and identifies peaks of signals above a prescribed threshold level; and (2) A semi-supervised Gaussian clustering process which clusters the inverted extrinsic (source locations) parameters into a 3D space and identifies targets using cluster centers. In the latter approach, the combined Orthogonal Normalized Volume Magnetic Source – Differential Evolution (ONVMS-DE) algorithms are applied to each dynamic data point and the intrinsic and extrinsic parameters of the anomalies extracted using a multiple source inversion approach. The calibration data analyzes have showed that the enhanced EMI models can locate and identified all TOI.

1.0 Introduction

By estimation there are approximately ten million acres of underwater areas potentially contaminated with unexploded ordnance (UXO). These lands, which are owned by the Department of Defense and the Department of Energy and have formerly been used mostly for training purposes, need to be cleaned before transferring to the public. Many active and former military installations have ranges and training areas that are adjacent to water environments such as ponds, lakes, rivers, estuaries, and oceans. In other sites, training and testing areas were deliberately situated in water environments. Disposal and accidents have also generated significant munitions contamination in the coastal and inland waters of the United States. Thus, in addition to the land based UXO, there are several million acres of underwater lands that are contaminated with UXO.

Detection and remediation of underwater UXO targets are more expensive than excavating the same targets on land. Advanced electromagnetic induction (EMI) sensors utilize multi-angle illumination of targets with 3- axis vector sensing (e.g., MetalMapper), and multi-static array sensors produce multi-sight-angle excitation (e.g., TEMTADS, BUD). Together with advanced EMI models these have provided excellent classification performance for detecting and discriminating subsurface metallic targets on land.

However, current EMI instruments, that are commonly applied to land based advanced UXO detection technologies, have been deployed for UW UXO detection and classification without considering whether to modify the associated EMI models, inversions schemes, and transmitter currents wave-forms [1]-[6]. This direct application of land-based methods to UW scenarios can lead to incorrect interpretations of UW EMI data. For example, recently, an operational marine version of the Berkeley Unexploded Ordnance Discriminator (BUD) was built and tested in shallow seawater [6] for detecting, locating, and discriminating metallic targets in an aqueous environment. Studies on land showed that the marine version of the BUD (deployed on land) was able to detect a six-inch steel test ball to over 57 cm depth and a typical 105mm UXO to over a meter and accurately recover their classification feature parameters (i.e., principal polarizabilities). In addition, these tests yielded identical transients in air and in seawater, in the absence of a target, assuring that the effects of the seawater and the air-sea interface were canceled by the BUD receiver pairs. However, results from tests for the 105 mm target in a UW environment showed that extracted extrinsic (depth and direction) and intrinsic (the principal polarizability curves) parameters, using a standard collocated orthogonal dipole model approximation, were incorrect particularly at early time gates (high frequencies). Studies under the SERDP project # MR-2409 have shown similar trends [7]. Namely, in MR-2409 project, TEMTADS data collected in a tank showed that the “noise” level in received signals is higher at early time gates when the sensor is submerged in conducting water than when it is in air. Similar results were reported for 105 mm projectile placed at 1 m below the Ultra-TEM Tx/Rx coils in the SERDP-MR-2412 project [2]. Independent in-air tests of both the marine version of BUD (MR-2321), the UW version TEMTADS and Ultra-TEM systems showed that the instruments functioned consistently and provided high quality data [8]. However, when the systems were placed in conducting environments, data quality went down, again particularly at early time gates (high frequencies). These factors (low SNR and low data quality) significantly limit the advanced EMI sensors applicability for UW target detection and discrimination. Thus, because the detection and disposal of underwater UXOs is even more expensive than similar procedures for land-based targets, the

existence of reliable detection and discrimination techniques with negligible false negatives is required before the successful cleanup of underwater contaminated areas take place.

To address these needs, the physics of EMI signals in a marine environment must be studied before deploying the current land-based EMI systems for UW-UXO detection and classification. In land based UXO detection scenarios, one or several EMI field transmitters and receivers are used to first send a magnetic field through the ground, which, being relatively unaffected by the soil, induces eddy currents in the bodies of buried metals (both UXO and clutter). During time domain EMI sensing, when the external primary magnetic field is turned off, eddy currents are generated inside conducting objects due to Lenz's law. These induced eddy currents produce secondary EMI fields, which are further registered by a set of receivers and analyzed. The physical differences between the shape and composition of the targets (volume, metal thickness, etc.) cause the different characteristics of the signals temporal decay (initial intensity, decay rate at early or late times) [15]-[16].

In the case of underwater UXO detection, it might be useful to use similar techniques with a sensor array positioned either above or below the water level. However, several factors specific to marine environments must be considered. Namely, when the advanced EMI systems are used to detect and identify a conducting and permeable compact metallic target such as (UXO) in conducting seawater, then the complex UW environment introduces additional EMI effects that are typically negligible when the target is in land soils. The first effect is a transient response from the conducting seawater itself due to eddy current and/or the direct coupling from Tx to Rx coils [1]-[8], [16]. The second is a change of the primary field at the target and a change of secondary magnetic field back to the receiver due to delays and dispersion of transient signals in conducting media [16]. The third is the EM coupling between the conductive object and the surrounding medium [16]. Studies have shown that these couplings are more significant at higher frequencies and depend on the material properties of the target, such as aluminum, steel, iron, etc. [16]. And the fourth effect is transient responses from water-air and water-sediment boundaries. It is known that vertical salinity gradients are often present in sea waters and sediments. These gradients change the EM field distribution and might affect the accuracy of target detection. In addition, the seabed properties need to be analyzed and included in the UXO detection and discrimination processes, particularly for moving underwater sensors, with continuously changing distances between the air-water and water-sediment boundaries.

2.0 Technical Objective

The technical objective of this work was to gain an understanding of the effects of conducting media on the behavior of diffusive EMI fields in the air-water-seabed environment to account for these effects in EMI data. Details for each of these objectives are provided below:

Specific technical objectives were to:

1. *Develop forward and inverse EMI models using relevant terms in the Hertzian magnetic dipole (HMD) expression to accurately account for the underlying physics of EMI fields in conducting UW environments.* One of the main reasons of success in the recent land based UXO detection and discrimination is the development of advanced, physically complete EMI models for representing subsurface metallic target responses [10]-[14]. However, all of these models were based on retaining only the near field term of the full expression for a HMD and bucking the primary magnetic field. In the case of the land-based EMI problem, fields outside of the target are considered to propagate instantaneously, without a time delay, on the scale of EMI observation. However, due to the diffusive nature of the conducting background medium, both the primary and secondary fields in a conducting medium build up gradually and propagate with a finite speed due to intermediate field effects from the HMD. Fields are now better described by the diffusion relationship in water. As a result, in a Time Domain (TD) scenario, the primary field does not fully die away as quickly as in the air after the Tx current is turned-off. Recent experimental and numerical data show [7], that this produces altered signals in the receivers at early time gates and complicates the secondary field from the target(s), likely leading to the repeatable undulations in target polarizabilities. Consequently, since early time gate signals are vital for estimating a target's location and orientation, the marine tests for the 105mm target, conducted under SERDP project MR-2321 [6], were not successful: the estimates of depth, orientation and the polarizability curves were incorrect.

2. *Research the behavior of diffusive EMI fields in the air-water-seabed environment using 3D EMI solvers based on the method of auxiliary sources (MAS) and Finite Difference Time Doman (FDTD) methods.* Here the enhanced models are applied to numerical and experimental data sets to fully quantify the updated EMI model's performance. Specifically, the enhanced models are linked to the data inversion algorithms, and robust inverse parameter regularization methodologies are created using advanced signal processing algorithms. Enhanced magnetic dipole model approximation is employed to determine the applicability of the proposed model for UW UXO detection and classification.

3. *Assess the UW target detection and discrimination capabilities (and limitations) of current advanced geophysical EMI sensors in the air-water-seabed environment using the FDTD method with a correspondence principle for wave and diffusion fields.* Under this objective, we studied how the UW environment's parameters (conductivity, magnetic susceptibility and UW conductivity gradient) impact advanced EMI geophysical (MM, TEMTADS, BUD) systems' detection and classification performances. This objective encompassed:

a. Assessing the current state of the art EMI systems for detecting and classifying UW UXO by processing existing and new SERDP-ESTCP UW data sets.
b. Identifying how the spatial and temporal variability of EMI fields in an UW environment affects EMI sensor data.
c. Researching the impact of sensor parameters (waveform, switch off time etc.) on UW EMI data. Recent experimental and theoretical studies [2],[7][16] clearly indicate that the UW environment can significantly alter a target's EMI responses, particularly at early time gates.

4. *Account for the effects of conducting media on both the primary and secondary EMI fields and the resulting data by combining a straightforward complex image method with existing advanced forward and inverse models.* The complex image method allows the use of modified, dipole like sources to quickly account for dipolar sources embedded in multilayer conductive and permeable media. We have developed and investigated the time domain image method as a possible way to retain as much model simplicity as possible while still preserving the relevant physics of the EMI scenario. The method has combined with the ONVMS method [8] by modifying the responding sources' Green's functions and incorporating this complex image method. The updated forward model has linked with direct search algorithms for extracting UW targets intrinsic (effective magnetic dipole polarizabilities) and extrinsic (locations and orientations) and surrounding medium conductivity and permeability.
5. *Compare the results of these modified methods to existing or new SERDP-ESTCP UW data sets*. Under this task, we have investigated the classification capabilities and limits of the enhanced modified forward and inverse models for UW data sets. The approach was tested against limited test-stand data set. We are planning to perform more detailed assessment of the effectiveness of the enhanced models by processing new SERDP-ESTCP UW test-stand and survey data sets.

3.0 Numerical Methods

3.1 The method of auxiliary sources for EMI problems

The method of auxiliary sources (MAS) is used to understand EMI field propagation and interaction with targets in underwater environments. The MAS is a numerical technique designed for solving various electromagnetic radiation and scattering problems. The MAS is robust, easy to implement, accurate, and has been used to investigate waveguide structures, antennas, scattering, electromagnetic wave propagation in complex media, etc. It has also been employed successfully in the analysis of low-frequency electromagnetic induction scattering phenomena [10], [11]. In the MAS, boundary value problems are solved numerically by representing the electromagnetic fields in each domain of the structure under investigation by a finite linear combination of analytical solutions of the relevant field equations, corresponding to sources situated at some distance away from the boundaries of each domain. The "auxiliary sources" producing these analytical solutions are chosen to be elementary dipoles/charges/currents located on fictitious auxiliary surface(s) that usually conform to the actual surface(s) of the structure. The method only requires points on the auxiliary and actual surfaces, so it is not necessary to resort the detailed mesh structures required by finite-element and boundary-element methods. The two auxiliary surfaces are set up inside and outside the penetrable scattering object. The fields outside of the structure are considered to originate from a set of auxiliary sources placed inside the object, while the fields inside the object are taken to arise from a set of auxiliary sources placed outside. The interior and exterior fields thus constructed are required to obey Maxwell's boundary conditions the continuity of the tangential magnetic field and the jump condition for the normal magnetic field at arrays of selected points on the physical surface(s) of the structure. This results in a matrix equation in which the amplitudes of the auxiliary sources are the unknowns. Once these amplitudes are found, the electromagnetic field as well as any quantity related to it can easily be computed throughout the computational space.

EMI scattering responses are usually expressed in terms of the induction number $\chi \sim a/d$, where d [m] is the skin depth and a [m] is a characteristic dimension of the object. It is well established that the electromagnetic field inside a conductor decays over distances of the order of the skin depth. This reduces the efficiency and accuracy of the MAS at high induction numbers due to singularities that appear in the scattering matrix. To overcome this problem, a combined MAS-thin skin approximation (MAS-TSA) [12], [14] based on the divergence-free Maxwell's equation for the magnetic field was developed and used to solve a variety of EMI problems from the magnetostatic regime up to 1 MHz for land-based UXO detection and discrimination. The TSA assumption, however, is found to break down when targets are placed in conducting media because satisfaction of the divergence-free equation is not sufficient to guarantee that all necessary boundary conditions for electric and magnetic fields are obeyed. We have overcome this difficulty by employing the surface impedance boundary condition (SIBC).

The SIBC is based on the fact that the electromagnetic fields and currents within the conductor are confined to a very thin surface layer. The model assumes that the EM field decays exponentially normal to the surface within a metallic object. Within the conductor, specific components of the field are related by Maxwell's equations. For example, a relationship between the components of **E** and **H** tangential to the surface can be written as

$$\mathbf{E}_t = [-(1+j)\delta/\sigma]\,\hat{\mathbf{z}}\times\mathbf{H}_t \tag{1}$$

where the subscript *t* indicates the component tangential to the surface of the conductor, $j=\sqrt{-1}$ is the imaginary unit, σ is conductivity and δ is skin depth. With $\hat{\mathbf{n}}=-\hat{\mathbf{z}}$ the outward pointing unit vector normal to the surface, $\mathbf{E}_t = -\hat{\mathbf{n}}\times(\hat{\mathbf{n}}\times\mathbf{E})$ and (1) becomes

$$\hat{\mathbf{n}}\times(\hat{\mathbf{n}}\times\mathbf{E}) = [-(1+j)\delta/\sigma]\,\hat{\mathbf{n}}\times\mathbf{H}\,. \tag{2}$$

This is the SIBC for highly conducting metallic objects. Equation (2) is solved using the MAS.

3.2 Models for representing targets EMI signals

During electromagnetic induction sensing, a time varying magnetic field illuminates a target. The primary magnetic field penetrates inside any conducting and/or permeable object (or medium) and induces eddy currents within it. The induced eddy currents produce a secondary field that is measured external to the object at the receiver coil. The electromagnetic data are then inverted in the sense that the mismatch between the measured and modeled data is minimized, indicating which model parameters and characteristics apply. In the case of discrete, metallic targets in air there are several forward EMI models for representing a target's EMI responses [17]-[20]. All these models use the simple magnetic dipole model approximation as the base model but utilize different variations. When the intervening medium between the Tx and Rx is itself conducting (and therefore diffusive), the water acts like a large "target" with the secondary field from the water and discrete metal target(s) interacting in complex ways. As a result, the simplest dipole model approximation should not be applied in UW-based surveying and analysis. To illustrate how this breaks down when placed in a conducting, diffusive medium such as water, let us consider the complete, rigorous expression for a single magnetic dipole model in an arbitrary homogeneous environment. The magnetic field **H** (A/m) due to an infinitesimal magnetic dipole **m** is

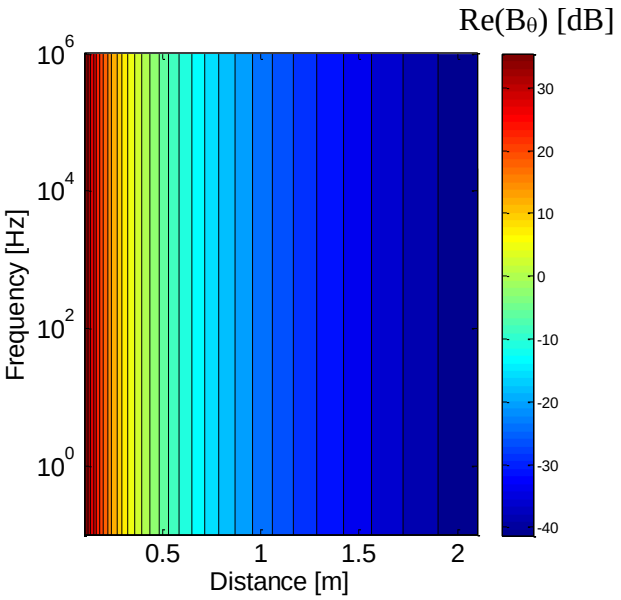

Figure 1. $B_\theta = \mu\mu_o H_\theta$ due to a magnetic m_z dipole in air k=0 as a function of frequency (y-axis) and distance (x-axis). The dipole is placed at the origin and distance is measured along x-axis.

$$\mathbf{H} = \frac{e^{-ikR}}{4\pi R^3}\left[\left(\frac{3\mathbf{R}(\mathbf{R}\cdot\mathbf{m})}{R^2}-\mathbf{m}\right)(1+ikR)-k^2\left(\mathbf{R}\times(\mathbf{R}\times\mathbf{m})\right)\right], \tag{3}$$

where **R = r** – $\mathbf{r}_d$, and the vectors **r** and $\mathbf{r}_d$ are the observation point and the location of the dipole ([16]**).** $k = \sqrt{\omega^2 \mu_o \varepsilon_o \varepsilon\mu + i\sigma\omega\mu\mu_o}$ is the wave number in the surrounding diffusive/conducting medium; σ (S/m) is the medium's conductivity, $\varepsilon_o = 8.85 \cdot 10^{-12}$ (F/m) and $\mu_o = 4\pi \cdot 10^{-7}$ (H/m) are the permittivity and permeability of free space, respectively, while ε_r and μ_r are relative permittivity and permeability, respectively; $\omega = 2\pi f$ is circular frequency. Note that, in the electromagnetic wave or diffusive regime, the magnetic field due to a magnetic dipole has terms that decay as R^{-1}, R^{-2}, and R^{-3}. The range $kR \gg 1$ is referred to as the far field zone, and fields in this range are referred to as being in the far field. Similarly, fields in the near zone (with $kR \ll 1$) are referred to as being in the near field, while the zone $kR \approx 1$ is called the intermediate zone. In the EMI regime, displacement currents are considered irrelevant.

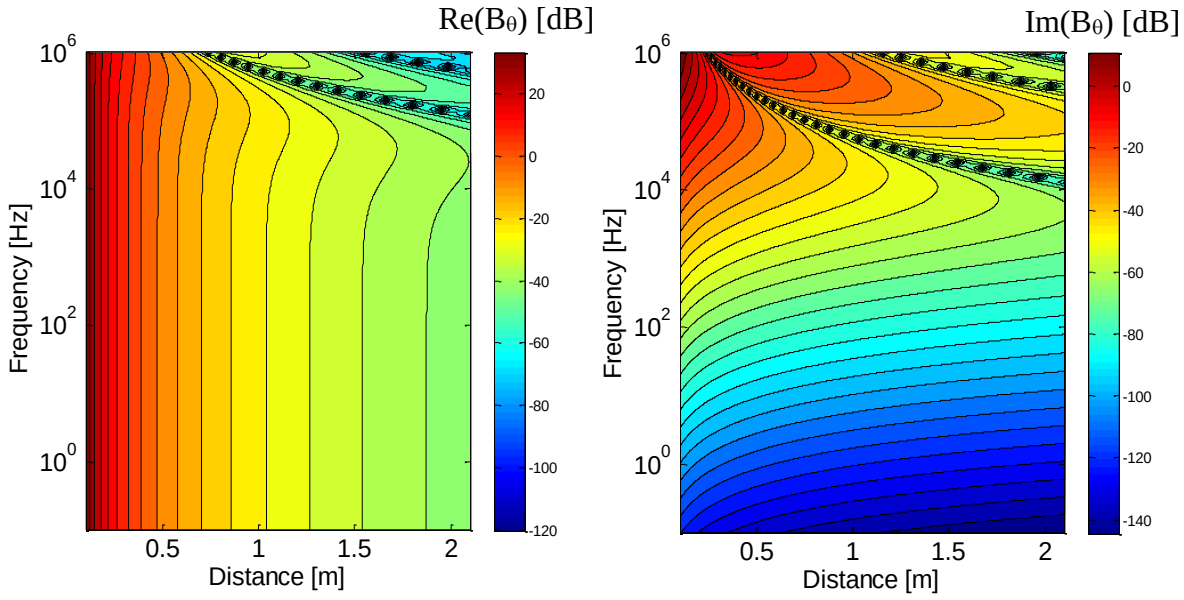

Figure 2. Inphase (left) and Quadrature (right) parts of B_θ ($= \mu\mu_0 H_\theta$) due to a magnetic m_z dipole placed in (s = 4 S/m) as a function of frequency (y-axis) and distance (x-axis). The dipole is placed at the origin and distance is measured along the x-axis.

For land based UXO classification problem one may assume that $k \approx 0$, and from eq (3) the magnetic field due to a dipole **m** is approximated as

$$\mathbf{H}(\zeta) = \bar{\bar{\mathbf{G}}} \cdot \mathbf{m}(\zeta) \tag{4}$$

where $\bar{\bar{\mathbf{G}}} = \frac{1}{4\pi R^3}\left(3\hat{\mathbf{R}}\hat{\mathbf{R}} - \bar{\bar{\mathbf{I}}}\right)$ is a dyadic Green's function, $\zeta = t$ or f is time or frequency, $\mathbf{m}(\zeta) = \bar{\bar{\mathbf{M}}}(\zeta)\cdot\mathbf{H}_0$, where $\bar{\bar{\mathbf{M}}}(\zeta)$ is the target's polarization tensor, and $\mathbf{H}_0$ is the primary magnetic field. The component of the magnetic field $H_\theta(t)$ in a spherical coordinate system for a m_z dipole with the current consisting of a rectangular pulse ($m_z(t)$=0 for t<0, $m_z(t) = J$ for 0<t<T and $m_z(t)$=0 for t>T; T is pulse width) is:

$$H_\theta(t) = \frac{\sin\theta}{4\pi R^3} m_z(t) \tag{5}$$

During land-based UXO detection and classification only the near field zone is considered, and signals from transmitters to a target and from targets to receivers are propagated without any dispersion/diffusion, on the time scale of relevant observation. This is the model that has been applied to date in UXO discrimination. Figure 1 shows the pattern of response when such a simple dipole source resides in a non-conducting environment. Figure 2 shows the changes that are wrought when the same dipole is placed in an environment with the conductivity of sea water. In a frequency and distance range of key concern for UXO discrimination, substantial distortions appear relative to the regular pattern in Figure 1. In particular, changes appear in both the in-phase and quadrature components of the magnetic field at crucial frequencies, between about 10 KHz and the upper EMI limits. Expressing this in other terms emphasizes how the fields from our source in sea water will vary, relative to the simpler picture that applies on land, according to frequency, observation point r, field component and direction. On the left in Figure 3, the results at the lowest frequencies (lowest *k* values) resemble those familiar from non-conducting media: modest

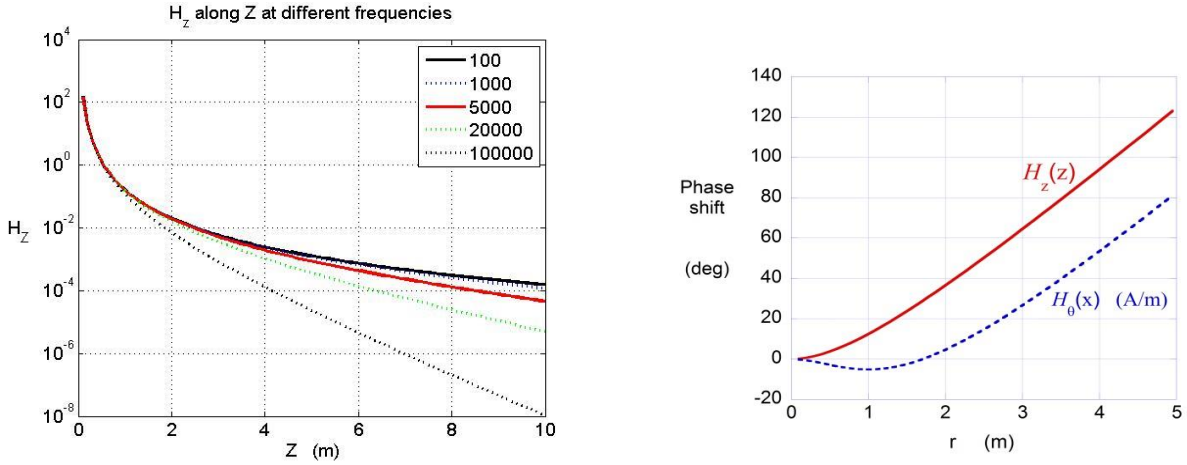

Figure 3. Left: Analytical $|H_z|$ values from a vertical magnetic dipole at the origin in seawater, at the indicated frequencies (in Hertz), evaluated along the Z axis. Right: Phase shift relative to the source, at 20 kHz, for H_θ along the X axis, where $H_\theta = -H_z$.

changes in frequency do not affect the field distribution, which is dominated by the $\left(1/R^3\right)$ dependence. In higher frequency ranges, this term still dominates in the region near the source. Farther away from the source, however, the other inverse-power terms come into play, affecting the slope of each curve differently; and ultimately, at the greatest distances, the exponential factor dominates. Variations in the field's phase may be even more consequential for modeling and processing than those of its magnitude (Figure 3, right). The finite time required for field diffusion through the conducting medium causes large phase shifts, relative to the timing of the source. Higher frequencies will produce larger and more rapid variations than those in the figure, lower frequencies less. All these effects are doubly significant, so to speak, in that they apply to fields from targets as well as from transmitters. From the point of view of modeling and processing, this heterogeneity in the field and its dependencies constitutes a radical change relative to the non-conducting world.

3.3 Enhanced transient EMI models for UW targets detection and classification.

Most, if not all, advanced land based UXO detection and classification geophysical electromagnetic systems operate in time domain. The systems consist a set of multiple transmitters and 3d receivers. Throughout subsurface target sensing, the currents are turned on and off abruptly in the transmitter coils periodically. During the turned-on period, the transmitter currents are raised abruptly and kept constant for a short time interval (typically 2.7 msec, or 8 msec, or 25 msec). The currents produce primary electromagnetic fields, which penetrates inside conducting environment. After the short time interval the currents are turned-off abruptly and as a result, according to Lentz's law, transient eddy currents (magnetic dipoles) are induced in the conducting medium. Thus, for practicality it is more convenient to derive eq. (3) in time domain for both primary and secondary EM signals in UW environment. To do so, let us derive the complete transient electromagnetic response of a magnetic dipole place in a conducting space. In the EMI regime the displacement current ($\mathbf{J} = i\omega\varepsilon\varepsilon_o\mathbf{E}$) is negligible compared to the conduction current $\mathbf{J} = \sigma\mathbf{E}$, and the wavenumber k is purely imaginary, $k = \sqrt{i\sigma\omega\mu\mu_o}$. Let us introduce a complex variable *s,* as $s = i\omega$. After replacing $i\omega$ with *s* in the equation (3), the transient magnetic field response h(t) of a constant **m** magnetic dipole after it is turned off can be calculated using the inverse (L^{-1}) Laplace transform, [13], as

$$\boldsymbol{h}(t) = L^{-1}\left[\frac{\mathbf{H}(s)}{s}\right], \tag{6}$$

following the substitution **H**(s) from eq. (3) into eq. (6) and applying the inverse Laplace transforms to three e^{-ikR}/s, $ikR\,e^{-ikR}/s$, and $k^2R^2\,e^{-ikR}/s$ yields,

$$\mathbf{h}(\mathbf{r},\mathbf{r}',t) = \bar{\bar{\mathbf{G}}}(\mathbf{r},\mathbf{r}',t)\cdot\mathbf{m}, \tag{7}$$

where

$$\bar{\bar{\mathbf{G}}}(\mathbf{r},\mathbf{r}',t) = u(t)\left(g_o(\mathbf{r},\mathbf{r}',t)\;\mathbf{R}\mathbf{R}^T - \bar{\bar{I}}\;g_1(\mathbf{r},\mathbf{r}',t)\right);$$

$$g_o(\mathbf{r},\mathbf{r}',t)=\frac{1}{4\pi R^5}\left[\frac{\theta R}{\pi^{1/2}}\left(4\theta^2R^2+6\right)e^{-\theta^2R^2}+3erfc(\theta R)\right] \tag{8}$$

$$g_1(\mathbf{r},\mathbf{r}',t)=\frac{1}{4\pi R^3}\left[\frac{2\theta R}{\pi^{1/2}}\left(2\theta^2R^2+1\right)e^{-\theta^2R^2}+erfc(\theta R)\right]$$

$u(t)$ is step function, i.e $u(t)=0,$ when t<0; $u(t)=1,$ when $t\geq 0$, $R=|\mathbf{R}|=|\mathbf{r}\text{-}\mathbf{r}'|$ is the distance between the magnetic **m** dipole $\mathbf{r}'$ position and **r** observation points, $\bar{\bar{I}}$ is the 3x3 identity matrix and $\theta=\left(\frac{\sigma\mu_r\mu_o}{4t}\right)^{1/2}$, σ (S/m) and $\mu_o\mu_r$ are the medium's conductivity and magnetic permeability, respectively, t -is time, and finally *erfc* is the complementary error function. For a general transient general magnetic dipole **m**(t) moment the transient magnetic field can be calculated as,

$$\mathbf{H}(\mathbf{r},\mathbf{r}',t)=\int_0^t\bar{\bar{\mathbf{G}}}(\mathbf{r},\mathbf{r}',t\text{-}\tau)\cdot\ \mathbf{m}(\tau)\,d\tau\ . \tag{9}$$

For the EM diffusion problem considered here, $\mathbf{m}(t)=\mathbf{m}(t)\left(1\text{-}u(t)\right)$ is a causal function. Note, that there is no time delay during diffusion, and the tensor Green's function $\bar{\bar{\mathbf{G}}}(\mathbf{r},\mathbf{r}',t\text{-}\tau)$ is just a shift of the fundamental solution for the initial problem at t=0 to the new starting time at $t=\tau$. The same time shift is applied to the magnetic dipole moment $\mathbf{m}(\tau)$. In addition, since $\bar{\bar{\mathbf{G}}}(\mathbf{r},\mathbf{r}',t)$ and $\mathbf{m}(t)$ are positive and negative causal functions, respectively. Therefore, applying convolution theorem to (9) yields that the magnetic field of the transient magnetic dipole is

$$\mathbf{H}(\mathbf{r},\mathbf{r}',t)=\bar{\bar{\mathbf{G}}}(\mathbf{r},\mathbf{r}',t)\cdot\ \mathbf{m}(t)\ . \tag{10}$$

Usually throughout transient electromagnetic sensing, we measure the electromotive force (emf), which is proportional to the time derivative of the secondary magnetic field at a receiver coil. Thus, taking the time derivative of equation (10) we obtain

$$\frac{\partial\mathbf{H}(\mathbf{r},\mathbf{r}',t)}{\partial t}=\bar{\bar{\mathbf{G}}}(\mathbf{r},\mathbf{r}',t)\cdot\ \frac{\partial\mathbf{m}(t)}{\partial t}+\frac{\partial\bar{\bar{\mathbf{G}}}(\mathbf{r},\mathbf{r}',t)}{\partial t}\cdot\ \mathbf{m}(t) \tag{11}$$

From equation (7) after some mathematical derivations the $\frac{\partial\bar{\bar{\mathbf{G}}}(\mathbf{r},\mathbf{r}',t)}{\partial t}$ term can be written as

$$\frac{\partial \bar{\bar{\mathbf{G}}}(\mathbf{r},\mathbf{r}',t)}{\partial t} = \left(g_o^{'}(\mathbf{r},\mathbf{r}',t)\ \mathbf{RR}^T - \bar{\bar{I}}\ g_1^{'}(\mathbf{r},\mathbf{r}',t) \right) u(t) \tag{12}$$

$$g_o^{'}(\mathbf{r},\mathbf{r}',t) = \frac{\theta^5}{\pi^{3/2} t} e^{-\theta^2 R^2}$$

$$g_1^{'}(\mathbf{r},\mathbf{r}',t) = \frac{\theta^3}{\pi^{3/2} t} e^{-\theta^2 R^2} \left(1 - \theta^2 R^2\right)$$

Note that in case of a land based UXO detection and classification problem we assume that conductivity of soil σ ~0 [S/m], i.e. ($\theta \rightarrow 0$), $\frac{\partial \bar{\bar{\mathbf{G}}}(\mathbf{r},\mathbf{r}',t)}{\partial t} \rightarrow 0$ and equation (11) reduces to

$$\frac{\partial \mathbf{H}(\mathbf{r},\mathbf{r}',t)}{\partial t} = \frac{1}{4\pi R^3} \left(3\hat{\mathbf{R}}\hat{\mathbf{R}} - \bar{\bar{\mathbf{I}}} \right) \cdot \frac{\partial \mathbf{m}(\mathrm{t})}{\partial t}. \tag{13}$$

The eq. (13) is used for the land based UXO classification problems. Thus, in a conducting environment the transient magnetic **m**(t) dipole produces emf, which is the sum of *emf*-s due to the derivative of magnetic dipole and the dipole moment itself.

To demonstrate differences between the enhanced eq. (11) and old eq. (13) models, the magnetic fields derivatives were calculated at a set of observation points for the vertical $\mathbf{m}(t) = \hat{\mathbf{z}}\ \mathrm{m}_o(\mathrm{t})$ and $\mathbf{m}(t) = \hat{\mathbf{x}}\ \mathrm{m}_o(\mathrm{t})$ dipoles, where the $\mathrm{m}_o(\mathrm{t})$ is magnetic dipole moment is taken for a nonpermeable, $\sigma = 5 \cdot 10^7 [S/m]$ conductive, 10 cm radius sphere placed in a uniform transient magnetic field, as derived by Wait in [38], equation #18. Figure 4 and Figure 5 show comparisons between time derivatives of magnetic fields (i.e. induced *emf*) calculated using the old and enhanced models for the horizontal and vertical **m**(t) magnetic dipoles, respectively, at different observations points. The shaded areas correspond to the current advanced EMI sensors operating time window. The results show that when the observation point is close to the magnetic dipole (**top rows:** Figure 4 and Figure 5), the time derivatives of magnetic fields produced only by $\frac{\partial \mathbf{m}(\mathrm{t})}{\partial t}$ (old model see eq. (13)) and combined $\bar{\bar{\mathbf{G}}}(\mathbf{r},\mathbf{r}',t) \cdot \frac{\partial \mathbf{m}(\mathrm{t})}{\partial t}$ and $\frac{\partial \bar{\bar{\mathbf{G}}}(\mathbf{r},\mathbf{r}',t)}{\partial t} \cdot \mathbf{m}(\mathrm{t})$ terms are identical in the current advanced EMI sensors operating time window. As the separation between the magnetic dipole and observation points increases, then there are observable contributions from the magnetic dipole(**m**(t)) i.e. $\frac{\partial \bar{\bar{\mathbf{G}}}(\mathbf{r},\mathbf{r}',t)}{\partial t} \cdot \mathbf{m}(\mathrm{t})$ term before and near 10^{-4} (sec) (EMI sensors operating early time), see Figure 4 and Figure 5: middle and bottom rows. The similar trends were observed numerically as well experimentally in MR-1632, MR-2412 and MR-2409 projects in both time and frequency domains.

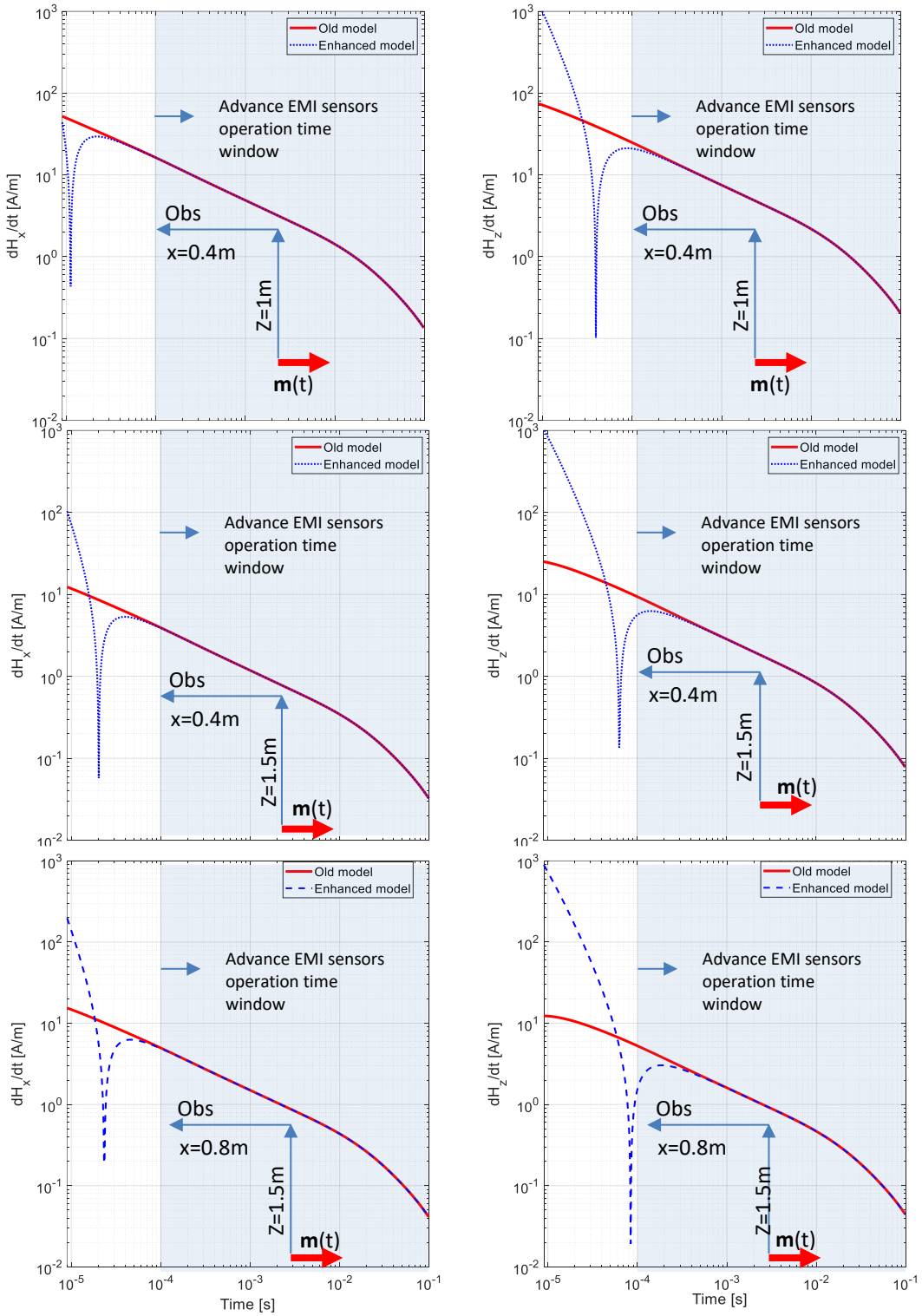

Figure 4. Comparisons between calculated time derivatives of magnetic fields for a horizontal, $\mathbf{m}(t) = \hat{\mathbf{x}}\, m_o(t)$, magnetic dipole using the old (red solid lines) eq. (13) and enhanced (blue dashed lines) eq.(11) models at observation points: Top row- x=0.4m, y=0,z=1m; middle row- x=0.4m, y=0,z=1.5m; bottom row- x=0.8m, y=0,z=1.5m. Left column: time derivative of H_x and right column: time derivative of H_z.

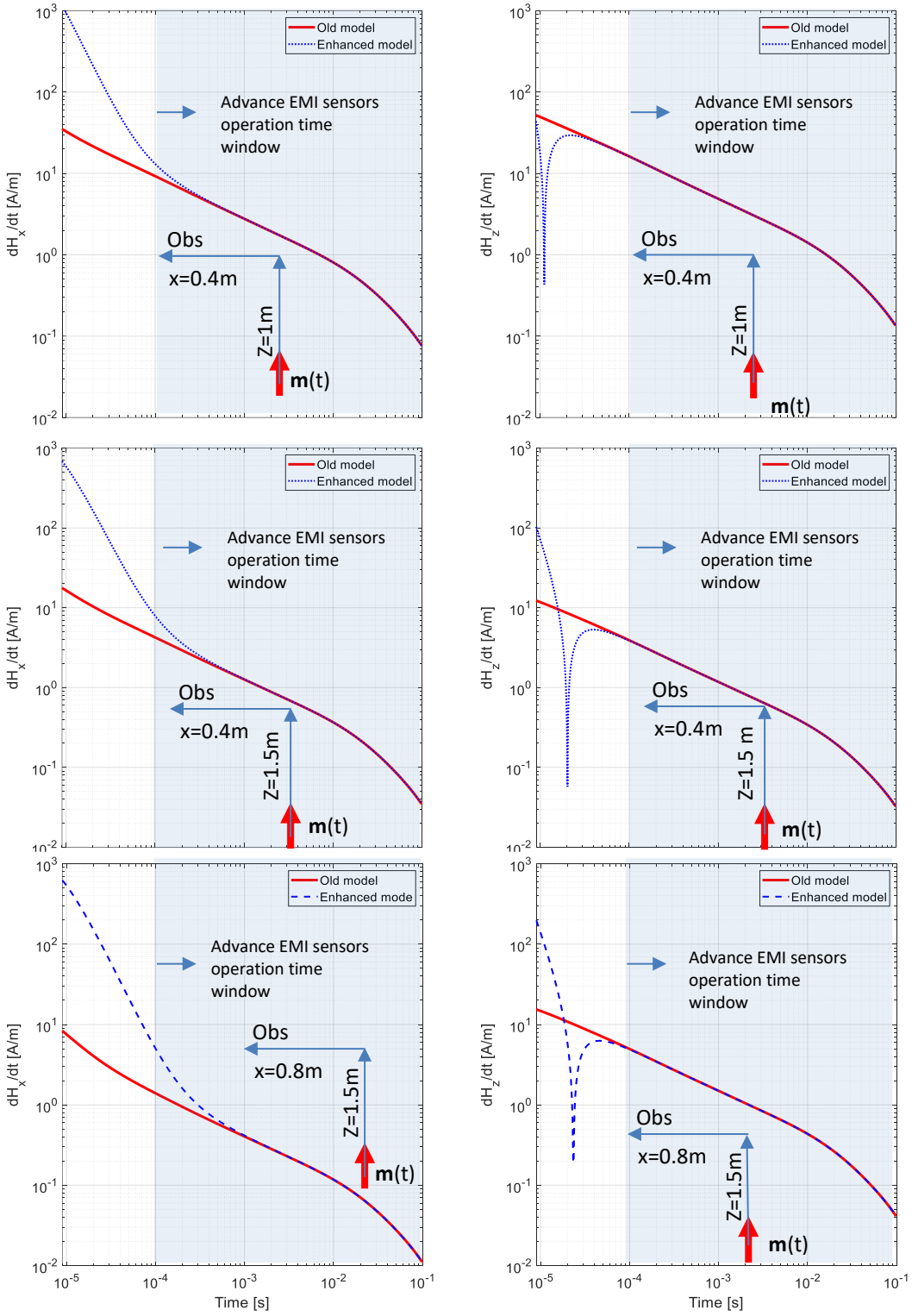

Figure 5. Comparisons between calculated time derivatives of magnetic fields for a vertical, $\mathbf{m}(t) = \hat{\mathbf{z}}\ \mathrm{m}_o(\mathrm{t})$, magnetic dipole using the old (red solid lines) eq. (13) and enhanced (blue dashed lines) eq.(11) models at observation points: Top row- x=0.4m, y=0,z=1m; middle row- x=0.4m, y=0,z=1.5m; bottom row- x=0.8m, y=0,z=1.5m. Left column: time derivative of H_x and right column: time derivative of H_z.

The contribution of the magnetic dipole(**m**(t)) , see eq. (11) second term, is significantly higher at earlier times $<10^{-4}$ (sec) compared to magnetic fields derivatives produced by the first term of eq. (11) right side i.e. $\bar{\bar{\mathbf{G}}}(\mathbf{r},\mathbf{r}',t)\cdot\frac{\partial \mathbf{m}(t)}{\partial t}$. Namely, calculations show that the induced *emf* ($\frac{\partial H_x}{\partial t}$ and $\frac{\partial H_z}{\partial t}$) calculated using all parts of eq. (11) are about 100 times higher than the *emf* produced by the first term of the eq. (11) right side. Utilizing this enhancement EMI signal's strength could increase targets detection depth at least twice, which will be a significant improvement for UW UXO detection and classification using EMI systems.

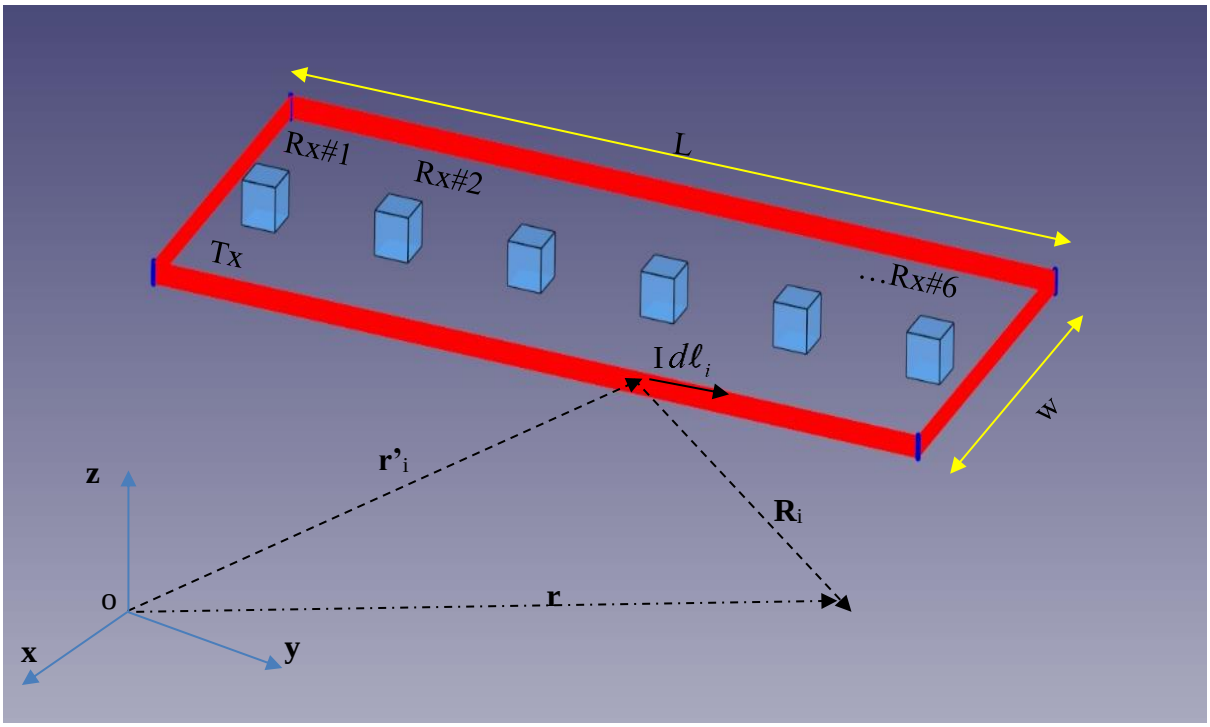

Figure 6. A schematic diagram of a UW Tx/Rx system. The observation point r is defined with respect to the global Cartesian coordinate system XYZO; $\mathbf{r}_i'$ is the location of the *i*-th current element on the transmitter, which carries a current I in the direction $d\ell_i$.

3.4 Primary electromagnetic fields in UW environment:

Under various SERDP-ESTCP programs several advanced EMI systems have been deployed and tested for UW UXO detection and discrimination [1], [2], [8], [9]. These systems have multiple transmitter loops, which generate the primary electromagnetic fields periodically by turning on and off currents. The primary magnetic fields impinge targets from different directions/sides depending on the Tx loops configuration geometry and the distance between a particular transmitting loop and the target. The primary electromagnetic field diffuses into the conducting medium and target, and, in accordance with Faraday's law, induces eddy-currents and/or magnetic dipoles within conductors. The strength and diffusion speed of the primary magnetic field depend on the magnitude of the transmitter current and conductivity of the medium, respectively.

The time harmonic primary magnetic produced by a UW Tx coil at any observation point **r** in a conducting environment, see Figure 6, is

$$\mathbf{B}^{pr}(\mathbf{r},\omega)=\oint_L \frac{I\mu_o}{4\pi R^3}(ikR+1)e^{-jkR}\left(d\vec{\ell}\times\mathbf{R}\right) \tag{14}$$

Where again **R=r-r'** is the distance between **r** observation and **r'** source points, k is wave number in conducting environment, I is the current Tx coil; $d\vec{\ell}$ is a vector tangential to the wire. After applying the inverse Laplace transforms to the equation (14) yields, the abruptly turned on (or off) primary magnetic field can be expressed as

$$\mathbf{B}^{pr}(\mathbf{r},t)=L^{-1}\left[\frac{\mathbf{B}^{pr}(\mathbf{r},s)}{s}\right]=\frac{I\mu_o}{4\pi}\oint_L\left(ercf(\theta R)+\frac{2}{\pi^{1/2}}\theta e^{-\theta^2R^2}\right)\left(\frac{d\vec{\ell}\times\mathbf{R}}{R^3}\right) \tag{15}$$

For calculating the primary magnetic field produced by a Tx loop at any observation point **r** and at any time t, the loop is divided into subsections and the closed integral in eq (15) is approximated as,

$$\mathbf{B}^{pr}(\mathbf{r},t)=\frac{I\mu_o}{4\pi}\sum_{i=1}^{N_{Tx}}\left(ercf(\theta R_i)+\frac{2}{\pi^{1/2}}\theta e^{-\theta^2R_i^2}\right)\left(\frac{\Delta\vec{\ell}_i\times\mathbf{R}_i}{R_i^3}\right), \tag{16}$$

where, $\mathbf{R}_i=|\mathbf{r}-\mathbf{r}_i'|$, $\mathbf{r}_i'$ is the location of the *i*-th current element, and $\Delta\ell_i$ is the tangential length vector for the *i*-th subsection of the loop. In what follows, and unless we note otherwise, we divide each transmitter coil into $N_{Tx}=50$ subsections whenever we calculate the primary magnetic induction using Eq. (16).

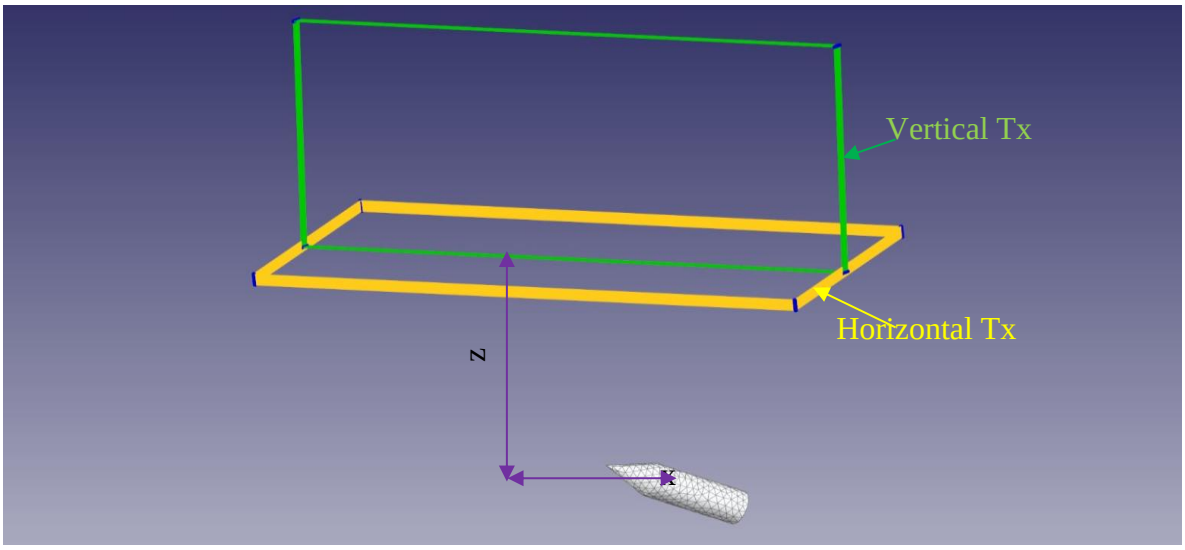

Figure 7. Sketch of a 3D Tx system for UW UXO targets interrogation.

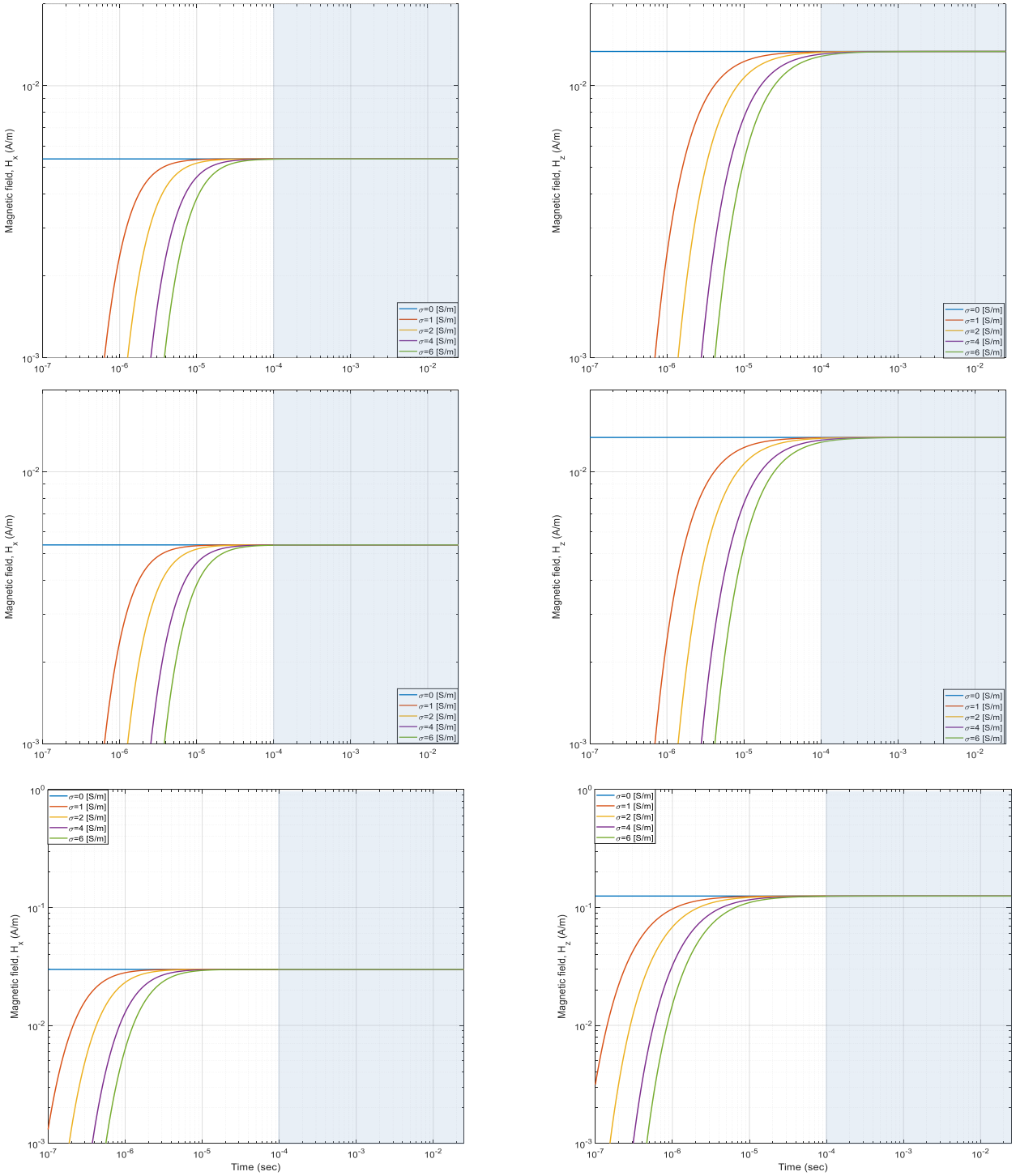

Figure 8. Primary magnetic field vs time for horizontal Tx coil placed in free space and in a different conducting medium, see Figure 7. Left column for H_x field, Right column H_z field. Fields are calculated: top row -at x=0.4 m, z=1 m; middle row x=0.4 m, z=1.5 m; bottom row x=0.8 m, z=2.5 m. Shaded areas correspond to current EMI system operating time window.

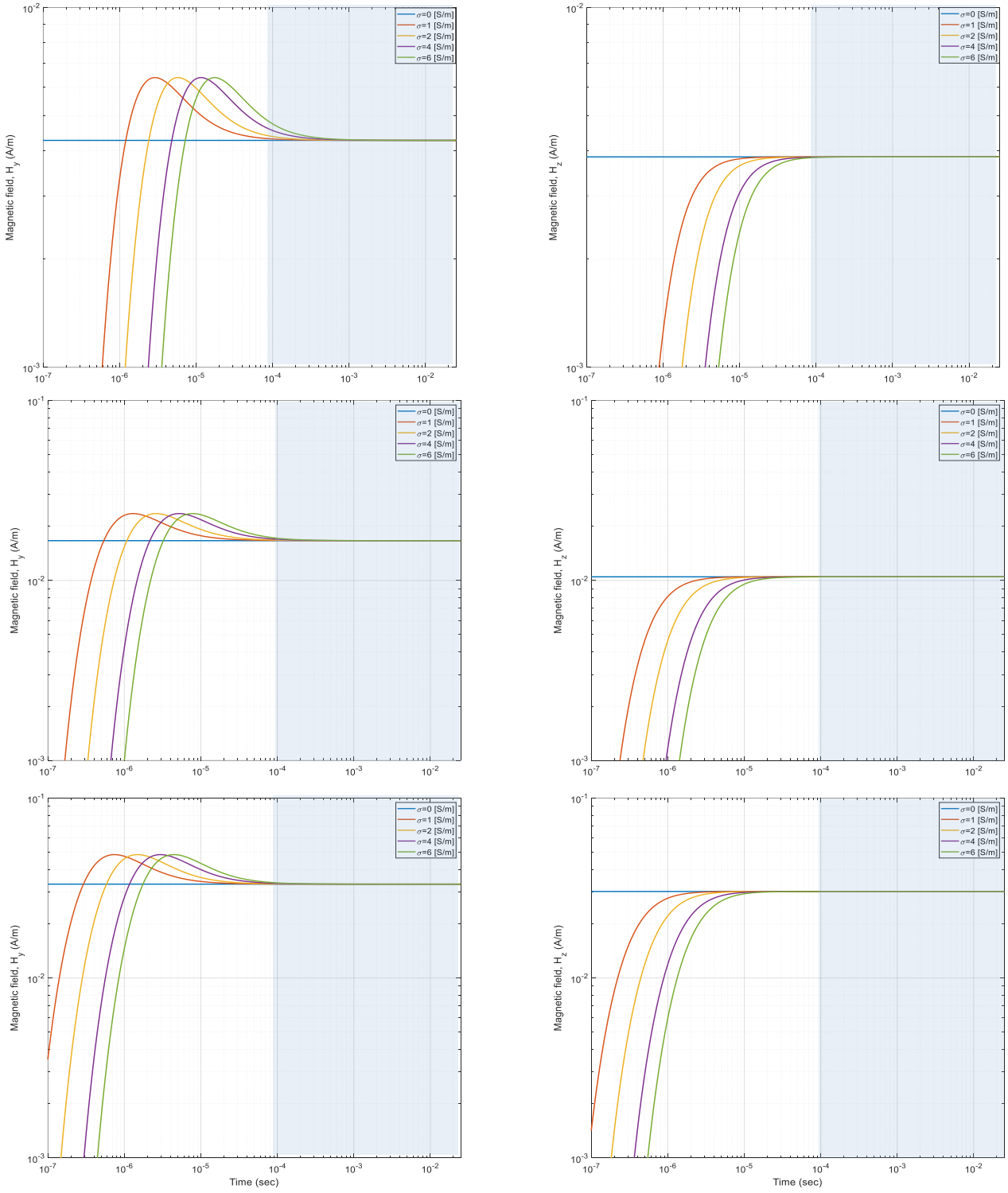

Figure 9. Primary magnetic field vs time for vertical Tx coil placed in free space and in a different conducting medium, see Figure 7. Left column for H_x field; Right column H_z field. Fields are calculated: top row -at x=0.4 m, z=1 m; middle row x=0.4 m, z=1.5 m; bottom row x=0.8 m, z=2.5 m; Shaded areas correspond to current EMI system operating time window.

To demonstrate how conducting environments influence the primary magnetic fields, Figure 8 and Figure 9 show the primary magnetic fields vs time at a set of (x, y=0, z) observation points for a horizontal and vertical 2 m x1m size Tx coils. The Tx coils were placed in the free space ($\sigma = 0$ [S/m]) and in medium with $\sigma = 1, 2, 4$ and 6 [S/m] conductivity. Figure 8 shows calculated H_x and H_z the primary magnetic field components at: top row x=0.4 m, z=1 m; middle row x=0.4 m, z=1.5 m; bottom row x=0.8 m, z=2.5 m locations. These results show that at later time (>10^{-4} sec, shaded areas) the primary magnetic in free space and in conducting medium are identical, where-else at earlier time the fields in conducting medium differs from field in the free space, and these differences are a function of medium conductivity. In addition, both H_x and Hz components of the primary magnetic fields have the similar time dependents. Figure 9 shows calculated H_y and H_z components of the primary magnetic field for the vertical Tx loop at the same observation points: top row x=0.4 m, z=1 m; middle row x=0.4 m, z=1.5 m; bottom row x=0.8 m, z=2.5 m locations. These results show the same trends as for the horizontal Tx coils, namely at later time (>10^{-4} sec, shaded areas) the primary magnetic in the free space and in a conducting media are identical, where-else at earlier time the fields in conducting medium differs from free space field. One distinguishable observed phenomenon here is the that the calculated H_y component's time dependence differs from the H_z component. At early time, the H_y component of the magnetic field has a pick, which is higher than the same field in the free space. Although, at early times in the short time window UW targets experience much less energy than the same targets in free space, our simulations show that these differences have negligible effect on the induced dipole moment distribution inside the target, particularly at later times. The is due to indistinguishable differences between the primary magnetic field in the free space and in conducting medium for the current EMI systems operating time widow (shaded areas).

3.5 Eddy currents in a conducting medium

In transient electromagnetic sensing, the primary electromagnetic field diffuses inside conducting medium and induces eddy-currents **J** within it. The eddy currents $\mathbf{J}=\sigma\mathbf{E}$, that are proportional to the electric **E** field and conductivity of medium, produce secondary electromagnetic fields. As a result, the secondary fields are mixed with targets EMI responses and produce additional unwanted *emf* in receive coils. To understand and mitigate the eddy current response, here we present electric field distributions in a conducting medium versus time and space. Namely, the electric fields are calculated along lateral distance and depth for a horizontal 2m x1 m Tx coil placed in the σ=6[S/m] conductive medium, Figure 10, Using eq. (17). Using the analogous relations between the magnetic and electric dipoles and eq. (10), the electric field of Tx loop in a medium with conductivity σ can be expressed as,

$$\mathbf{E}^{pr}(\mathbf{r},t) = \frac{I}{\sigma}\sum_{i=1}^{N_{Tx}} \overline{\overline{\mathbf{G}}}\ (\mathbf{r},\mathbf{r}_i,t)\cdot\Delta\vec{\ell}_i\,, \tag{17}$$

Where the tensor Greens function $\overline{\overline{\mathbf{G}}}\ (\mathbf{r},\mathbf{r}_i,t)$ is given in eq. (8).

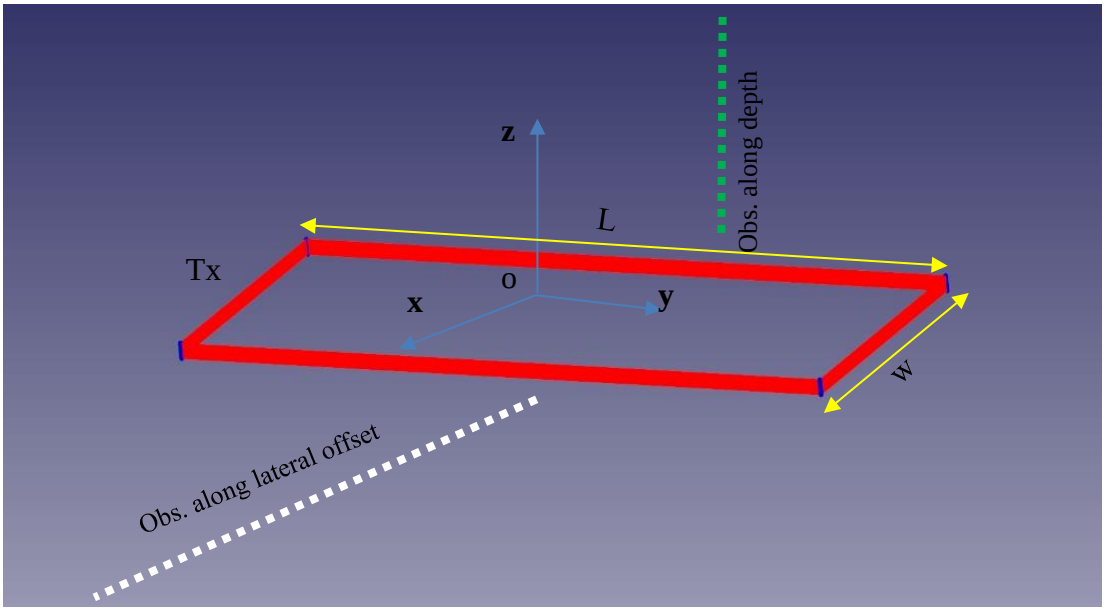

Figure 10. A schematic diagram for electric field calculation conducting environment.

Figure 11 shows electric fields vs time along lateral (left) and vertical (right) offsets for horizontal Tx coil in 6 S/m conducting medium. The center of the coordinate system coincides with the Tx coil's center. Figure 11-left is for fixed z=1 m and Figure 11-right is for fixed x=-1m, y=0m. These results show that: 1. the electric field produced by horizontal Tx coils diffuses slowly in both lateral and vertical directions; 2. the conductive medium delays and broadens electric field distributions.

The maximum of the electric field, that forms a "smoke ring", occurs at $t = \frac{R^2 \mu_o \sigma}{10}$. Although, at later time the electric field approaches to $t^{-5/2}$ decays in both directions, their magnitudes change differently along vertical and horizontal directions. Namely, at later time the electric field along vertical offset (depth) approaches to a constant value, where-else along the lateral direction the magnitude of the field increases as the distance from the Tx increases. This sensitivity of the electric field magnitude in the lateral direction can influence the background removal process and must be consider during transient UW electromagnetic data processing and inversion.

Figure 12 illustrates further how the maximum of the electric field (eddy-current) moves along lateral and vertical offsets for a 2m x1 m Tx coil in a conducting medium. On Figure 12 $R = \sqrt{x^2 + z^2}$. On the Figure 12 left: y-is distance along lateral offset and z=1m; and on Figure 12 right: x=-1m and z is the depth. These distributions show that electric field values in the space decays as 1/distance^3 and the occurrences of maximums strongly depend on the conductivity and distance between Tx and observation points. Even at later times the induced eddy currents are not negligible and they can produce secondary magnetic field, which could affect measure targets signals at later time.

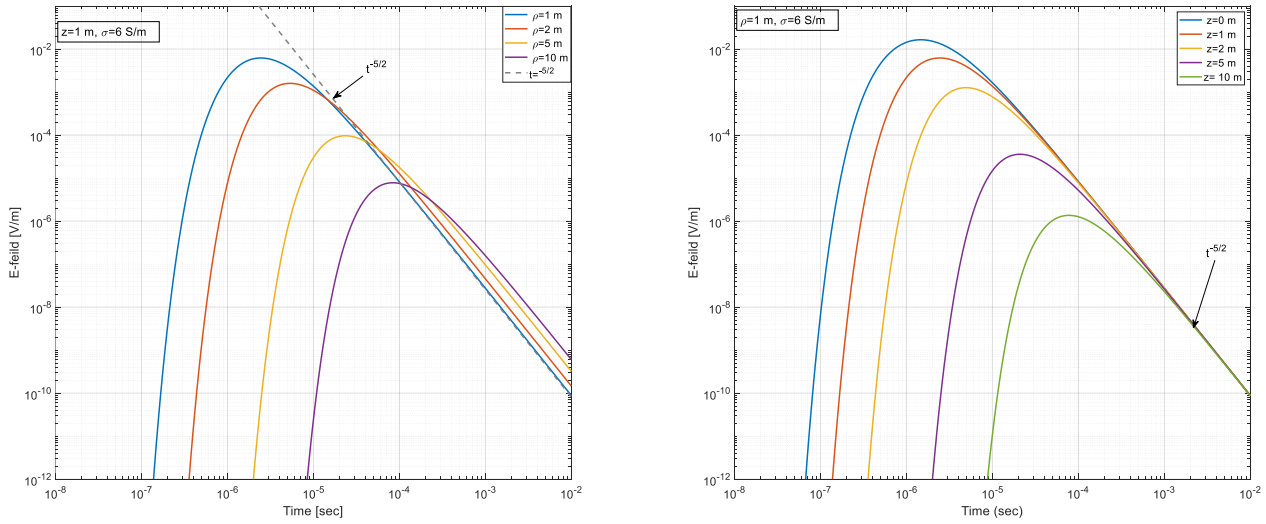

Figure 11. electric field vs time for horizontal Tx coil placed in medium with conductivity of 6 S/m , see Figure 10. Left: electric field at four different locations along lateral offset, for fixed z=1 m; Dashed line corresponds to $t^{-5/2}$ decay for comparison; Right: electric field at five locations along depth for fix ρ=x=-1m;

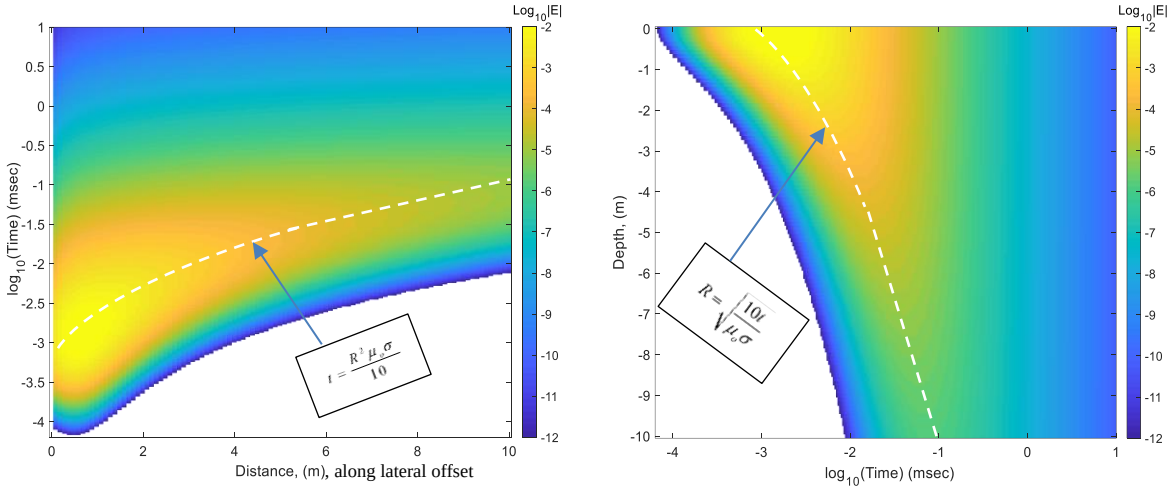

Figure 12. electric field distribution along lateral and vertical offsets for the horizontal 2m x 1 m Tx loop in 6 S/m conductive space.

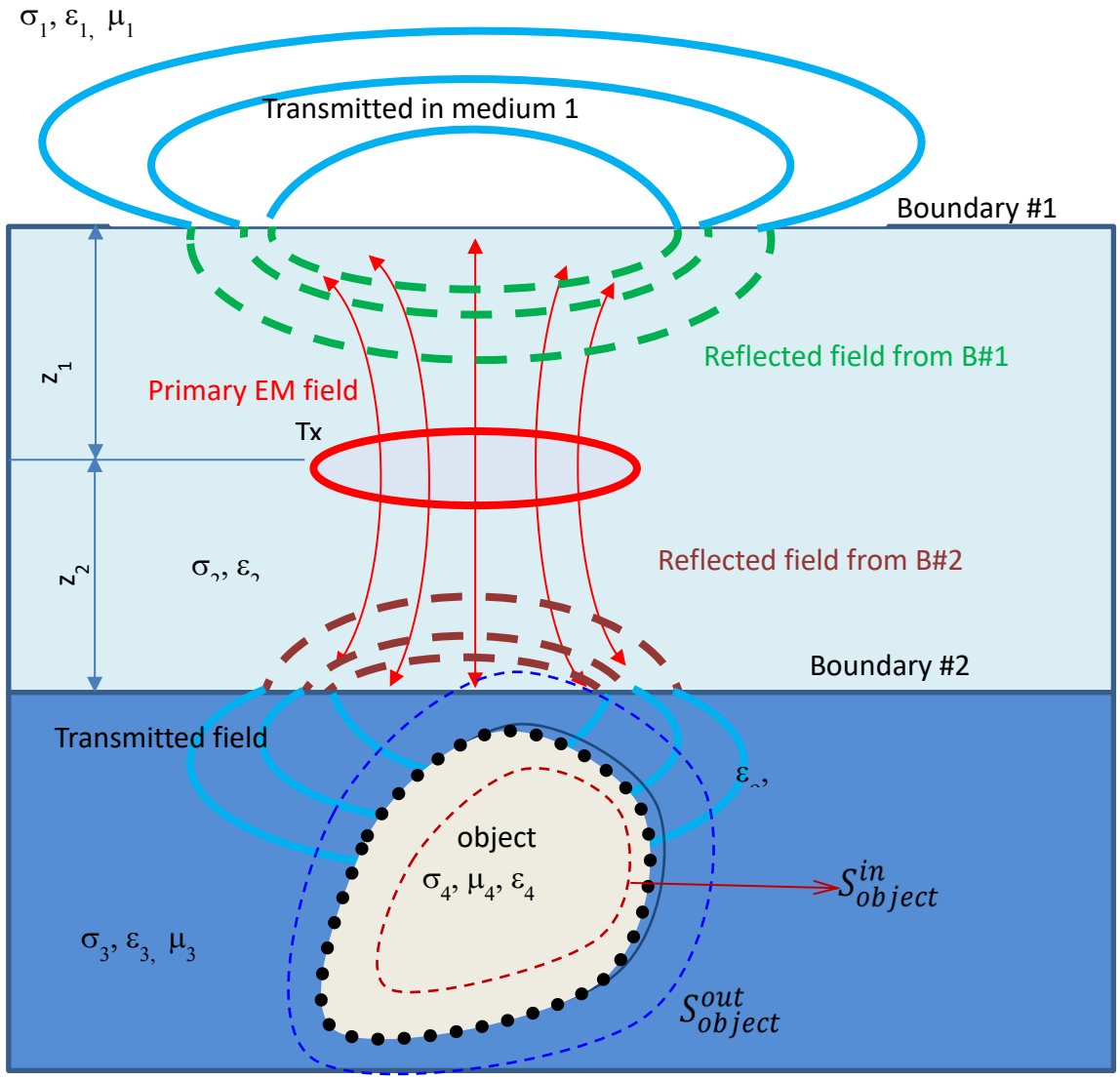

Figure 13. MAS diagram for an object embedded in a multilayer environment.

3.6 MAS for a target embedded a multilayer environment

Complete and detailed formulations of MAS for single and multiple targets are provided in references [10]-[14]. Here MAS is extended for a high conducting and permeable metallic target placed in a multilayer conducting environment. During electromagnetic induction sensing, a time varying magnetic field illuminates a target. The primary magnetic field penetrates inside any conducting and/or permeable object (or medium) and induces eddy currents within it. The induced eddy currents produce a secondary field that is measured external to the object at the receiver coil.

To begin, consider a conducting and permeable object and a multi-layer environment containing distinct, homogeneous, conducting and permeable media, $\ell = 1, 2, ..., N_{sec}$,where N_{sec} is the

number of each medium. Each medium is characterized by permittivity ε_ℓ [F/m], permeability μ_ℓ [H/m], and conductivity σ_ℓ [S/m]. The region external to the object is region 3, and the region internal to target is region 4. The unit normal vector $\hat{\mathbf{n}}_\ell$ points outward from the region $\ell+1$ to region ℓ, as represented in Figure 13.

The target is illuminated with a time-varying primary electromagnetic field generated by a Tx current embedded in medium 2. The time dependence expression of $\mathrm{e}^{\mathrm{j}\omega t}$ is assumed and its expression suppressed subsequently throughout. The primary magnetic field diffuses into medium 1, 2 and 3, and penetrates the object to some degree, inducing currents within and producing a secondary/scattered field outside. The primary magnetic field generated from the Tx coil inside its hosting medium-2 is represented with a set of cylindrical plane waves as:

$$\begin{aligned} \mathbf{B}^{pr} &= \sum_{n=1}^{N} \nabla \times \mathbf{A}_n^{pr}; \\ \mathbf{A}_n^{pr} &= \frac{\mu_o}{4\pi} \mathbf{J}_n \frac{e^{-ikR}}{R} = \frac{\mu_o}{4\pi} \mathbf{J}_n \int_0^\infty \frac{\alpha}{\beta} \mathrm{e}^{-\beta_2 |z-z_o|} \mathrm{J}_o(\alpha\rho) d\alpha; \end{aligned} \tag{18}$$

where $\mathrm{J_o}(.)$ is the Bessel's function of first kind and zero order, $\beta_m = \sqrt{\alpha^2 - k_m^2}$, m=2 number of medium, $\rho = \sqrt{(x-x_o)^2 + (y-y_o)^2}$, $\mathrm{k}_m = \sqrt{(\varepsilon_m \omega^2 - i\omega\sigma_m)\mu_m}$, and $(\mathrm{x_o}, \mathrm{y_o}, \mathrm{z_o})$ point is the Tx coil's center. The reflected and transmitted electromagnetic fields inside each medium are approximated as:

$$\mathbf{B}_m = \nabla \times \mathbf{A}_m, \tag{19}$$

$$\mathbf{E}_m = \frac{1}{i\omega\varepsilon_m\mu_m} \left(k_m^2 \mathbf{A}_m + \nabla \left(\nabla \cdot \mathbf{A}_m \right) \right) \tag{20}$$

Where $k_m = \sqrt{(\varepsilon_m \omega^2 - i\omega\sigma_m)\mu_m}$ and $\mathbf{A}_m = \int_0^\infty C_m^\nu \mathrm{e}^{s\beta_m(z-z_b)} \mathrm{J}_o(\alpha\rho) d\alpha$; $\mathrm{s} = \begin{cases} +1, & \text{when } z < z_b \\ -1, & \text{when } z > z_b \end{cases}$

$\mathrm{z_b}$ is distance from Tx center to a b=1,2… boundary. C_m^ν are unknown coefficients, which are calculated from the boundary conditions for tangential components of electric and magnetic fields at b=1,2… boundaries. ν is r (for reflected) or t (for transmitter) signals. The electromagnetic fields inside of each section of the metallic object are governed by the Helmholtz equation [15]-[16].

Under the MAS formulation, the fields at any **r** point inside object are represented as a superposition of fields created by a set of magnetic $\mathbf{P_o}$ (o=1,2,3, ..$\mathrm{N_{srs}}$) dipoles placed at $\mathbf{r}_\mathrm{o}$ points on the outer auxiliary surface, as

$$\mathbf{E}_m^t = \nabla \times \mathbf{F}_m^t \tag{21}$$

$$\mathbf{H}_m^t = \frac{1}{i\omega\mu_m}\left(k_m^2\mathbf{F}_m^t + \nabla\left(\nabla\cdot\mathbf{F}_m^t\right)\right) \tag{22}$$

Where $\mathbf{F}_m^t = \frac{1}{4\pi}\sum_{o=1}^{N_{srs}}\frac{e^{-ik_m R_o}}{R_o}\mathbf{P}_o$; $\mathbf{R}=\mathbf{r}-\mathbf{r}_o$; $t = inside$;

Similarly, the electric and magnetic fields at any **r** point outside the object in region m=3 are calculated as a superposition of fields generated by a set of magnetic $\mathbf{P}_{in}$ (in=1,2,3, ..) dipoles placed at $\mathbf{r}_{in}$ point on the inner auxiliary surface using the equations (21) and (22), when

$\mathbf{F}_m^t = \frac{1}{4\pi}\sum_{in=1}\mathbf{P}_{in}\left[\frac{e^{-ik_m R_{in}}}{R_{in}} + \int_0^\infty \frac{\alpha}{\beta_m}\mathrm{e}^{-\beta|z-z_{in}|}\mathrm{J}_o\left(\alpha\rho_{in}\right)d\alpha\right]$, where $\mathbf{R}=\mathbf{r}-\mathbf{r}_{in}$; m=3, $t = out$

Since the field of each of the auxiliary sources satisfies the Helmholtz wave equation, the only requirement imposed on these sources is to satisfy the boundary conditions - the continuity of tangential components of electric and magnetic fields on both sides of the physical surfaces:

$$[\hat{\mathbf{n}}\times\mathbf{E}_{b+1}^{total}] = [\hat{\mathbf{n}}\times\mathbf{E}_b^{total}], \quad b=1,2,3 \tag{23}$$

$$[\hat{\mathbf{n}}\times\mathbf{H}_{b+1}^{\text{total}}] = [\hat{\mathbf{n}}\times\mathbf{H}_b^{\text{total}}], \quad b=1,2,3 \tag{24}$$

here $\boldsymbol{n} = \boldsymbol{v}\times\boldsymbol{u}$ is the surface normal, $\boldsymbol{v}$ and **u** are orthogonal vectors tangential to the surface. The corresponding electric and magnetic field vectors are evaluated separately for the two domains bounded by the surface. Enforcing these boundary conditions results in a system of linear equations with respect to the unknown amplitudes of the auxiliary sources. Once the amplitudes of the auxiliary sources are found, any other EM parameter of interest (power flows through object boundaries, near and far fields, distribution of excited volumetric currents inside lossy dielectrics, etc.) can be derived through the superposition of fields created by real and auxiliary sources. This scheme also provides an easy way of monitoring the accuracy of the numerical solution by inspecting the mismatch of the boundary conditions: since the wave fields of each of the auxiliary sources satisfy the Helmholtz wave equation exactly, the only source of the simulation error is imperfect satisfaction of the boundary conditions, due to the discrete distribution of the auxiliary sources.

4.0 Time Domain EMI sensing Problem

During time-domain electromagnetic induction sensing, a transmitter current is turned on, it rises exponentially in time, reaches its maximum value, and stays on for a t_{on} period. The transmitter current produces the primary magnetic field that penetrates inside any highly conducting and/or permeable metallic object. At $t=t_{off}$ time the transmitter current is turned off. Immediately after that, eddy currents are induced inside conducting objects due to Lenz's law. The induced eddy currents produce a secondary field that is measured external to the object at the receiver coil. The electromagnetic data are then used in the sense that the mismatch between the measured and modeled data is minimized, and the target's intrinsic and extrinsic parameters are extracted. There are several forward EMI models for representing a target's EMI responses [17]-[20] in air. All these models use the simple magnetic dipole model approximation as the base model but utilize different variations. These models, which were developed for land based UXO detection and discrimination, assume that a target's EMI responses reach the Rx sensors instantaneously without any time delay. However, theoretical analyses [21], [22] and experimental data [6], [7] show that a magnetic dipole immersed in a conducting medium generates an electromagnetic field which builds up gradually and diffuse over a finite period of time . This excitation behaves somewhat like a "diffusion wave", and the propagation velocity v_o of its maximum point in the pulse form is inversely proportional to the conductivity of host medium [21], [22]. Since advanced EMI systems have different size transmitter and receiver coils, as well as different time on/off durations, there is a need to study the coils' characteristics and behavior in marine environments. This requires a solution of the full Maxwell's equations in the time domain for realistic field conditions.

There are different techniques for solving the Maxwell's equations directly using finite difference schemes. One of these techniques is the FDTD method [23]. It is well established that the FDTD solution of the Maxwell equations in the purely diffusive limit is time consuming, mainly resulting from the fact that the stability condition dictates a very small-time step. To overcome this problem, here the unconditionally stable Crank-Nicolson FDTD (CNFDTD) scheme [24] is adapted for solving time domain EMI problems.

4.1 Stability of the CNFDTD Scheme

Let us assume a transient current carrying transmitter loop is placed in an isotropic lossy dielectric and magnetic medium and generates electromagnetic fields. The electromagnetic fields are governed by Maxwell's equations. Using the CN-FDTD scheme, the Ampere's and Faraday's equations can be written as:

$$\frac{1}{2}\left(\nabla^H \times \mathbf{H}^{n+1} + \nabla^H \times \mathbf{H}^n\right) = \frac{1}{2}\sigma_e\left(\mathbf{E}^n + \mathbf{E}^{n+1}\right) + \varepsilon\ \frac{\mathbf{E}^{n+1} - \mathbf{E}^n}{\Delta t}, \tag{25}$$

$$-\frac{1}{2}\left(\nabla^E \times \mathbf{E}^{n+1} + \nabla^E \times \mathbf{E}^n\right) = \frac{\sigma_m}{2}\left(\mathbf{H}^{n+1} + \mathbf{H}^n\right) + \mu\ \frac{\mathbf{H}^{n+1} - \mathbf{H}^n}{\Delta t}. \tag{26}$$

Where field values at the n+1time step are unknown and those at the nth step are known from the initial conditions or from previous step of solution. And *x* component of $\nabla^E \times$ and $\nabla^H \times$ operators are approximated as

$$\left(\nabla^E \times \mathbf{E}\right)_x = \frac{E_z(i,j,k) - E_z(i,j-1,k)}{dy} - \frac{E_y(i,j,k) - E_y(i,j,k-1)}{dz},$$

$$\left(\nabla^H \times \mathbf{H}\right)_x = \frac{H_z(i,j+1,k) - H_z(i,j,k)}{dy} - \frac{H_y(i,j,k+1) - H_y(i,j,k)}{dz}.$$

Similarly, a reader can approximate y and z components of the $\nabla^E \times$ and $\nabla^H \times$ operators. *dy*, and *dz* are the spatial meshing sizes along the *y*, and *z* axes, *i*, *j*, and *k* are the integer number indices of the computational cells, and *n* is the time step index. From equations (25) and (26) electric $\mathbf{E}^{n+1}$ and magnetic $\mathbf{H}^{n+1}$ fields intensities at *n*+1 time can be estimated as:

$$\mathbf{H}^{n+1} = \frac{2\mu - \sigma_m \Delta t}{2\mu + \sigma_m \Delta t}\mathbf{H}^n - \frac{\mu\,\Delta t}{\sigma_m \Delta t + 2\mu} \cdot \left\{\nabla^E \times \mathbf{E}^{n+1} + \nabla^E \times \mathbf{E}^n\right\}, \tag{27}$$

$$\mathbf{E}^{n+1} = \frac{2\varepsilon - \sigma_e \Delta t}{2\varepsilon + \sigma_e \Delta t}\mathbf{E}^n + \frac{\varepsilon\,\Delta t}{\mu(2\varepsilon + \sigma_e \Delta t)} \cdot \left\{\nabla^H \times \mathbf{H}^{n+1} + \nabla^H \times \mathbf{H}^n\right\}. \tag{28}$$

After combining equations (27) and (28) the electric $\mathbf{E}^{n+1}$ field intensity at n+1 is,

$$\begin{aligned}\mathbf{E}^{n+1} = {} & \frac{2\varepsilon - \sigma_e \Delta t}{2\varepsilon + \sigma_e \Delta t}\mathbf{E}^n + \frac{\varepsilon \Delta t}{\mu(2\varepsilon + \sigma \Delta t)} \cdot \left\{1 + \frac{2\mu - \sigma_m \Delta t}{2\mu + \sigma_m \Delta t}\right\} \cdot \nabla^H \times \mathbf{H}^n - \\ & \frac{\Delta t^2}{\left(2\varepsilon + \sigma_e \Delta t\right)\left(2\mu + \sigma_m \Delta t\right)} \cdot \left\{\nabla^H \times \nabla^E \times \mathbf{E}^{n+1} + \nabla^H \times \nabla^E \times \mathbf{E}^n\right\},\end{aligned} \tag{29}$$

where Δt is *the time-step* size, ε and μ are the permittivity and permeability of the material, respectively, similarly σ_e and σ_m are electric and magnetic conductivities of the medium, respectively.

Let's use the CN-FDTD scheme and equations (27), (28) and (29) to derive a relation between the numerical wave vector components, wave frequency, time step, and space grid sizes. Assume that we have a plane, monochromatic wave as:

$\mathbf{E} = \mathbf{E}_o e^{J\left(\omega t_n - \mathbf{k}\cdot\mathbf{R}_{ijk}\right)}$ and $\mathbf{H} = \mathbf{H}_o e^{J\left(\omega t_n - \mathbf{k}\cdot\mathbf{R}_{ijk}\right)}$,

where

$\mathbf{k} = \mathrm{k}_x\hat{i} + \mathrm{k}_y\hat{j} + \mathrm{k}_z\hat{k},\ \mathbf{R}_{ijk} = \mathrm{x}_i\hat{i} + y_j\hat{j} + \mathrm{z}_k\hat{k};\ t_{n+1} = t_n^0 + \dfrac{\Delta t_n}{2};\ t_n = t_n^0 - \dfrac{\Delta t_n}{2};\ \mathrm{x}_i = i\Delta,\ \mathrm{y}_j = j\Delta$ and $\mathrm{z}_k = k\Delta$

After substituting the vector **E** and **H** fields into the CN-FDTD scheme equations(27) and (28), and combining the electric and magnetic fields equations, we obtain a homogenous system of equations for x, y and z components of the electric **E** field as:

$$\begin{pmatrix} A_1 & a_{xy} & a_{xz} \\ a_{yx} & A_2 & a_{yz} \\ a_{zx} & a_{zy} & A_3 \end{pmatrix} \begin{pmatrix} E_{0,x} \\ E_{0,y} \\ E_{0,z} \end{pmatrix} = 0 \tag{30}$$

Where

$$A_q = \frac{1}{\left(c\Delta t_n\right)^2}\tan^2\left(\frac{\omega\Delta t_n}{2}\right) - \left(\frac{1}{\Delta\psi^2}\sin^2\left(\frac{k_\psi\Delta\psi}{2}\right) + \frac{1}{\Delta\zeta^2}\sin^2\left(\frac{k_\zeta\Delta\zeta}{2}\right)\right),$$

$$\psi = \begin{cases} y, \text{ for q=1;} \\ z, \text{ for q=2;} \\ x, \text{ for q=3;} \end{cases} \text{ and } \zeta = \begin{cases} z, \text{ for q=1;} \\ x, \text{ for q=2;} \\ y, \text{ for q=3;} \end{cases},$$

,

$$a_{\eta\lambda} = a_{\lambda\eta} = \frac{1}{\Delta\lambda\Delta\eta}\sin\left(\frac{k_\eta\Delta\eta}{2}\right)\sin\left(\frac{k_\lambda\Delta\lambda}{2}\right),$$

$\eta = x, y,$ or z, and $\lambda = x, y,$ or z;

By setting the determinant equal to zero for the system of equations in (30), the general form of the numerical dispersion relation for the CN-FDTD scheme reduces to

$$\frac{1}{\left(c\Delta t_n\right)^2}\tan^2\left(\frac{\omega\Delta t_n}{2}\right) = \frac{1}{\Delta x^2}\sin^2\left(\frac{k_x\Delta x}{2}\right) + \frac{1}{\Delta y^2}\sin^2\left(\frac{k_y\Delta y}{2}\right) + \frac{1}{\Delta z^2}\sin^2\left(\frac{k_z\Delta z}{2}\right) \tag{31}$$

After considering a special case of a square uniform grid $\Delta x = \Delta y = \Delta z \equiv \Delta$, wavenumbers in each directions are $k_x = k_y = k_z = k/\sqrt{3}$, $k = \omega/c$. After introducing the grid sampling density $N_\lambda = \lambda_o/\Delta$ and defining the Courant stability factor for each non-uniform Δt_n time step as $S_n = c\Delta t_n/\Delta x$, from the equation (31) wavenumber can be expressed as

$$k = \frac{2\sqrt{3}}{\Delta}\sin^{-1}\left[\frac{1}{\left(\sqrt{3}S_n\right)}\tan\left(\frac{\pi S_n}{N_\lambda}\right)\right] \tag{32}$$

By choosing S_n and N_λ in the equation (32) the wavenumber k can have complex values. For the specific case of equation (32), the transition between real and complex values of k occurs when

$$\frac{1}{\left(\sqrt{3}S_n\right)}\tan\left(\frac{\pi S_n}{N_\lambda}\right) = 1 \tag{33}$$

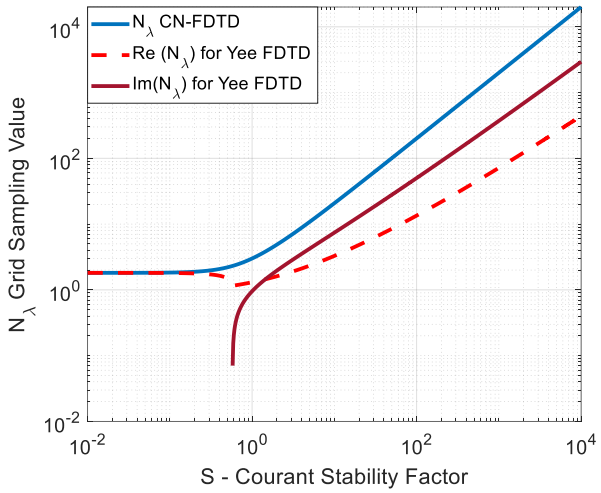

Figure 14. Grid sampling values versus S Courant stability factor for the CN-FDTD and standard Yee FDTD schemes.

At this transition N_λ grid sampling for the CN-FDTD scheme is

$$N_\lambda = \frac{\pi S_n}{\tan^{-1}\left(\sqrt{3}S_n\right)} \tag{34}$$

Since, $\tan^{-1}$ function is real for any real values, therefore N_λ is real for any S_n values as well. As a result, from equation (32) *k* wavenumber is a real number for any S_n values when equation (33) is hold. Figure **14** shows comparisons between grid sampling N_λ values for the CN-FDTD and standard Yee FDTD schemes [23]. The comparisons show that N_λ values are real for any S_n value for the CN-FDTD scheme and complex after $S_n > 1/\sqrt{3}$ for the standard FDTD scheme. For real *k* wavenumbers the numerical wave undergoes no attenuation while propagating in the grid, and when *k* is a complex then the numerical wave undergoes a nonphysical exponential decay while propagating on the grid. Thus, the equation (34) illustrates unconditional stability of the CN-FDTD scheme for any S_n values i.e. for non-uniform Δt_n time step. This opens possibilities to use not only non-uniform grid sizes but also non-uniform time steps in the CN-FDTD scheme.

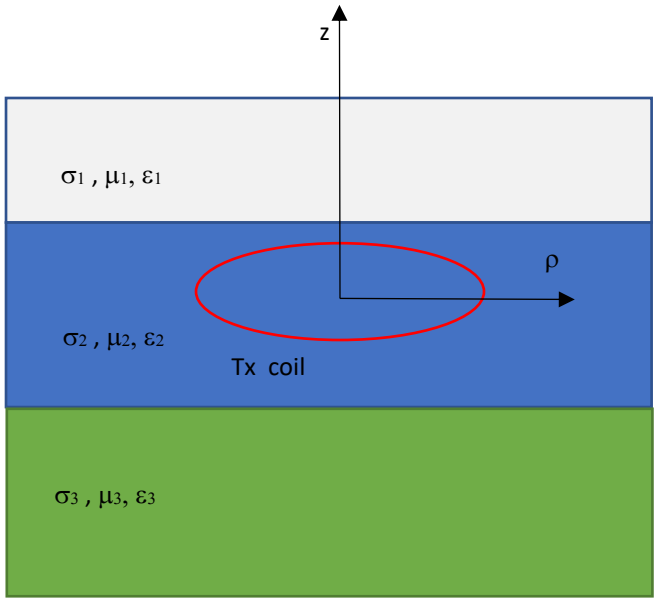

Figure 15. EMI diffusion problem's Geometry for a multilayer structure

4.2 CN-FDTD Scheme for multilayer structure in Cylindrical Coordinates

A circular Tx coil, carrying time varying current is placed in a medium. The coil produces symmetric electromagnetic fields, which penetrate in the layers and diffuses in them, see Figure **15**. After taking advantage of the problem's symmetry, the CN-FDTD scheme for electric and magnetic fields can be written as

$$E_{\varphi}^{n+1}(i,k)=\frac{2\varepsilon-\sigma\Delta t}{2\varepsilon+\sigma\Delta t}E_{\varphi}^{n}(i,k)+\frac{\Delta t}{2\varepsilon+\sigma\Delta t}\left[\begin{array}{l}\left\{\frac{H_r^{n+1}(i,k)-H_r^{n+1}(i,k-1)}{\Delta z}-\frac{H_z^{n+1}(i,k)-H_z^{n+1}(i-1,k)}{\Delta r}\right\}+\\ \left\{\frac{H_r^{n}(i,k)-H_r^{n}(i,k-1)}{\Delta z}-\frac{H_z^{n}(i,k)-H_z^{n}(i-1,k)}{\Delta r}\right\}\end{array}\right] \quad (35)$$

$$H_r^{n+1}(i,k)=H_r^{n}(i,k)+\frac{\Delta t}{2\mu}\left\{\frac{E_{\varphi}^{n+1}(i,k+1)-E_{\varphi}^{n+1}(i,k)}{k_z^h\Delta z}+\frac{E_{\varphi}^{n}(i,k+1)-E_{\varphi}^{n}(i,k)}{k_z^h\Delta z}\right\} \quad (36)$$

$$H_z^{n+1}(i,k)=H_z^{n}(i,k)-\frac{\Delta t}{2\mu}\left\{\frac{r(i+1)E_{\varphi}^{n+1}(i+1,k)-r(i)E_{\varphi}^{n+1}(i,k)}{\left(r(i)+k_r^h(i)\Delta r/2\right)k_r^h\Delta r}+\frac{r(i+1)E_{\varphi}^{n}(i+1,k)-r(i)E_{\varphi}^{n}(i,k)}{\left(r(i)+k_r^h(i)\Delta r/2\right)k_r^h\Delta r}\right\} \quad (37)$$

Where Δr and Δz are grid sizes in the radial and axial direction, respectively; *r(i)* is the radial distance in the cylindrical coordinate system and σ, μ, ε are conductivity, permittivity, permeability for (i,k) grid. After inserting $H_r^{n+1}(i,k)$ and $H_z^{n+1}(i,k)$ expressions into the equation for $E_{\varphi}^{n+1}(i,k)$ we obtain a sparse linear system of equations. The $E_{\varphi}^{n+1}(i,k)$ field is calculated at each (*i*,*k*) grid by solving the sparse linear system of equations. Once the $E_{\varphi}^{n+1}(i,k)$ -field is calculated, $H_r^{n+1}(i,k)$ and $H_z^{n+1}(i,k)$ are determined explicitly using equations (36) and (37).

5.0 Numerical and experimental results

The current land based UXO classification approach consists of: 1) deployment of dynamic electromagnetic induction (EMI) mapping systems, followed by 2) cued static data collection over each anomaly found in the map data, then 3) data inversion and targets' feature parameters extraction using advanced EMI models, and finally, 4) classifying all anomalies as UXO and non-UXO items.

5.1 Tx coil in UW environment

To achieve robust UW targets classification performance, first we need to understand how underwater environment effect on EMI systems operation. Figure 16 shows comparisons between

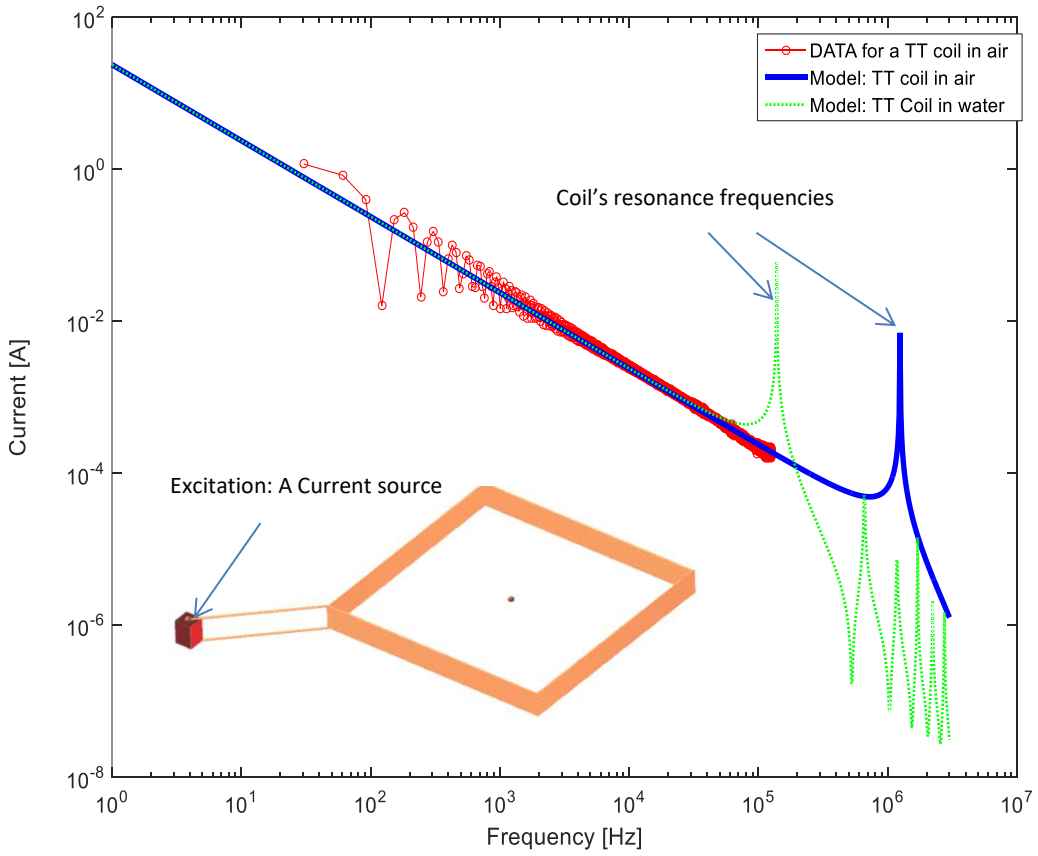

Figure 16. Induced current on the 68 cm x 68 cm square transmitter coil, with sixteen turns, placed in air and in UW environment.

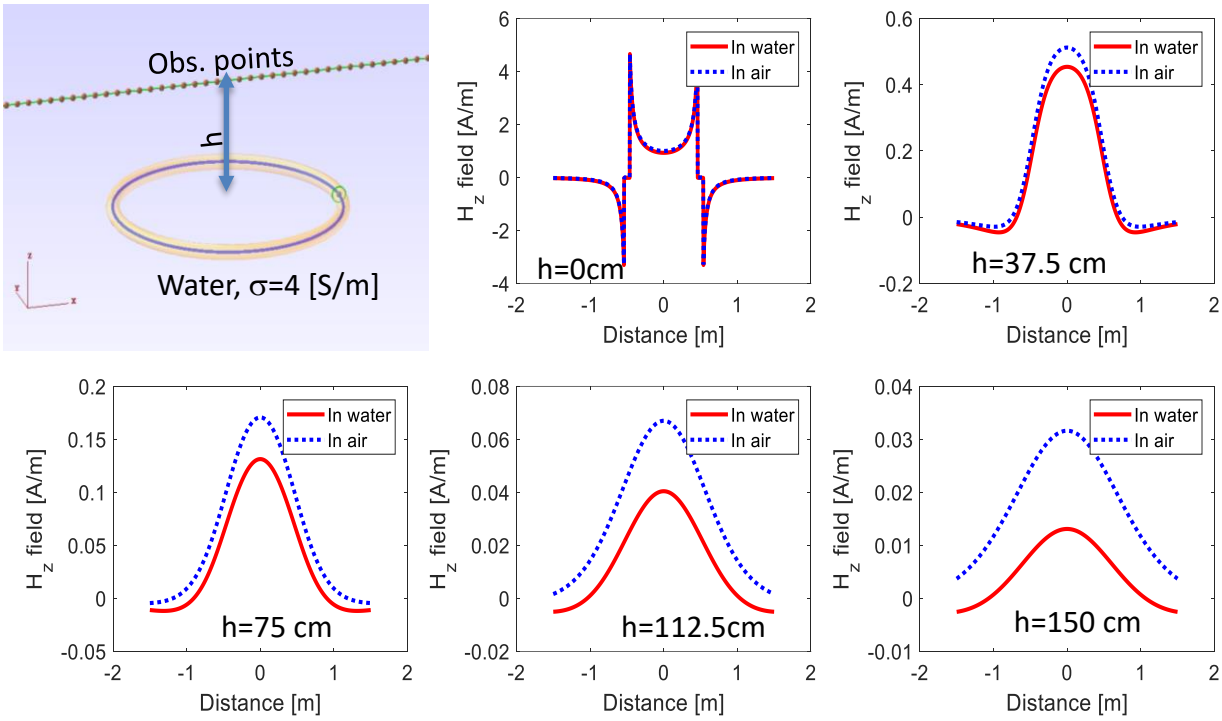

Figure 17: Upper left: A schematic diagram: an insulated coil is placed in a conducting space, and the primary magnetic field from the coil is calculated at observations points; Magnetic field vs distance at 50 kHz: comparisons between the primary magnetic fields along a line at different elevations for the coil placed in air and for the same size insulated coil in conducting water.

modeled and measured currents for the 16 turn, 68cm x 68 cm square coil. The calculations were done for Tx placed in air and in UW using the EMCOS's software package [26]. Underwater calculations were done for $\varepsilon_r = 81$ and $\sigma = 10^{-2}[S/m]$ freshwater. The computational result for coil in air agrees to actual measured data taken for the same size coil in air. The comparisons show that the coil's resonance frequency is shifted from 1 MHz (in air) to ~ 100 kHz when the coil is submerged UW. This shift in resonance frequencies introduces undesirable ringing currents at close to resonance frequency after Tx is turned off. At this close resonance frequency, the currents distribution on Tx coil is very sensitive to inductive and capacitive coupling, and they generate additional "noise" (uncontrollable signals) in the receiver coils, which has been observed experimentally in [7]. One of potential ways to avoid the resonance frequency shift is to insulate coil in the UW environment.

To further understand the primary magnetic fields sensitivity in conducting medium, Figure 17 shows the comparisons between the primary magnetic fields at different elevations for a coil in air and for the same size insulated coil in conducting space. The comparisons show that the conductive media affect the primary magnetic field, namely as the elevation h increases the spatial distribution of the primary magnetic field remain the same, where else due to absorptions the magnitude of the field in conducting water decreases in comparison to the field in air for the same Tx coil.

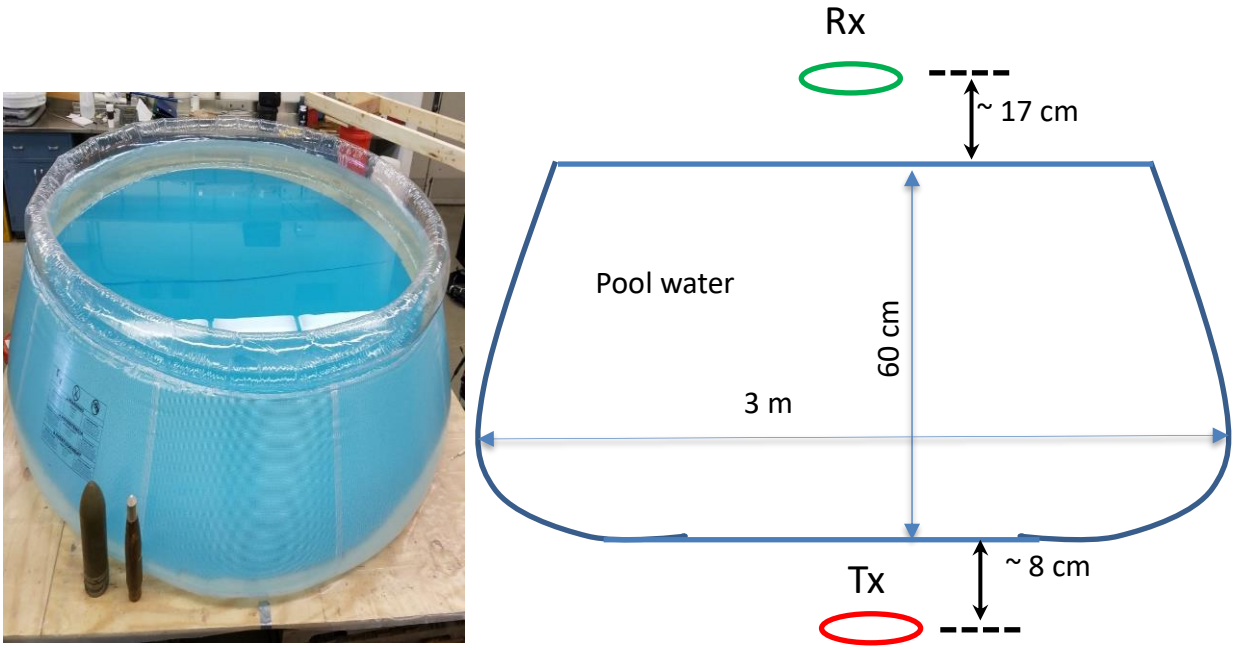

Figure 18 A schematic diagram of the experimental data collection. The data were collected low $\sigma = 1.26\ [S/m]$ and high $\sigma = 4.8\ [S/m]$ conducting salt water.

5.2 UW Lab Data collection and analysis

To validate the described frequency domain analysis, this section shows experimental results for a pool filled with different conductive water and a partially submerged 2.76-inch rocket. These data were taken at CRREL using a high frequency EMI induction sensor with detachable Tx and Rx configuration. The Tx and Rx coils are 27 cm in diameter, and each has 2 turns. The Figure 18 shows the pool and its dimensions. The Tx and Rx coils were placed under and above the 60 cm depth pool water, respectively. Figure 19 shows comparisons between modeled and actual data for the EMI signals at the pool center for salt water. Two cases were considered: low ($\sigma = 1.26\ [S/m]$) and high ($\sigma = 4.8\ [S/m]$) salts. The measured data were extracted as salt case minus no salt (tap water) case. The numerical results were obtained using the MAS technique. The results show good correlations between measured and modeled data. In addition, we see that the as salinity of the salt water increase from low (7.2 ppt) to high (31.5 ppt) the EMI response shift towards to low frequencies. Namely, in salt water we see a distinct shift in quadrature part that one must account for in both primary and secondary magnetic fields.

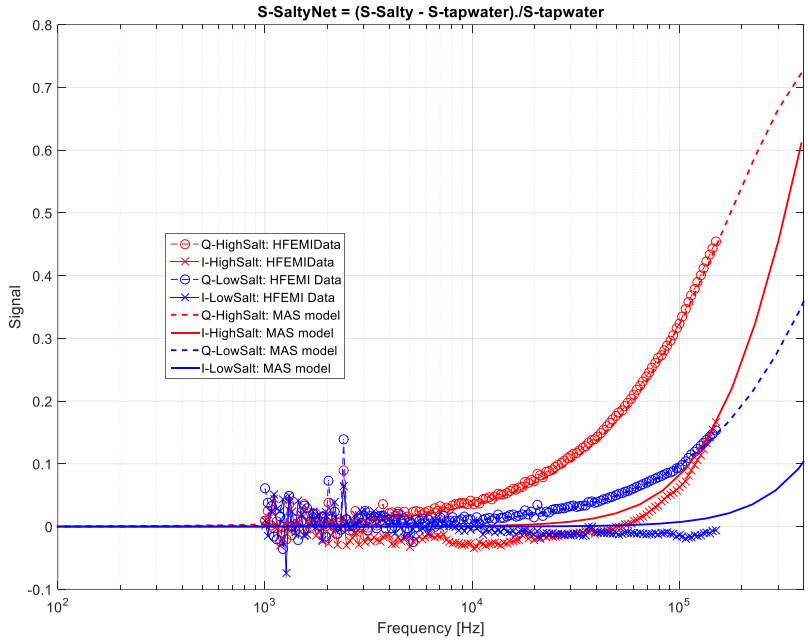

Figure 19. Measured and modeled EMI signals at pool center with no target other than the salt water.

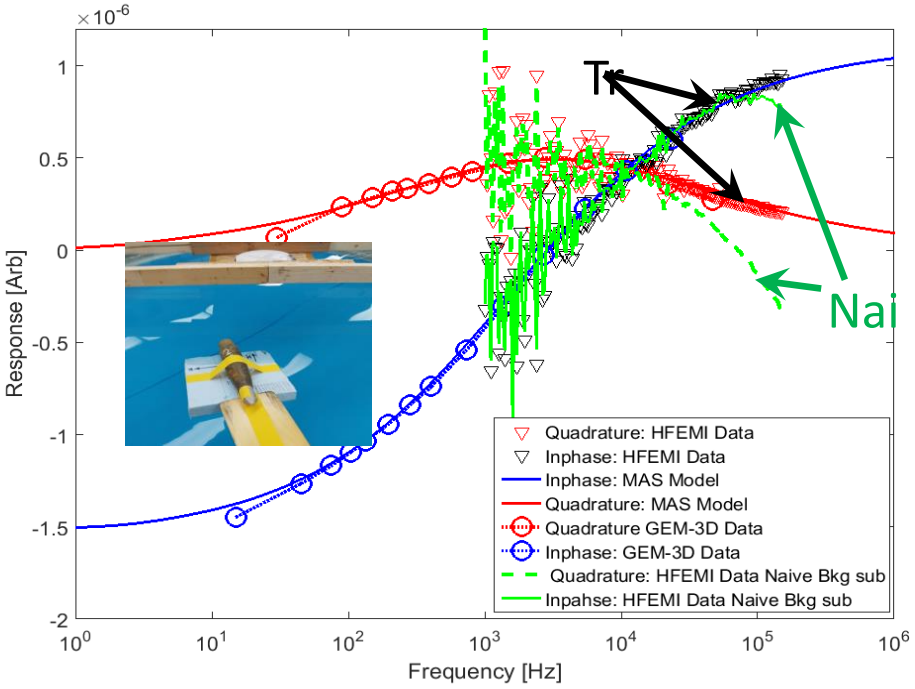

Figure 20. Comparisons between modeled and measured EMI responses for a 2.75" Rocket.

5.3 A new approach for extracting UW target's true EM responses

Finally, to illustrate how the salt water influences a targets EMI response, a 2.75" rocket as submerged in the salt water and EMI responses were measured using the high frequency EMI system, see inserted picture on Figure 20. The rocket's responses were calculated using two schemes: naïve and a new approach. Here the naïve calculation of the rocket's response F_{rocket} simply subtracts the salt water background signal S_{sw} from the data $S_{rocket+sw}$, as:

$$\textbf{Naive:}\ F_{rocket} = S_{rocket+sw} - S_{sw} \tag{38}$$

For extracting the true, intrinsic rocket response, in the proposed new approach, the result $S_{rocket+sw} - S_{sw}$ is scaled to the salt water background signal S_{sw} to account for the salt water alteration of the primary field. The final true rocket response is calculated, as

$$\textbf{True:}\ F_{rocket} = \left(S_{rocket+sw} - S_{sw}\right) \Big/ S_{sw} \tag{39}$$

Figure 20 shows comparisons between EMI responses for the 2.75" rocket obtained using the naïve and new approach. Since the high frequency EMI sensor has small signal to noise ratio at low (<100 kHz) frequencies, we also include the data measured using a low frequency EMI system called GEM-3D. In addition, the EMI response was modeled using the MAS technique for the same 2.75" rocket. These results show that the proposed new approach correctly extracts a targets true EMI response.

5.4 Dielectric Permittivity effect

In this section, the electric and magnetic fields are computed for a single turn, 50 cm radius transmitter loop carrying 1 A current placed in a uniform lossy dielectric medium. The fields are calculated at ρ =z=1 m from the center of the loop for conducting (left column: s= 10^{-2} [S/m], right column: σ = 4 [S/m]) and ε_r =1 non-dielectric (solid lines), and for ε_r =81 dielectric (dashed lines), uniform space. The results, depicted in Figure 21, show that for a high loss dielectric (σ = 4 [S/m]) the electromagnetic fields are identical in ε_r =81 dielectric and non-dielectric ε_r =1 medium. In addition, for a low-loss dielectric (σ = 10^{-2} [S/m]) the electromagnetic fields are identical below 1 MHz, (way above EMI sensing frequencies), in ε_r =81 dielectric and non-dielectric ε_r =1 medium, but they diverge at high frequencies. Thus, for

the frequencies of interest (40 Hz to 10 kHz) the displacement current $|j\omega\varepsilon_r\varepsilon_0\mathbf{E}|$ is still much smaller than the conduction current $|\sigma\mathbf{E}|$, and the quasi-magnetostatic approximation is applicable for underwater lossy-dielectric environments.

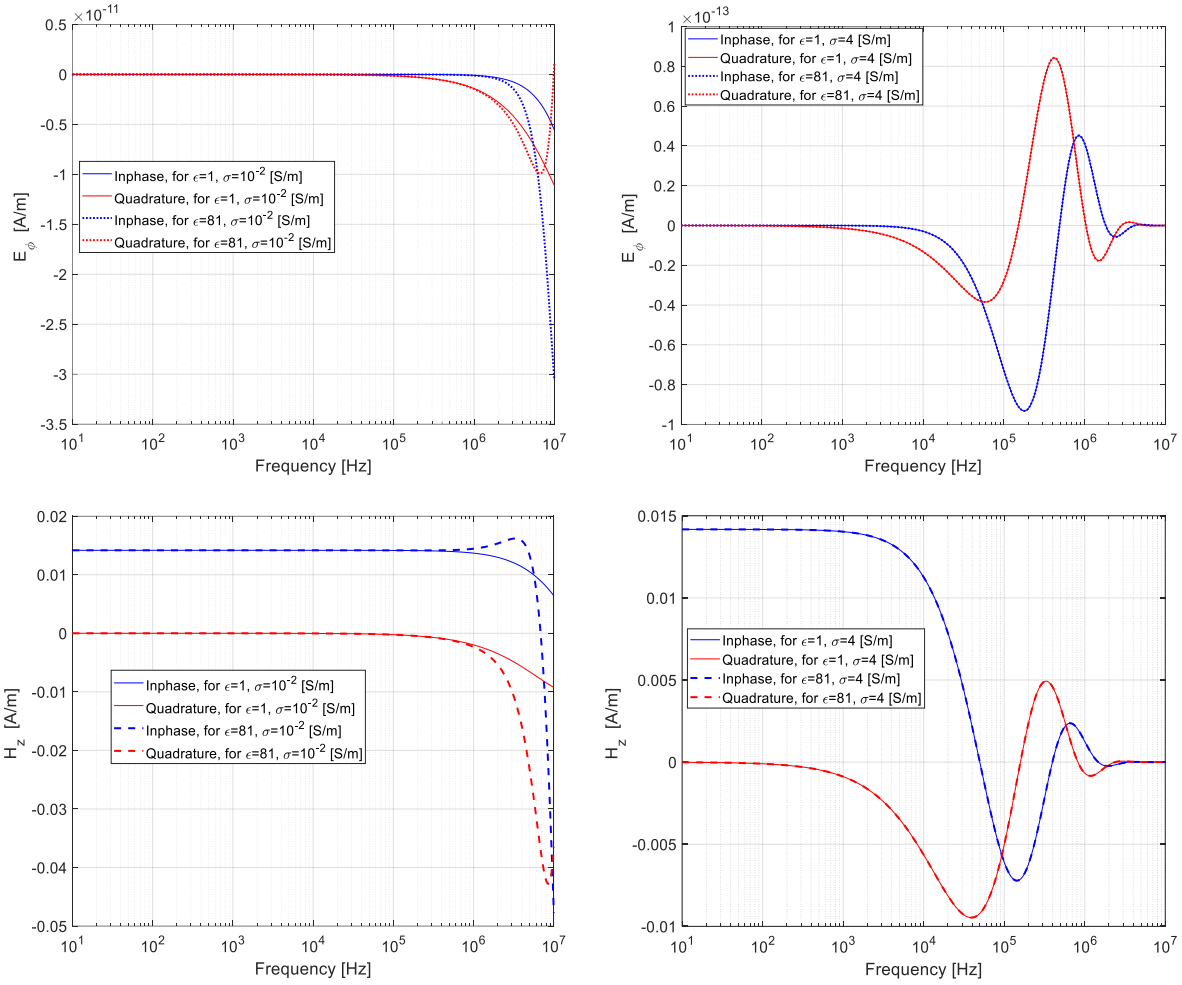

Figure 21. Electric E_ϕ (top row) and Magnetic Hz fields vs frequency for a single turn, 50 cm radius transmitter loop carrying 1 A current. The fields are calculated at ρ =z=1 m from the center of the loop placed in a uniform lossy (conducting) dielectric medium. Inphase (blue lines) and quadrature (red lines) parts of the electric E_ϕ and magnetic Hz fields for ε_r =1 (solid lines) and ε_r =81 (dashed lines) lossy dielectric media with (left) σ = 10^{-2} [S/m] and (right) σ = 4 [S/m] conductivity.

.

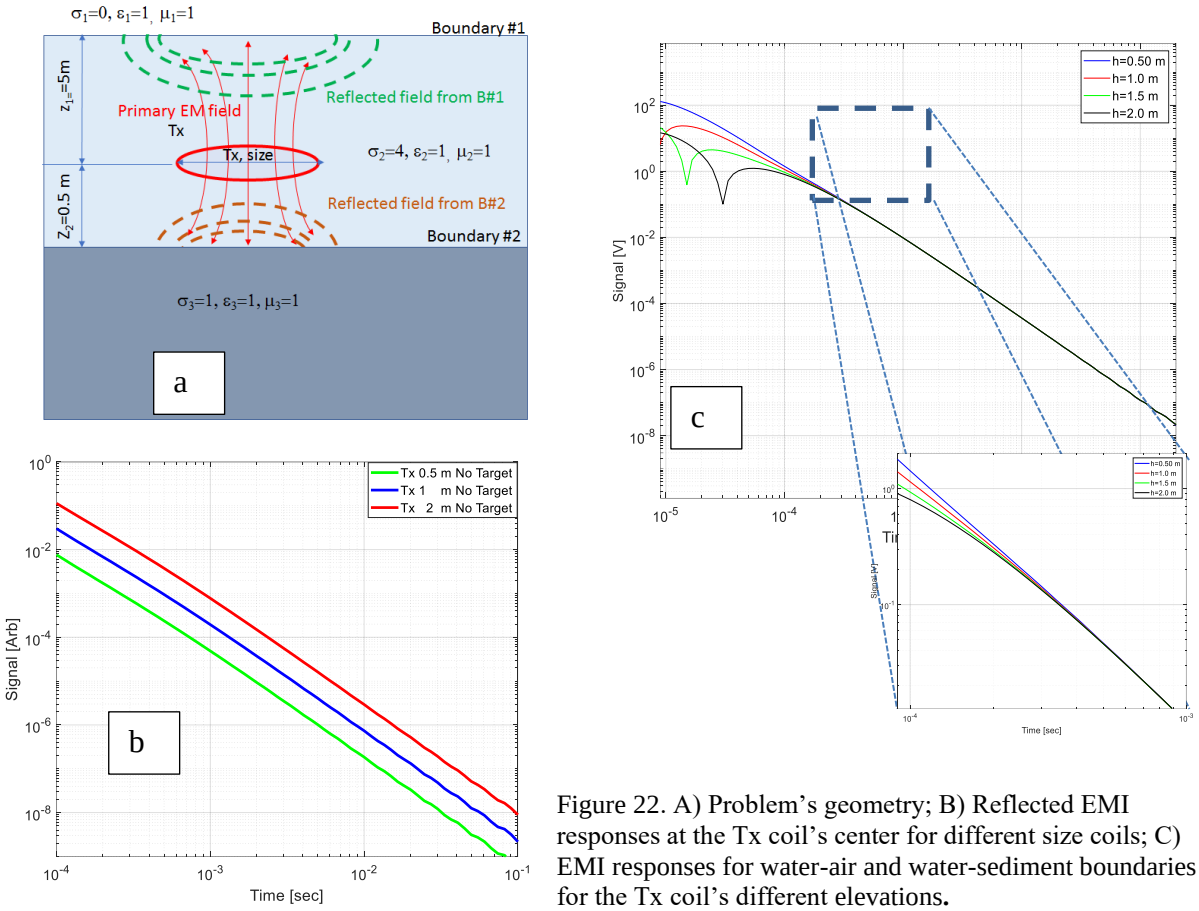

Figure 22. A) Problem's geometry; B) Reflected EMI responses at the Tx coil's center for different size coils; C) EMI responses for water-air and water-sediment boundaries for the Tx coil's different elevations.

5.5 Air-water-sediment boundaries

5.5.1 Sensor size and elevation effects

The dynamic and heterogeneous (UW plants, corals, rocks) sea-bed environment makes it difficult to deploy and place an EMI sensor close to buried UW metallic targets. Borrowing from land-based EMI, one of the potential ways to detect deep targets is to use a large Tx coil. Here the effects of Tx coil's size and elevations above the sea-bed boundary are investigated for a three-layer (air-water-sediment) structure. The problem's geometry and electromagnetic parameters for each layer are depicted on Figure 22a. The calculated total reflected EMI fields from the water-air and water-sediment boundaries at the center of Tx coil are shown in Figure 22b for different size coils. In these calculations, different size horizontal Tx loops are placed at $z_2=h_2$ = 50 cm above water-sediment boundary. The results show the total secondary field from water-air and water-sediment boundaries increases as the loop's size increases. Figure 22c shows the total reflected EMI field vs time for a 2 m size Tx loop placed at different elevations from the water-sediment boundary. In these calculations $z_2=h$ and $z_1=5.50-z_2$. The results (in inserted picture) demonstrate

that the reflected signals are sensitive with respect to elevation, and these effects extend up to 300 μsec.

5.5.2 Susceptible and/or conductive sediments effect on EMI signals

This section demonstrates EMI signals for susceptible and /or conductive sediments for the horizontal 2 m size coil placed at z_2=50 cm above water sediment boundaries. A frequency/time dependent susceptibility for the seabed is modeled using a log-uniform (Cole-Cole model) distribution, as

$$\chi = \chi_o \left(1 - \frac{1}{ln\left(\tau_2 / \tau_1\right)} ln \frac{1 - i\omega\tau_2}{1 - i\omega\tau_1} \right) \tag{40}$$

Where χ_0 is the zero-frequency limit, τ_1 and τ_2 represent lower and upper bounds for distribution.

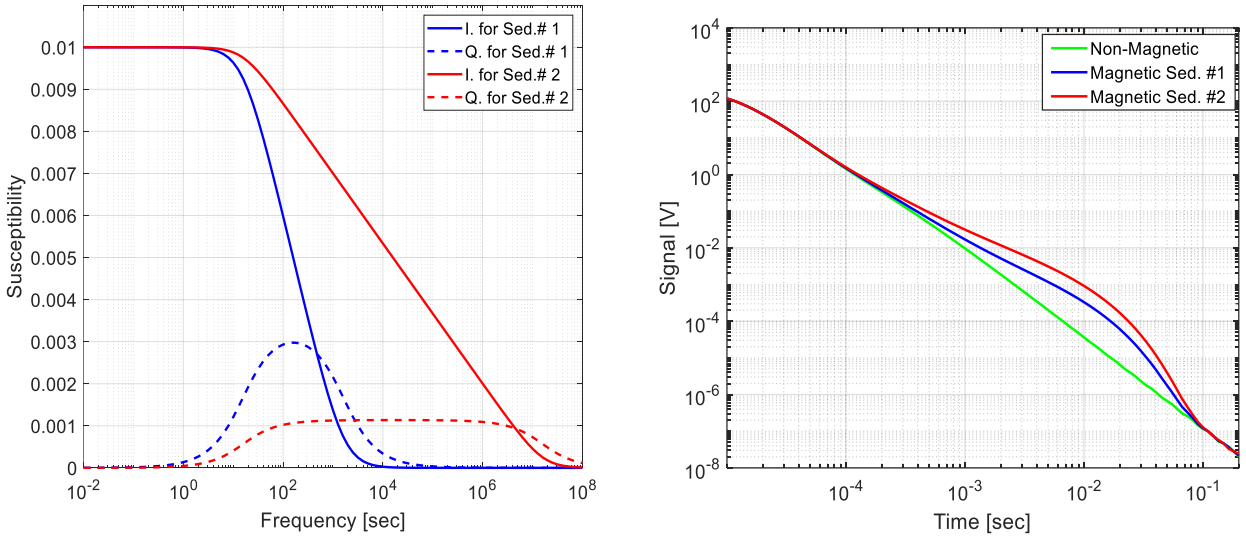

Figure 23.left: Susceptibility versus frequency for sediments. Blue lines are for χ_0=0.01, $\tau_1 = 10^{-8}$ [sec] and $\tau_2=10^{-2}$ [sec];and Red lines are for χ_0=0.01, $\tau_1 = 10^{-4}$ [sec] and $\tau_2=10^{-2}$ [sec]; Right: The total reflected EMI response from water (σ_2=4 [S/m], ε_2=1, μ_2=1)-air (σ_1=0 [S/m], ε_1=1, μ_1=1) and water-sediment (σ_3=1 [S/m], ε_3=1, μ_3=1+ χ) boundaries at the center of the Tx loop.

The left part of Figure 23 shows the χ susceptibility versus frequency for two types of sediments. In these calculations the susceptibility parameters for sediment type #1 are: χ_0=0.01, $\tau_1 = 10^{-8}$ [sec] and $\tau_2=10^{-2}$ [sec], and for sediment type #2: χ_0=0.01, $\tau_1 = 10^{-4}$ [sec] and $\tau_2=10^{-2}$ [sec]. The total EMI responses vs time at the center of 2 m size Tx coil placed at z_2=50cm (z_1=5 m) above the

water-sediment boundary is depicted on Figure 23 right. The comparisons between susceptible and non-susceptible sediments show that the effect of magnetic sediments appears at late time channels and their values and time-window (spread size) depend on τ_1 and τ_2 lower and upper time bounds. Since many, if not all, advanced EMI systems measure UXO targets EMI responses between 100 μsec and ~10 msec time window, the magnetic sediment could significantly influence UW targets EMI responses.

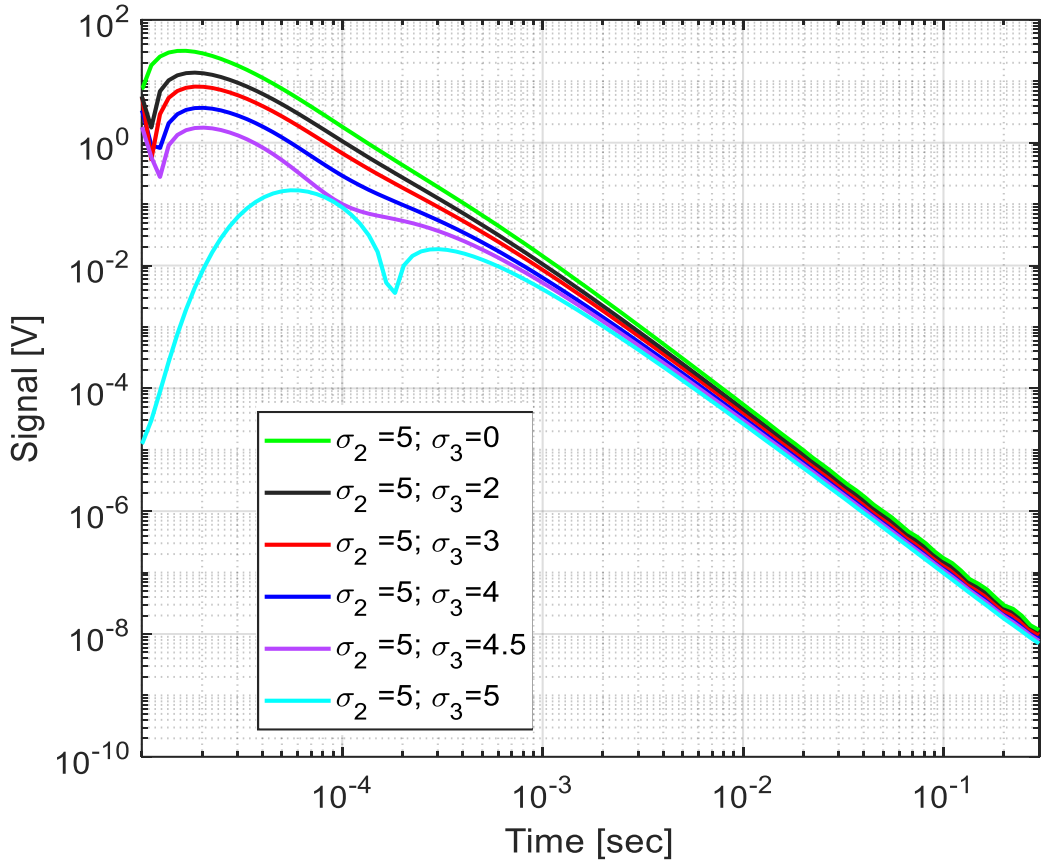

Figure 24. Total EMI signal versus time for three water-air and water-sediment boundaries for different conductive sediment.

Next EMI responses are investigated for three layer air (σ_1=0 [S/m], ε_1=1, μ_1=1), water (σ_2=5 [S/m], ε_2=1) and different conductive sediment (σ_3, ε_3=1, μ_3=1). The results are depicted on Figure 24. Calculations are done for the 2 m horizontal transmitter loop placed at z_2=50cm (z_1=5 m) above the water-sediment boundary. The results show that the total EMI signals from water-sediment boundaries vary with changing the sediment conductivities, and these effects are observable up to

1 msec. These reflected EMI signals produce additional noise and could potentially limit EMI targets detections in dynamic mode.

Finally, the comparisons between EMI signals for the three-layer air-water-sediment and the 10 cm diameter UW conductive σ_4=4 10^6 [S/m], permeable (μ_4=100) and non-permeable (μ_4=1), spheres are shown on Figure 25. Again, calculations are done for the 2 m horizontal transmitter loop placed at z_2=50cm (z_1=5 m) above the water-sediment boundary, and spheres are placed in the sediment at 70 cm and 100 cm from the center of the horizontal Tx loop. The secondary signals are calculated at the center of the Tx loop. The results show that total signal from water-air and water-sediment boundaries are higher than signals from the sphere at early time channels. The similar results are observed for 105 mm projectile, see Figure 26.

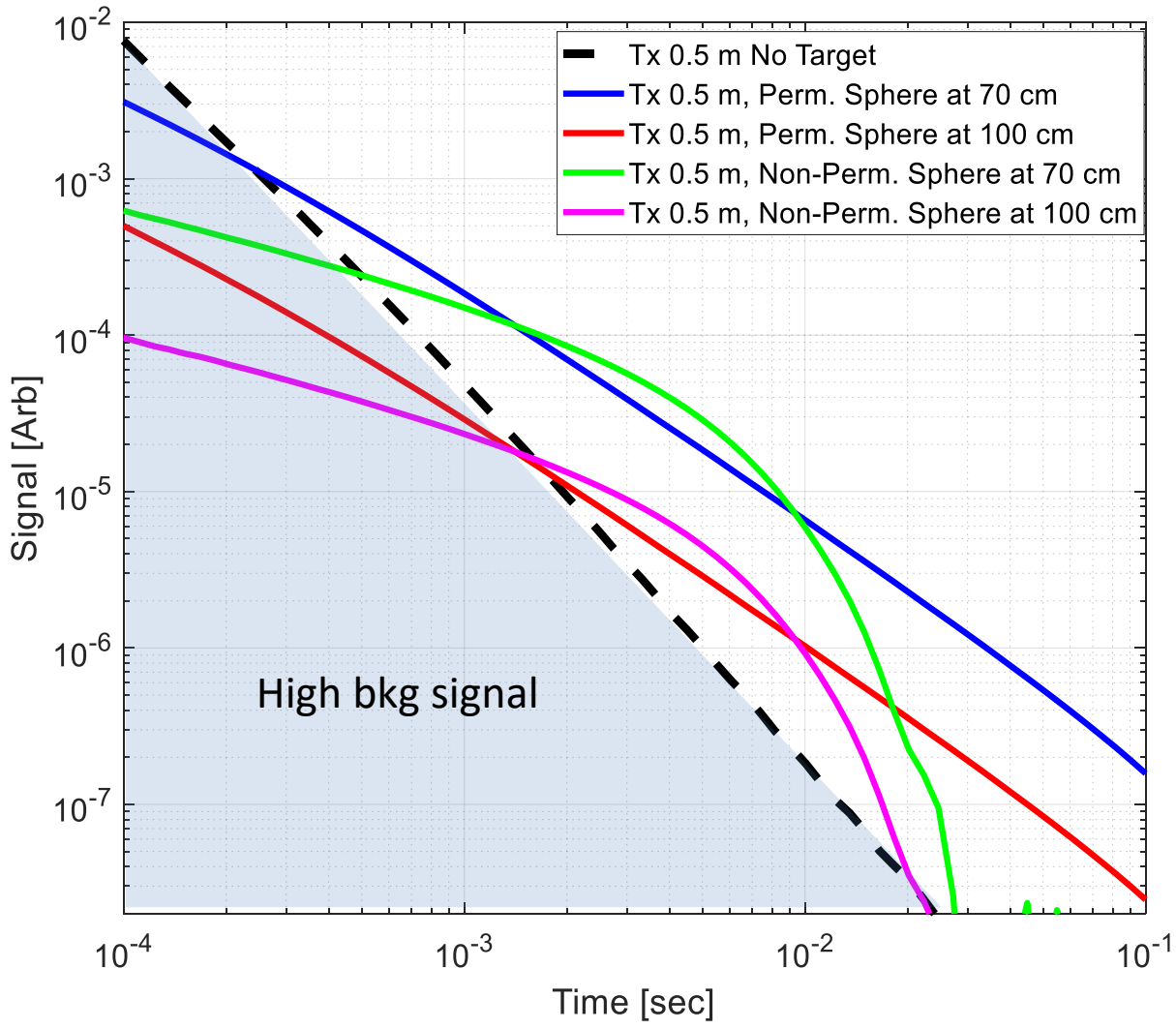

Figure 25. Comparisons between EMI signals for the three layer air-water-sediment and UW conductive, permeable and non-permeable spheres.

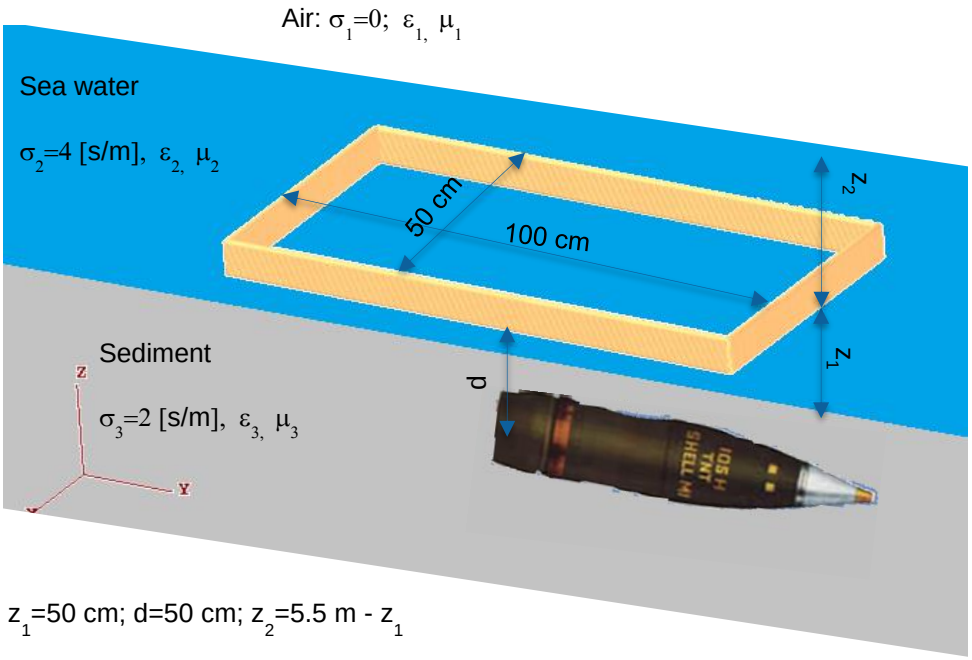

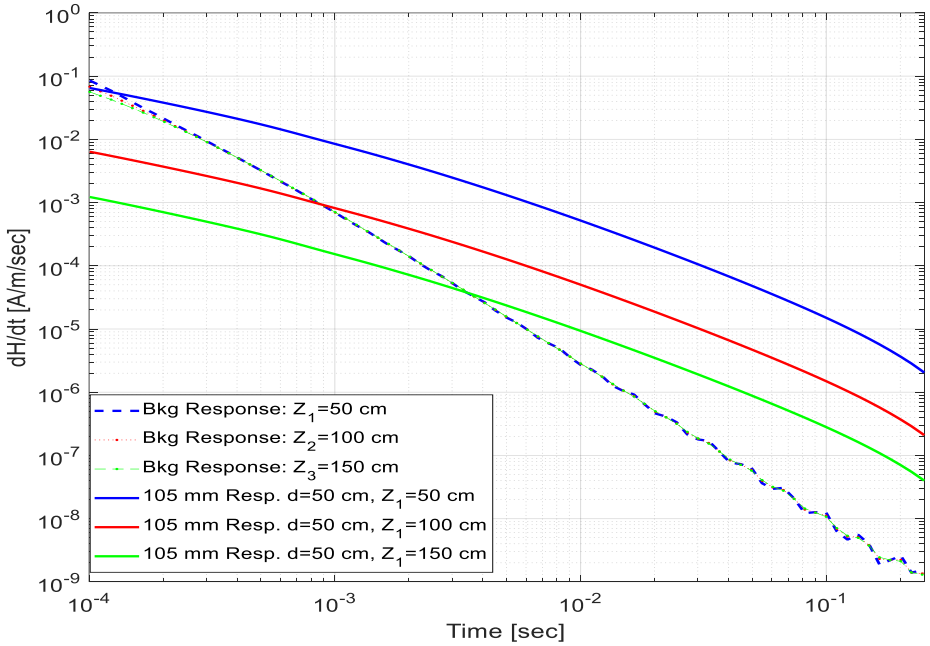

Figure 26. Comparisons between EMI signals for the three-layer air-water-sediment and UW conductive, permeable and 105 mm projectile.

5.6 Time domain analysis

Numerical calculations presented here are done for a 1 m diameter horizontal transmitter loop placed in the media #2, with σ_2=4 [S/m] conductivity, permeability μ_2=1, and permittivity ε_2=1. The loop caries the time varying current source, Figure 27.

$$J_\phi(t)=\begin{cases}1\text{-}e^{-t/\tau}, & \text{where } \tau=500\,[\mu\text{sec}], \text{ when } t\le 12.5\ [\text{msec}]\\ e^{-(t-12.5)/\tau}, & \text{where } \tau=100\,[\mu\text{sec}], \text{ when } t>12.5\ [\text{msec}]\end{cases} \tag{41}$$

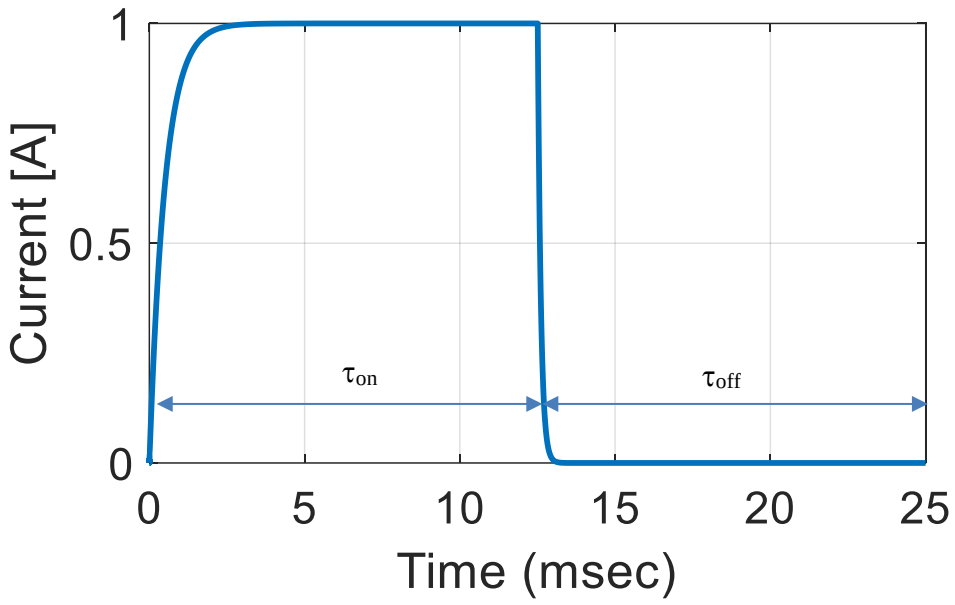

Figure 27. Current vs time in a Tx loop.

Figure 28 and Figure 29 show the electric E_ϕ and magnetic *Hz* fields distributions for uniform (left figures) and three-layer (right figures) structures, respectively after Tx current turn off. In these calculations the entire computational area is divided into *Nz*=201 x *Nr*=301 grid points, the spatial grid size is *dz*=*dr*=10 cm, cΔt=2500*dz* time step. The Tx coil is placed at 50 cm above the water-sediment boundary (with water-sediment parameters σ_3=2 [S/m], ε_3=1, μ_3=1). The comparisons between calculated fields for the Tx coil in the uniform and three-layer structure show some-slightly different distributions. To further illustrate how layer boundaries affect EMI signals in the time domain, Figure 30 and Figure 31 depict differenced electric $\left|E_\varphi^{layered}-E_\varphi^{water}\right|$ and magnetic $\left|H_z^{layered}-H_z^{water}\right|$ fields distributions for different time steps and for the Tx coil placed at 50 cm above water-sediment boundary (left figures) and for the Tx coil placed at 50 cm below water-air boundary (right figures), respective. The field distributions show, that more diffusive EM fields are "reflected" and spread in the area at water-air boundary than at water-sediment boundary, particularly at early times after turning off the Tx coil.

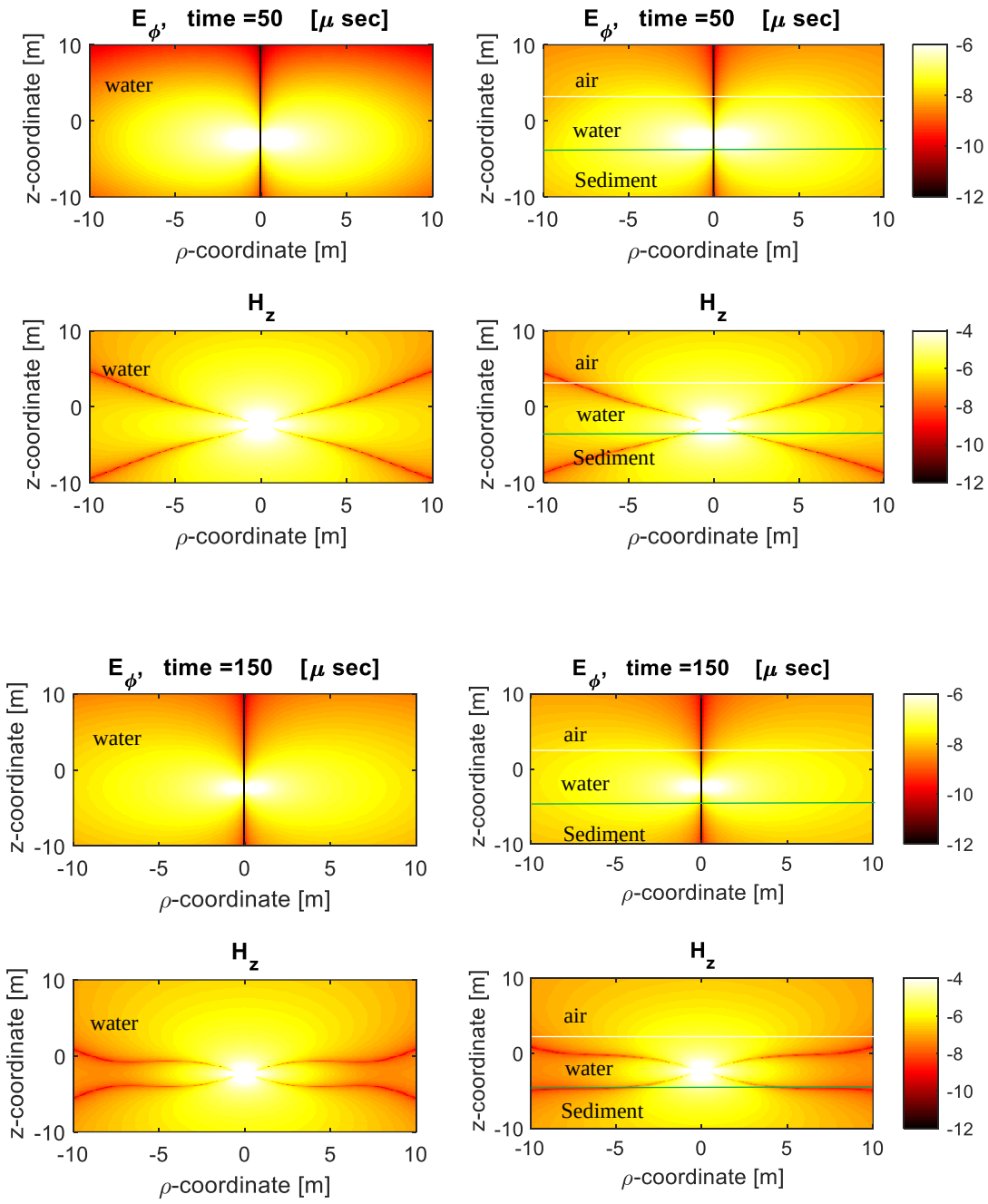

Figure 28. Snapshots at t= 50 μsec (top two rows) and t= 150 μsec (bottom two rows) after Tx current turn-off; electric and magnetic fields distributions in a uniform conducting space (Left) and in an air-water-sediment area for the 1 m diameter loop transmitter current placed at 50 cm above the water sediment boundary, green line. Fields are plotted as $\log_{10}|.|$.

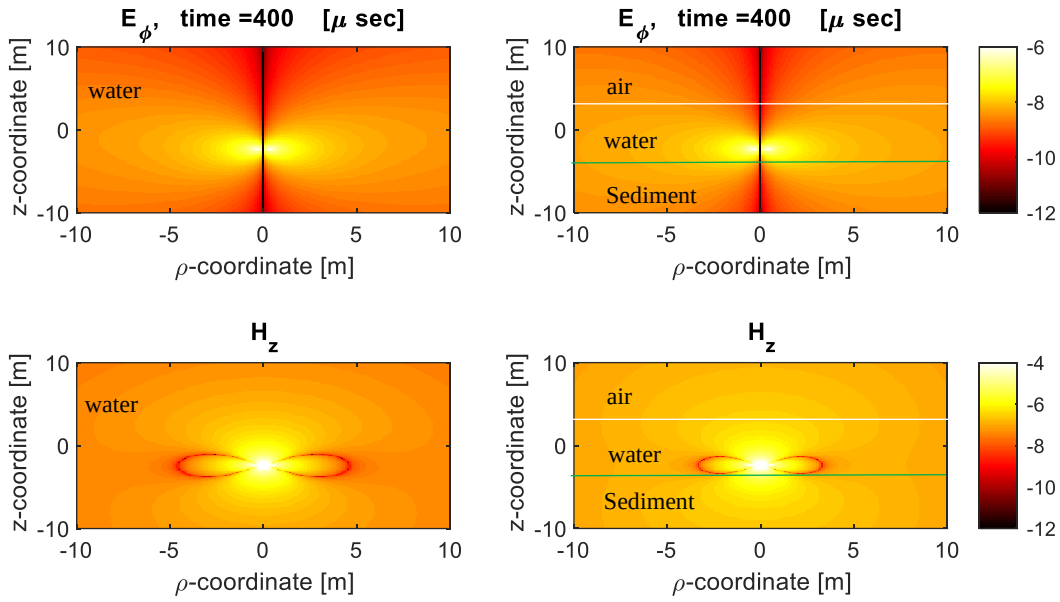

Figure 29. t= 400 μsec after Tx current turn-off; electric and magnetic fields distributions in a uniform conducting space (Left) and in an air-water-sediment area for the 1 m diameter loop transmitter current placed at 50 cm above the water sediment boundary, green line. Fields are plotted as $\log_{10}|.|$.

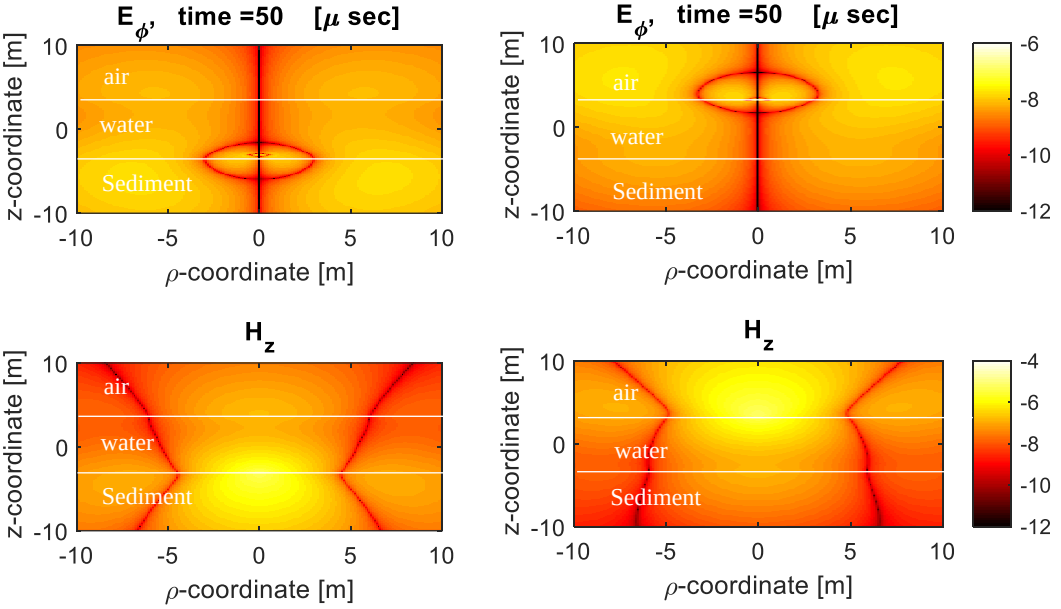

Figure 30. Snapshots at t= 50 μsec after Tx current turn-off; Differenced electric $\left|E_{\varphi}^{air-water-sediment}-E_{\varphi}^{water}\right|$ and magnetic $\left|H_{z}^{air-water-sediment}-H_{z}^{water}\right|$ fields distributions in an air-water-sediment area. The 1 m diameter tx current loop is placed at 50 cm Left: above water-sediment boundary and Right: below air-water boundary.

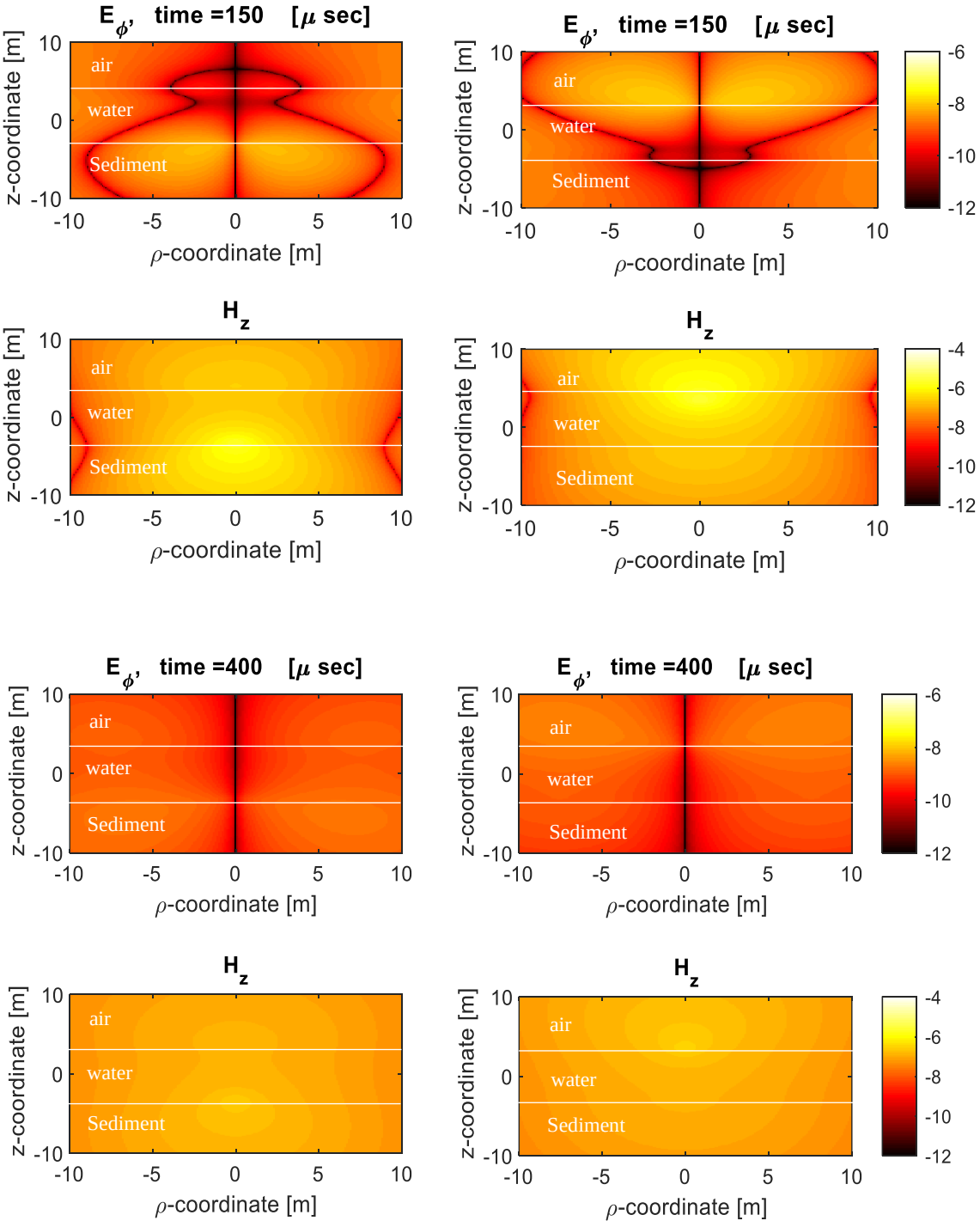

Figure 31. Snapshots at t= 150 μsec (top two rows) and t= 400 μsec (bottom two rows) after Tx current turn-off; Differenced electric $\left|E_{\varphi}^{air-water-sediment} - E_{\varphi}^{water}\right|$ and magnetic $\left|H_{z}^{air-water-sediment} - H_{z}^{water}\right|$ fields distributions in an air-water-sediment area. The 1 m diameter Tx current loop is placed at 50 cm: Left: above water-sediment boundary and Right: below air-water boundary.

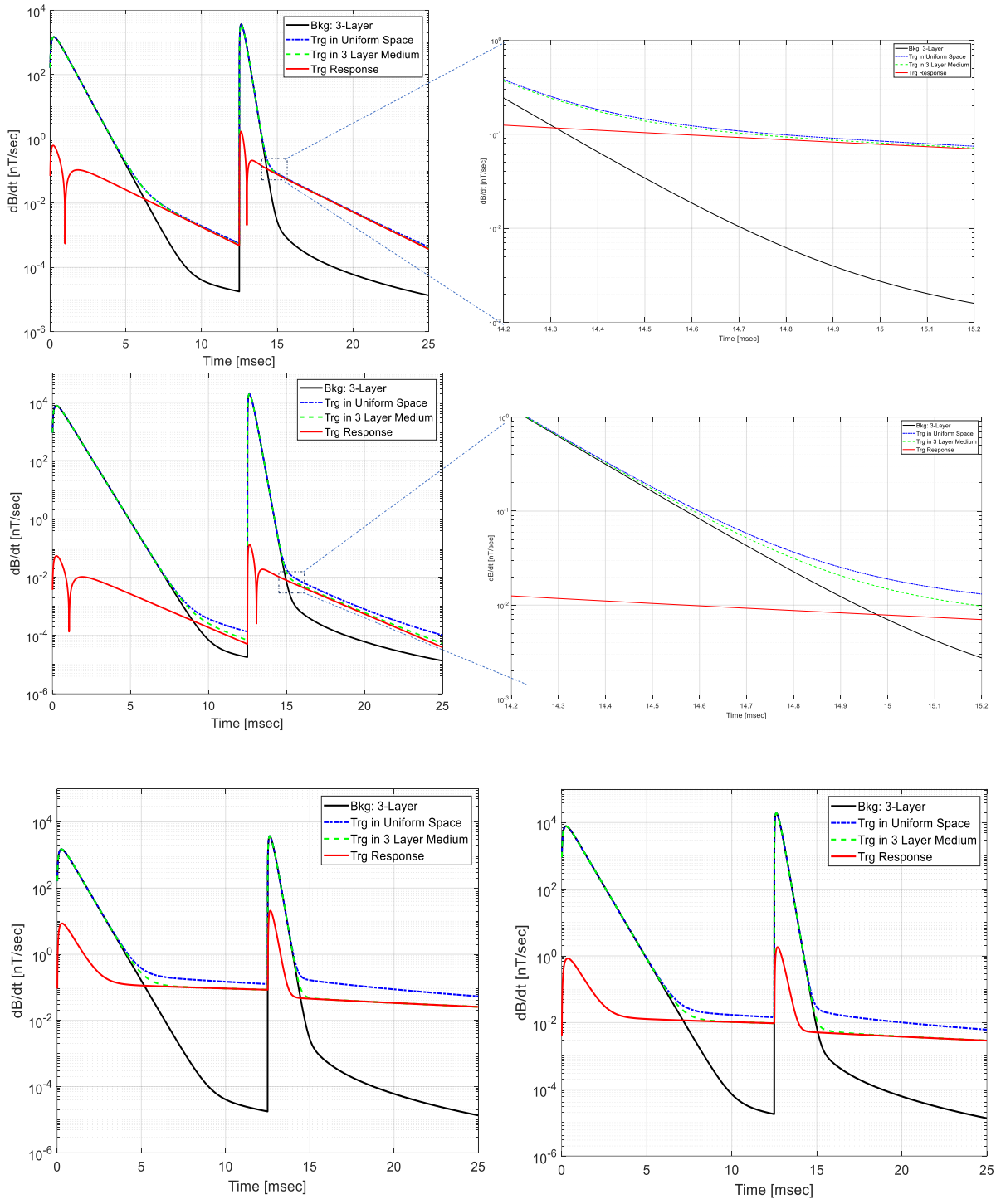

Figure 32. EMI responses for a conducting σ=4 10^6 [S/m] cylinder with length 70 cm 10 diameter; Top and middle rows: for μ=1 non-permeable and bottom row: for μ=100 permeable cylinder, respectively. Top and bottom lefts: for 80 cm , middle left and bottom right for 150 cm separations between the Tx and target's centers. Top and middle rights: zoomed selected sections on left.

Finally, the comparisons between $\partial \mathbf{B}/\partial t$ signals for the three-layer air-water-sediment (background) and the 70 cm length and 10 cm diameter conductive $\sigma=4\cdot10^6$ [S/m], non-permeable ($\mu=1$), and permeable ($\mu=100$) cylinder, placed in an uniform conductive ($\sigma_2=4$ [S/m], $\varepsilon_2=1$, $\mu_2=1$) and three-layer (($\sigma_1=0$ [S/m], $\varepsilon_1=1$, $\mu_1=1$, $\sigma_2=4$ [S/m], $\varepsilon_2=1$, $\mu_2=1$, $\sigma_3=2$ [S/m], $\varepsilon_3=1$, $\mu_3=1$) structure are shown on Figure 32. Again, calculations are done for the 1 m horizontal transmitter loop placed at $z_2=50$cm ($z_1=5$m below 5.5 m) above the water-sediment boundary. The cylinders are oriented vertically and placed in the sediment. Numerical data are obtained for 80 cm and 150 cm separations between the cylinder and Tx coil's centers. The induced *emf* ($\partial \mathbf{B}/\partial t$) are calculated for full (12.5 msec -on and 12.5 msec-off) waveform signals. The results show that, due to Tx current fast on and off there are very strong $\partial \mathbf{B}/\partial t$ responses. These responses, which are proportional to the time derivative of Tx currents, depend on the Tx currents and properties of the surrounded medium. Even after these strong initial responses, the signals from conducting medium (direct coupling from Tx to Rx coils, decays ~ $t^{-5/2}$) environment are higher than the target's responses at early times, but later time closely spaced targets responses become dominant. As a distance between the target and observation point increases the target's EMI responses decays and influence on the host media moves slightly to later time channels, see Figure 32 top and middle rights. In addition, the total responses in uniform conducting space are higher than for targets in a 3-layer environment, which are due to higher background response in uniform conducting medium due to stronger eddy, $\mathbf{J}=\sigma\mathbf{E}$; or $\mathbf{J}\sim \partial\mathbf{H}/\partial t$, currents. To better understand how conductivity distributions of conductivity influence the EM signals, using the CN-FDTD model, we also studied EM field distributions for three layer stepwise, conductivity (S/m)

$$\sigma=\begin{cases}0,\ \text{in air}, \text{depth}<0\\ 5\ , \text{depth}\ \in[0,10]\\ 1\ , \text{depth}\ \in[>10]\end{cases}$$

and for linearly changed continuing conductivity (S/m) Figure 33, modeled as

$$\sigma=\begin{cases}0,\ \text{in air}, \text{depth}<0\\ -0.2\ \cdot\text{depth}+5\ , \text{depth}\ \in[0,25]\\ 0, \text{depth}\ \in[>25]\end{cases}$$

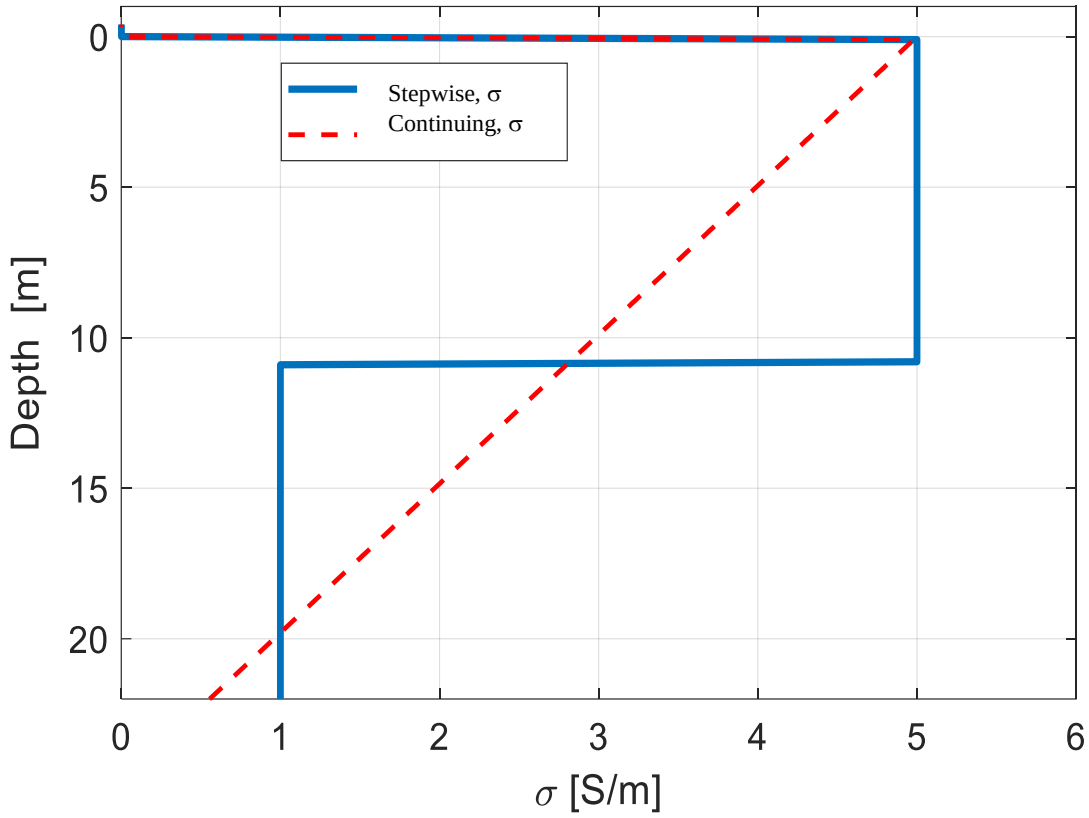

Figure 33. Distributions of stepwise and continuing conductivities.

Figure 34 shows comparisons between magnetic fields along z **(**ρ=0) and along ρ (z **=0**) axis at 200 μ sec and 400 μ sec after Tx currents were turned off

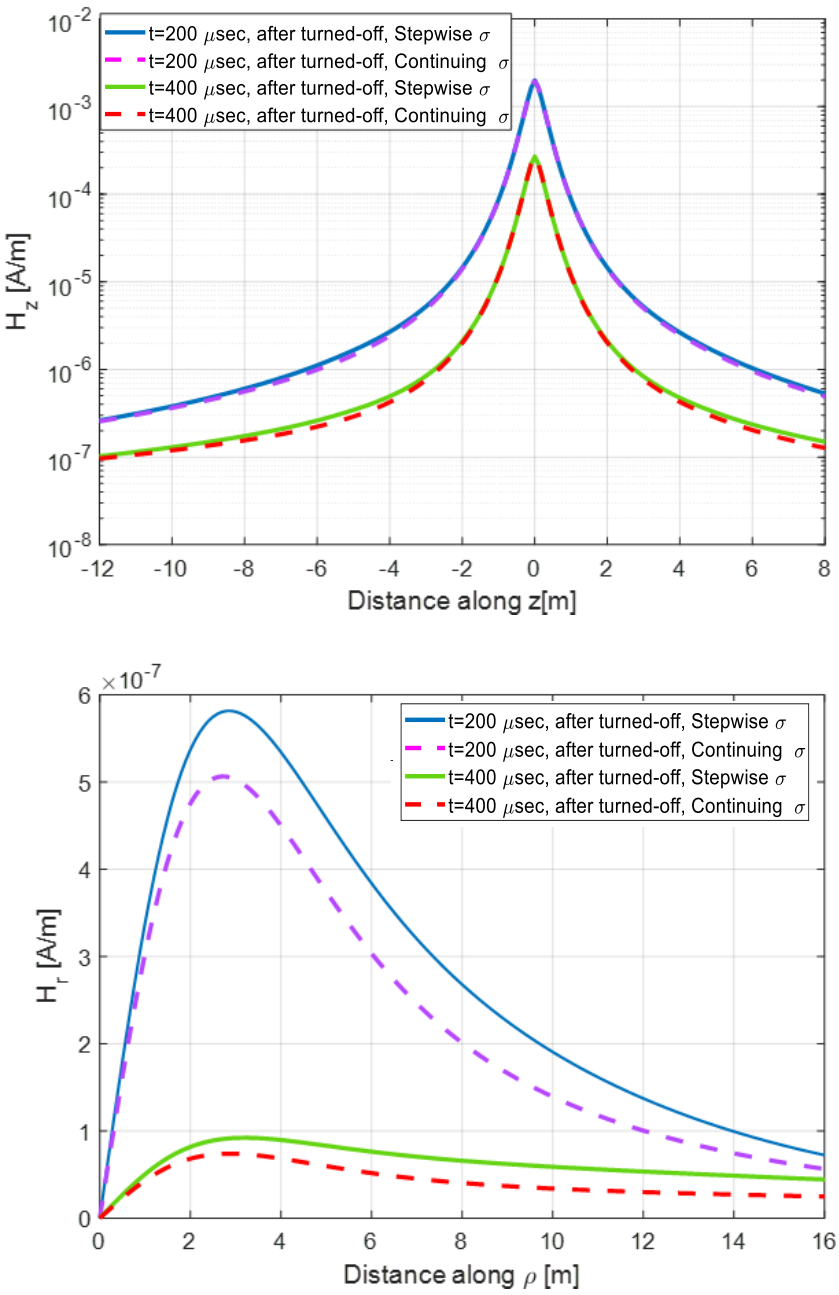

Figure 34. Comparisons between magnetic fields for stepwise and continuing conductivity models top: for H_z magnetic field along (ρ=0) z-axis and bottom: for H_ρ magnetic fields along ρ , (z=0) axis 200 μ sec and 400 μ sec after Tx currents were turned off.

The results show that H_z magnetic fields (Figure 34 top) along z-axis for stepwise and continuing conductivity models are identical, where else H_ρ magnetic fields along ρ axis have similar distributions but different magnitudes. These observed differences are correlated more to the eddy currents rather than to conductivity changes, see Figure 11.

5.7 Time domain Image method

In general UW UXO classification (and ultimately discrimination from clutter) is an inverse scattering problem. The inversion is carried out by 1) choosing a forward model that produces target responses and accurately accounts for underlying physics of EMI field diffusion in a complex UW environment; and 2) defining an objective function that measures the misfit between those predictions and measured data. The success of data inversion requires fast and robust forward models which account for complete EM signals from targets and surrounding environment. The results presented in sections 5.3 thru 5.6 demonstrate that the electromagnetic fields associated with the UW primary and secondary (targets response) fields can be complicated by the effect of reflections from the air-water, water-sediment, and sediment-water boundaries. These reflected or transmitted electromagnetic fields can introduce additional signals and contaminate target EMI responses. The electromagnetic diffusion fields are functions of frequency and the conductivity structure of the aqueous environment. The standard methods, such as FDTD, integral equations and etc., require substantial computational time and resources, and therefore they are unsuitable for data inversion and processing. A quick and easy way to calculate fields produced by multi-layered structures is a technique called the image method. The method has been extensively used for calculating the electromagnetic fields produced by time harmonic current sources near the earth's surface [38]-[41] in frequency domain. Here we extended the complex image method to transient problem and developed the time domain image method (TDIM). The TDIM is adapted to UW EMI data inversion scheme. The TDIM approximates fields due to induced currents in a multi layered structure, such as air-water and water-sediment, by representing the induced currents in each layer with an image current at a 'smoke ring' depth. Figure 35 shows normalized voltages produced by a step-off loop current placed in σ=4 [S/m] conducting half-space at h=6m below the air-water boundary. The calculations are done using analytical [42] and TD-image methods. The TDIM data agree with analytical results. The method is applicable for the half-space as well as for multi-layer-structure.

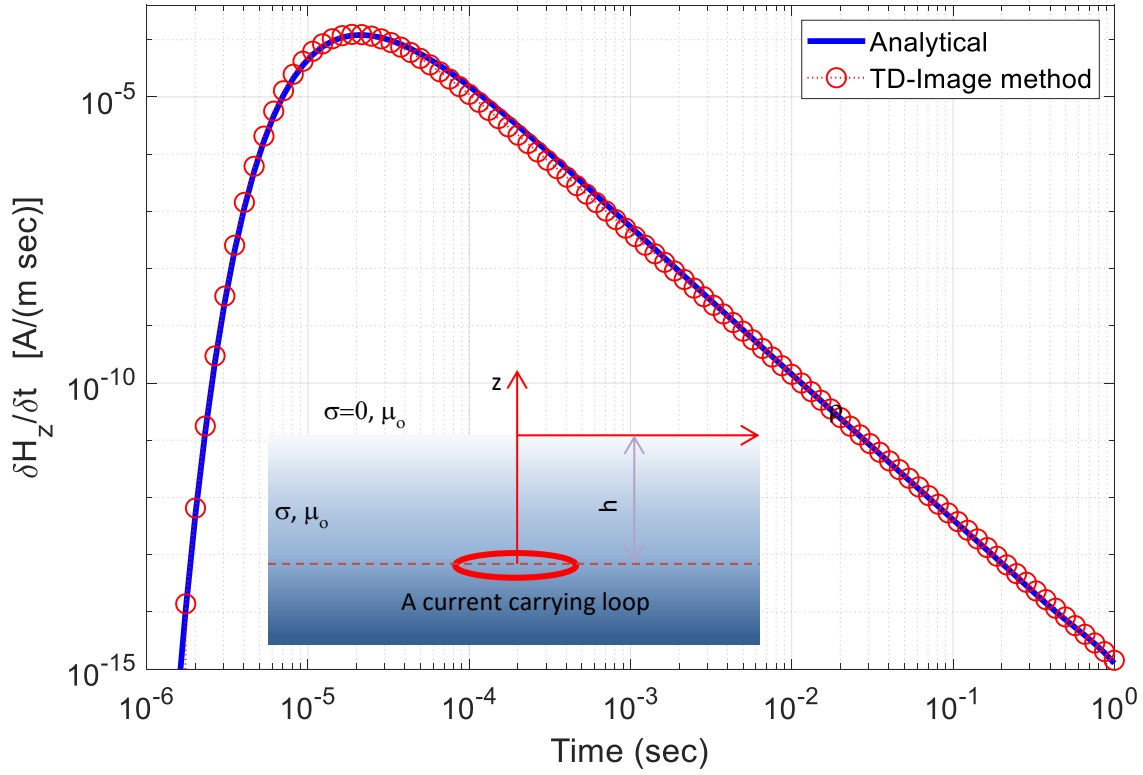

Figure 35. Comparisons between normalized voltage responses calculated using the analytical and TD-Image method at the axis surface of for a step-off function current in the buried source loop.

5.8 Investigating saltwater effects on transient electromagnetic induction sensing of submerged metallic objects using analytical methods

5.8.1 Signals in time domain

Given existing and emerging EMI sensing technology, we will divide time roughly into the following ranges:

time	Designation
< 0.1 ms	VET: Very early time
0.1 ms – 1 ms	ET: Early time
1 ms - 10 ms	MT: Mid-time
>10 ms	LT: Late time

As we shall see, under relevant sensing conditions, very strong SW effects appear in VET. However, in general, that realm is not examined in TD EMI sensing for UXO detection and discrimination. Substantial effects may appear in ET, possibly into the beginning of MT, and we will focus on those realms. For computing the TD S(*f*) from a submerged target, the physical system and its mathematical equivalent can be viewed in terms of a sequence of transfer functions, see Figure 36 and equation (42).

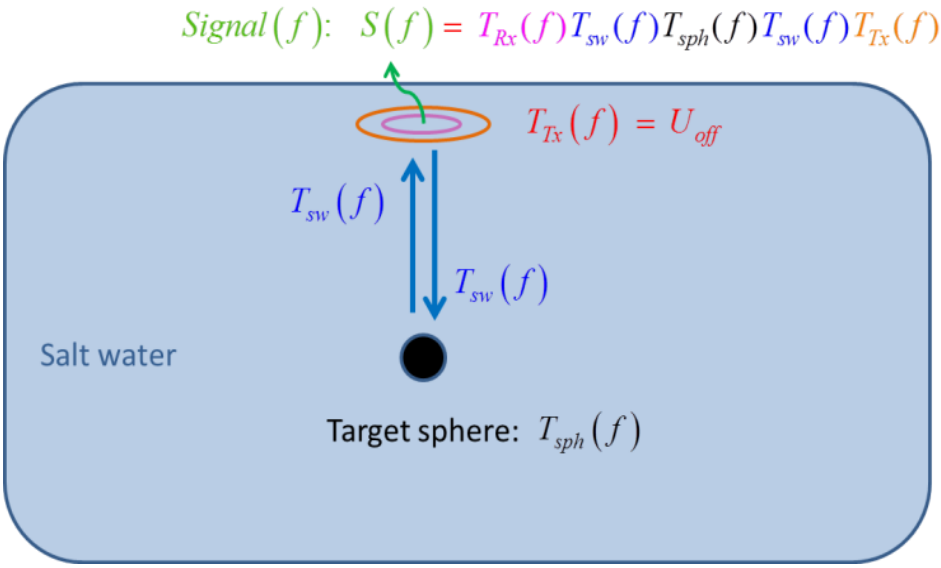

Figure 36. Within a background of SW, a sensor, with Tx and Rx co-located, sends a signal to and receives a signal from the responding target.

In the FD, the signal received from the target, $S(f)$, results from a concatenation of these effects, or transfers, tantamount to a product of the functions in sequence. The product sequence begins with the input of the transmitter (Tx), i.e. $T_{Tx}(f)$.

$$S(f) = T_{Rx}(f)T_{sw}(f)T_{t\arg}(f)T_{sw}(f)T_{Tx}(f) \tag{42}$$

Subsequent transfer functions act on this input, beginning with the SW's effect on the primary field, $T_{sw}(f)$; followed by the action of the responding target, $T_{targ}(f)$, e.g. that of a metal sphere, $T_{sph}(f)$ followed again by $T_{sw}(f)$, this time acting on the S(*f*) as it returns to the sensor; and finally the instrument receiver (Rx) performs its transformation of all this into a signal via $T_{Rx}(f)$. Integrating the inverse Fourier transform directly via

$$S(t) = \int df \; S(f)e^{2\pi ift} \tag{43}$$

produces the complete TD S(*f*) signal. Speaking of SW effect on the secondary field, we mean it to be implicit that this includes SW effects on the primary field, i.e. via the product $T_{sw}(f)\,T_{Tx}(f)$ in (42).

In principle one could perform an integration analogous to that in (42) - (43) but with all factors explicitly in the TD – a laborious sequence of convolutions. In some instances, however, we may proceed directly in time domain, in effect performing most of the work in (42) - (43) analytically, leaving only a tractable TD integral [27], [28] . This is the approach we shall use when calculating the response of a half-space of SW. In particular, for points on the boundary of the half-space due to a vertical magnetic dipole of moment M located at the origin (ρ, z=0) on the surface of that half-space

$$\frac{\partial B_z}{\partial t} = \frac{9M}{2\pi\sigma\rho^5}\left\{\Phi(u) - \sqrt{\frac{2}{\pi}}e^{-u^2/2}\left(u + \frac{u^3}{3} + \frac{u^5}{9}\right)\right\}$$

$$where\ \mathrm{u}^2 = \frac{\sigma\mu\rho^2}{2t};\quad \Phi(u) = \sqrt{\frac{2}{\pi}}\int_0^u e^{-\xi^2/2}\,d\xi \tag{44}$$

where σ, μ are properties of the responding SW half-space. Note that this expression calculates the signal (i.e. $\partial B_z/\partial t$) from the SW itself, as a background. This is distinct from computing the SW's alteration of the target's S(*f*), which, in practice, must be extracted from a signal containing background as well.

5.8.2 Specification of contributing factors

Let us begin our treatment with the middle factor, $T_{targ}(f)$. The target will frequently be considered below to be a representative sphere, with

$$T_{targ}(f) = T_{sph}(f) = \left(2\pi\alpha^3\right) conj\left\{\frac{\left(2\mu_r+1\right)\left(1-\kappa\alpha\ cot\left(\kappa\alpha\right)\right)-\left(\kappa\alpha\right)^2}{\left(\mu_r-1\right)\left(1-\kappa\alpha\ cot\left(\kappa\alpha\right)\right)+\left(\kappa\alpha\right)^2}\right\} \tag{45}$$

$$\kappa = k\ for\ sphere, \quad \alpha = radius\ of\ sphere$$

The parameter κ [m^{-1}] is $k^2 = -\omega^2\mu\varepsilon\left[1-i\frac{\sigma}{\omega\varepsilon}\right] => i\omega\mu\sigma$ (46)

where ω is the angular frequency (rad/s); μ [*H/m*] is the magnetic permeability of the target material and σ [*S/m*] its electrical conductivity. One form or anothr of this solution appears in many works preceding and including ref [29]. The form in (45) accommodates the positive time exponent convention in (43), which also determines the sign inside the square root in (46). The relative permeability of the object is $\mu_r = \mu/\mu_o$ and $\mu_o = 4\pi \times 10^7\ H/m$ is the magnetic permeability of free space. We assume here, as through the entire paper, that the mode of sensing is electromagnetic induction (EMI) and magneto-quasistatics is the appropriate physics [15]. In some instances we will apply alternative expressions for $T_{targ}(f)$. However, in all cases the target is assumed to respond like an infinitesimal dipole, with moment proportional to $T_{targ}(f)$. This target response is sandwiched between two identical environmental transfer functions, $T_{sw}(f)$, i.e. the net effect is $T_{sw}(f)^2$. Because both Tx and target are assumed to act as infinitesimal (z-oriented) dipoles, we apply e.g. [31]

$$T_{sw}(f) = \frac{e^{-ikr}}{2\pi}\left[i\frac{k}{z^2}+\frac{1}{z^3}\right] \tag{47}$$

in which *z* is the sensor-target separation or "standoff" (m), and *k* is defined like the parameter κ in (46), but with σ, ω,μ pertaining to SW. Again, given different time exponent and geophysical display conventions, consistent signs and complex conjugations must be observed between different derivations of these transfer functions.

This expression in (47) derives from the more general expression for the magnetic field from an infinitesimal magnetic dipole in a possibly dispersive medium. Most generally, one may regard the formulation then as applying simply to the reference configuration of a Tx/Rx unit "talking" back and forth with a target, all within an infinite homogeneous medium. At the same time, we

have found in lab measurements Figure 37 that this expression also approximates the signal finite reasonably well when a magnetic dipole field passes through a laterally broad layer of SW.

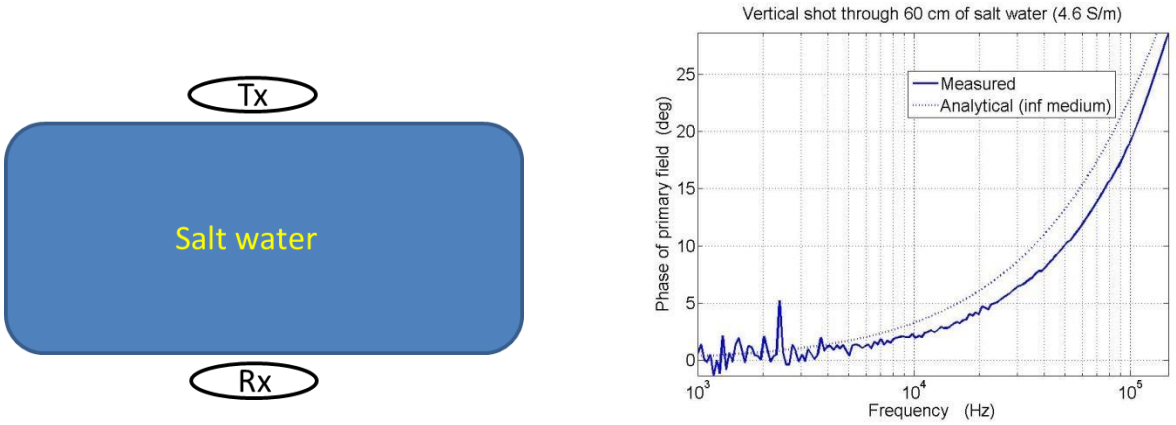

Figure 37. Phase of a field measured through a layer of SW vs that predicted for the same offset through SW by (47) .

Taken by itself, the product $T_{sw}(f)\, T_{targ}(f)\, T_{sw}(f)$ is in fact the impulse response, or "response spectrum" of the SWtarget-SW physical system. The remaining two factors constitute our instrumental excitation and reception processing of that system and may be considered together. We assume that the Rx is a loop antenna, such that it responds to the negative time derivative of the S(f), i.e. $T_{Rx}(f) = -i\omega$. (Unless otherwise noted, we leave off any scaling factors of these transfer functions because we are only interested in the relative form of signatures with respect to one another, subject to the same arbitrary scaling). If the Tx executes a unit-magnitude, perfectly vertical (instantaneous) downward step in time of its magnetic field, then $T_{Tx}(f) = U_{\infty}(f) = -1/i\omega$. Altogether then, under these assumptions, the instrumental effect is $T_{Tx}(f)\, T_{Rx}(f) = 1$, and the sensor recovers the impulse response of the physical system. In reality, while in fact our expression for $T_{Rx}(f)$ may apply quite well, the Tx shutoff is not quite instantaneous. Rather, $T_{Tx}(f) = U_{off}(f)$, where the latter consists of some finite-duration shift from "on" (+0.5) to "off" (-0.5). A handy, reasonably general rendition of U_{off} used here is

$$U_{off}(f) = U_{tanh}(f) = \frac{i/2a}{e^{\omega/2a} - e^{-\omega/2a}}$$

$$u_{tanh}(t) = \tanh(a\pi t) \qquad (48)$$

where a [s^{-1}]is a selected constant. In general, the time duration of the shutoff will be ~ $1/a$, see figures below. In most of what follows, we will apply (48) with $a = 3 \times 10^4\, s^{-1}$, i.e. shutoff

duration of ~ $t_s \sim 3 \times 10^{-5}\, s$ (Figure 38). This is long enough to be realistic but short enough so as not to distort signals unduly within the time and frequency ranges of interest.

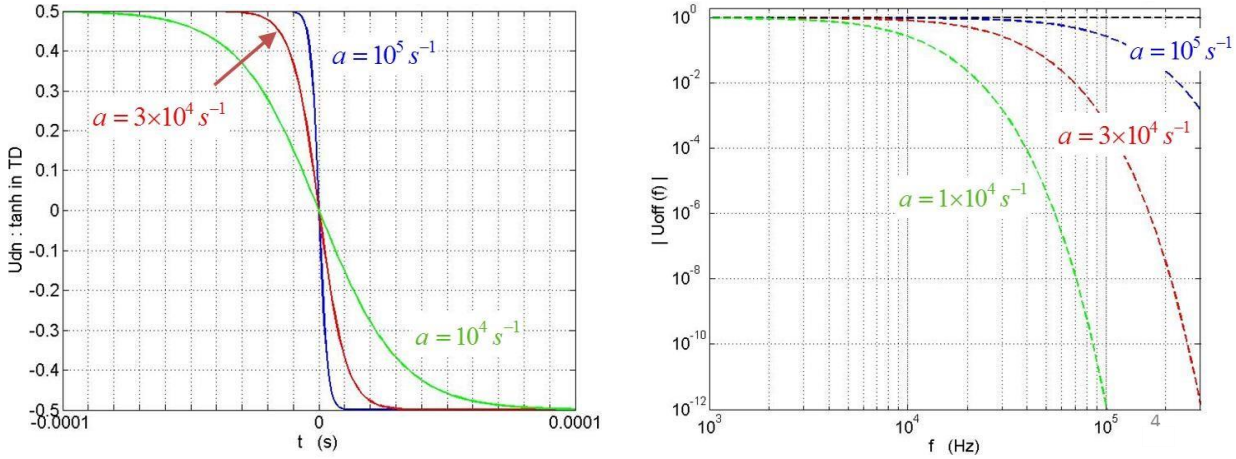

Figure 38. Left: $u_{tanh}(t)$ for various values of a. Right: $T_{Tx}(f)U_{off}(f)$, based on (48).

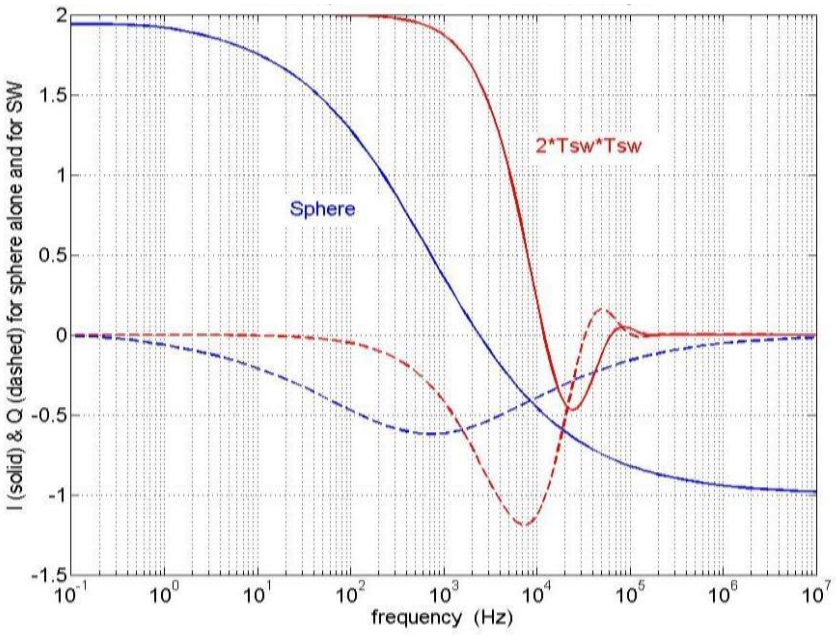

Figure 39. Blue: $T_{sph}(f)$ based on (45). Red: $T_{sw}(f)^2$, scaled by 2 for ease of graphical comparison, for a standoff z = 3 m.

5.8.3 Effects of target distance, composition, and disposition on TD responses

As a first case, we consider a spherical target based on a steel sphere in our lab (commercial shotput) about 11.3 cm in diameter. Applying (45) with $\mu_r = 100$, $\sigma = 5.33 \times 10^6 \, S/m$ produces the $T_{sph}(f)$ shown in Figure 39, which matched FD lab measurements well. The SW effect $T_{sw}(f)$ is squared to reflect the "round trip" that the signal must make, as per (42). Clearly, the $T_{sw}(f)^2$ factor will alter the product $T_{sw}(f)\, T_{targ}(f)\, T_{sw}(f)$ in roughly the upper (log) half of the range of the spectrum of $T_{sph}(f)$. Note that here $T_{sw}(f)^2$ will suppress expression of the highest frequency portion of $T_{sph}(f)$; the finite shutoff ($t_s \sim 3 \times 10^{-5} \, s$) will also suppress the highest frequencies, but neither of these multiplicative factors will have much specifically suppressive effect below some 10s of kHz, i.e after $t \sim 0.1 ms$ in the TD. The standoff distance z = 3 m was chosen because it produces a $T_{sw}(f)^2$ that overlaps substantially with $T_{sph}(f)$, and thus may alter its apparent signature. This is a large enough z value so that the SW might produce some effect but is not so large as to be entirely unrealistic. While this is a rather large EMI sensing distance, particularly for a target the size of a shotput, we note that a frequency response similar to the form of the $T_{sph}(f)$ shown would also apply to a target of the same material and same transverse diameter but greater length. That is, this (normalized) $T_{sph}(f)$ might be taken to represent a target the size of a 105 mm or 155 mm projectile, lying on its side and made of the same steel as the shotput.

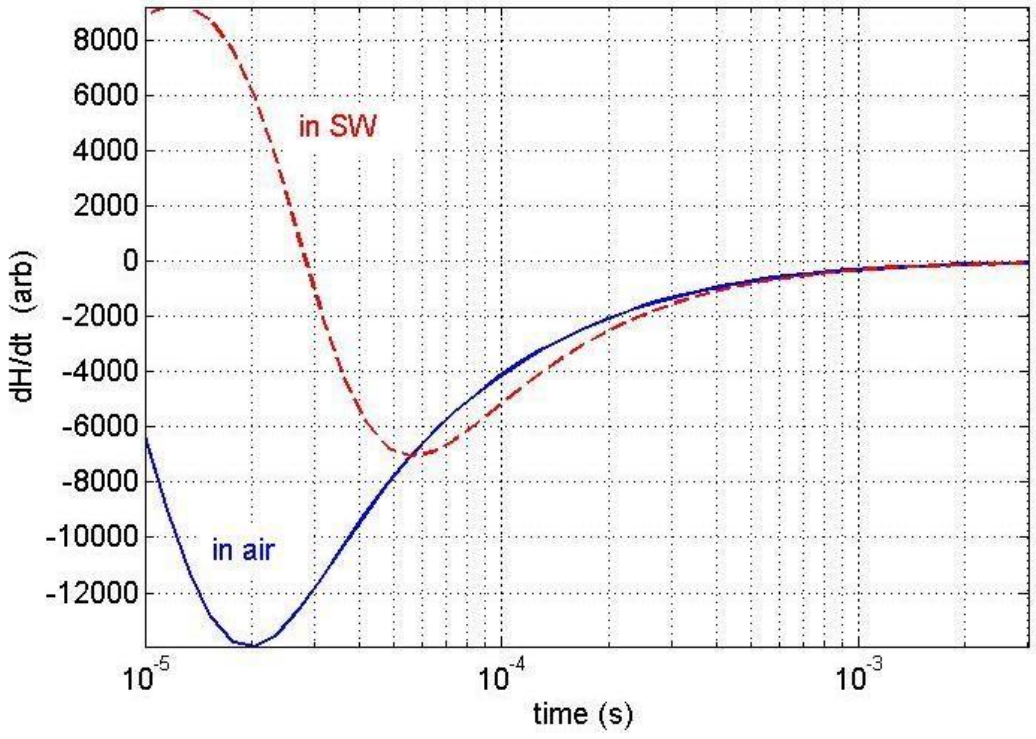

Figure 40. Computed, normalized TD response of lab shotput at 3m standoff shows the large magnitude of VET swings in value and characteristic, diffusive delay.

Before proceeding, we do well to recognize the overall shape of TD response that is to be expected over a range that includes VET. For the case at hand, with a shutoff that is essentially

complete by about $1.5\times10^{-5}\,s$, Figure 40 shows the response from VET until early MT. Here and in all subsequent plots of computed $\partial H/\partial t$ values, unless otherwise noted, results have been conveniently normalized. In particular, $T_{sph}(f)$ has been normalized as shown in Figure 39, and $T_{sw}(f)$ has been normalized by its value at the target, for lowest frequency applied, where SW has negligible effect. These conveniences are applied simply so that we may compare patterns, subject to the same scaling.

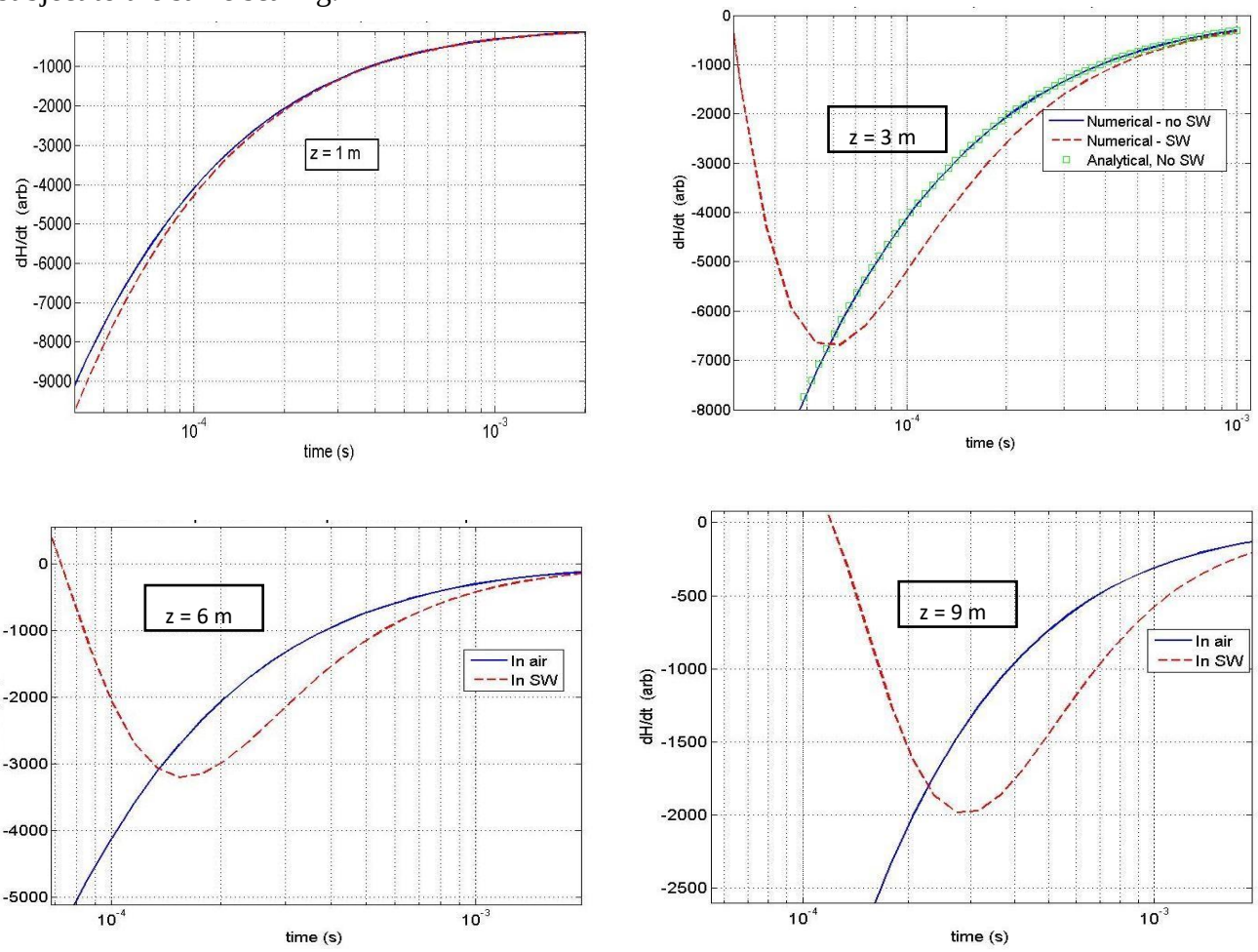

Figure 41. Calculated response of shotput at different standoffs *z* from the sensor. Blue: pattern in air. Red: pattern in SW.

Figure 40 illustrates that the change in magnetic field initiated by the Tx shutoff reaches the target, and S(*f*) then returns, by magnetic diffusion. Overall, classical diffusion solutions (see e.g. ref [32] or, geared more to the specific applications at hand, [15]) indicate that a sudden change imposed at a source or boundary will diffuse to an observation point L distance away according to the dimensionless number $t_d/\sigma\mu L^2$. That is, a point located L distance away from the forcing action will first experience some significant effect when this ratio surpasses $\sim10^{-1}$; diffusion to that point becomes more or less complete when the ratio approaches 1. Overall, diffusion serves to delay the dashed red curve (sphere in SW) relative to the blue curve (sphere in air). This says that the delay in each direction of the signals round trip will be $\sim 2 \times 10^{-5}$ s, for a total or about 4×10^{-5}s, which

we see in the plot. A particular point worth noting in the figure is that the region we are interested in, i.e. after 0.1 ms, actually only constitutes the trailing end of a much larger, earlier change in values. In other cases below as well as in many not shown, this earlier ($t < 10^{-4}\, s$) swing in values is frequently very much larger than later ($t > 10^{-4}\, s$) response magnitudes.

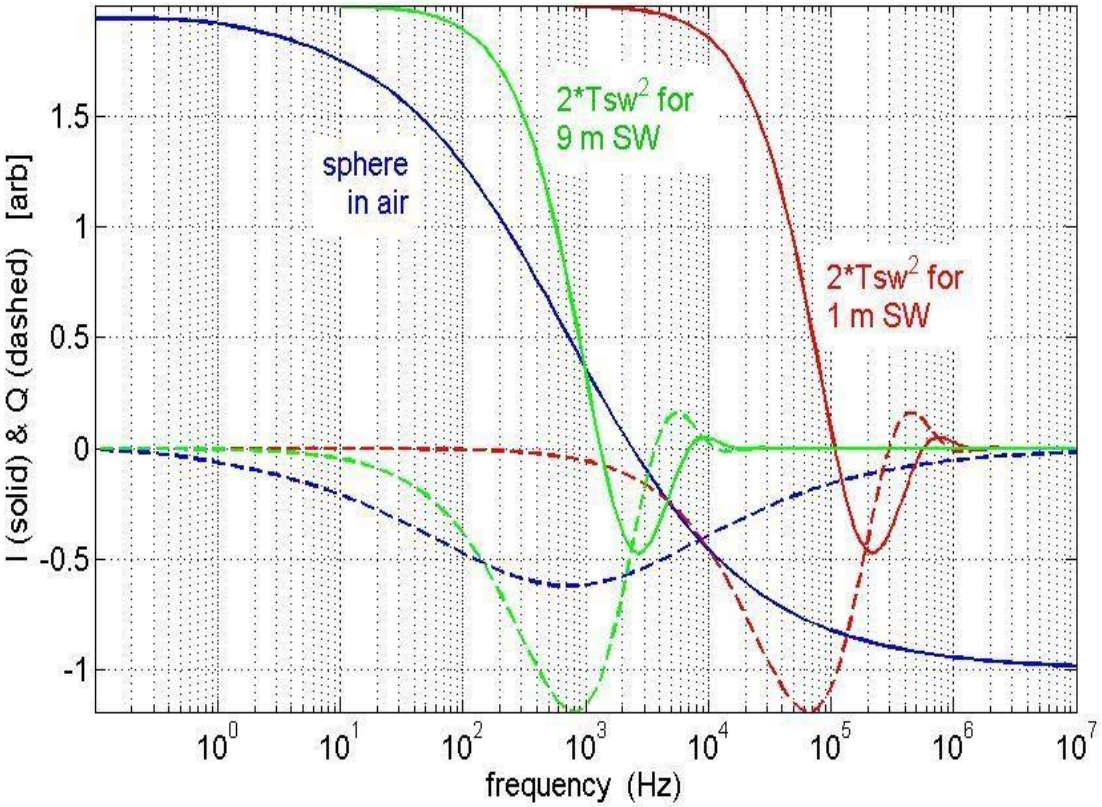

Figure 42. Normalized frequency response $T_{sph}(f)$ for the lab sphere in air, with $T_{sw}(f)^2$ for z = 1 and 9 m (scaled by 2 for plotting convenience).

5.8.4 Effects of distance

The factor $T_{sw}(f)$ depends strongly on the distance z (the "standoff") between the sensor and target, as per (47). The distance dependency appears both in the polynomial terms and in the exponential, increasing very nonlinearly as a function of frequency. Figure 41 shows the computed TD responses of our lab shotput through different distances, in either SW or air. The underlying interest resides in the fact that we would be seeking the inherent signature, i.e. polarizability of the target, as would be revealed by the values in air. Hence, the question is how much the presence of the SW engenders a signal that differs from the air pattern.

Figure 42 above shows the corresponding FD picture. At a standoff of z = 1 m, the activity in $T_{sw}(f)^2$ is shifted into the higher frequencies, above 10^4 Hz, so that one should expect no significant influence in the TD after 0.1 ms. Note that this will be the case regardless of the target being considered. At the other extreme, in the z = 9 m case, the effect of $T_{sw}(f)^2$ is at much lower frequencies, over the main response region of the sphere. Thus, its effect plays out later in the TD, through the beginning of MT. The 3 and 6 m standoff cases feature $T_{sw}(f)^2$ curves spaced between the two extremes shown.

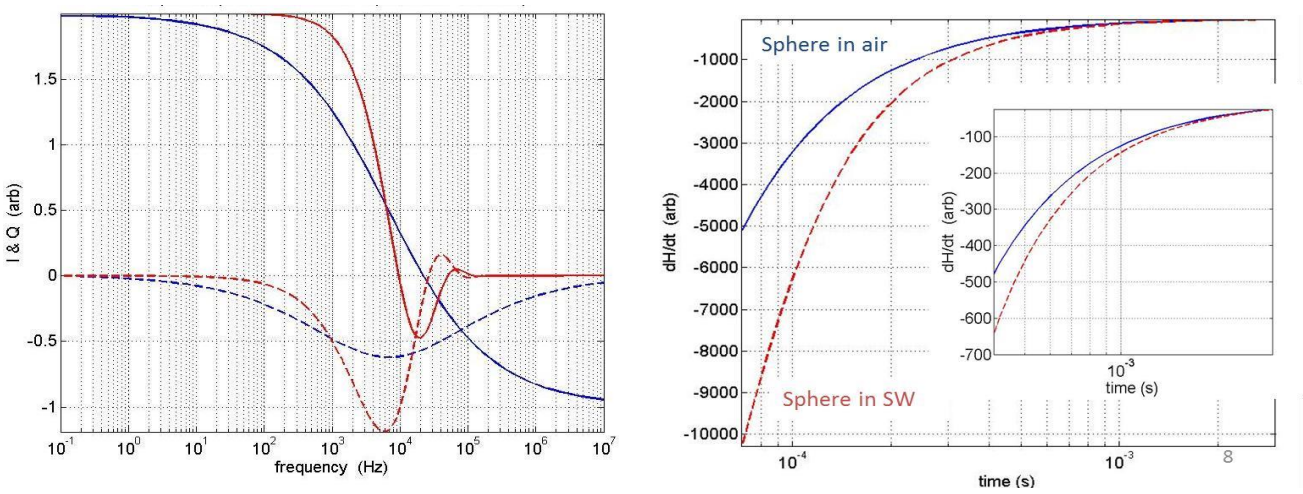

Figure 43 Left: Inphase (solid) and quadrature (dashed) response spectra for the reference sphere (blue) and the SW, i.e. $T_{sw}(f)^2$(red). Right: computed TD responses.

5.8.5 Effects of object composition

To examine effects of object composition, we begin by considering the sub-sea-bottom sphere in Ref [33], Here, however, we consider the object to be immersed in the SW itself. Further, rather than the large diameter of 60 cm assumed in [33], we assume one here more in line with that of a typical large UXO. Together with electromagnetic properties, the radius of a sphere determines the shape of its frequency response. However few UXOs have such a (60 cm) radius of cylindrical curvature, while many may have lengths comparable to 60 cm. Thus, here we retain the electromagnetic properties from [8] (μ_r =300,σ= 2× 10^6 *S/ m*) while reducing the diameter to 150 mm. Except in magnitude, this should produce a frequency response like that of a UXO-sized object, under transverse excitation and observation, made entirely of the reference steel. As we shall note below, particularly with reference to ferrous targets, elongation under axial observation produces quite different effects on the frequency response than does the diameter under transverse observation [34],[35].

Our newly-posited target produces a frequency response that overlaps the active region of $T_{sw}(f)^2$ quite thoroughly, at the same standoff used in Ref [33] (Figure **43**, left). This overlap produces

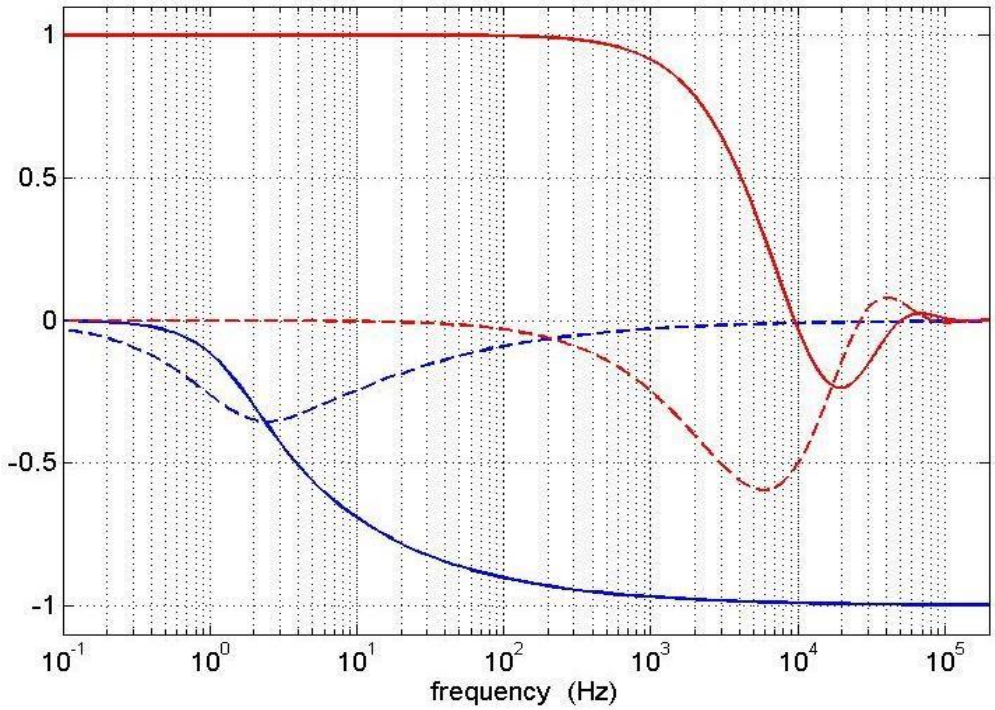

Figure 44. Inphase (solid) and quadrature (dashed) frequency responses of a 20 cm diameter copper sphere in air (blue) compared to the round-trip SW effect $T_{sw}(f)^2$ (red) at 3.35 m standoff.

quite striking effects in ET (Figure 43). The difference between the TD target signature in air and that in SW ranges between about 100% at the beginning of ET and ~ 10 – 20% near the end of it. Clearly target composition can have a significant effect on how much alteration of TD response will appear in SW. The target properties chosen above (particularly$\sigma\mu$) result in a $T_{targ}(f)$ shifted well into higher frequencies, relative to our lab shotput's pattern. As an illustration of the other extreme, a non-ferrous, highly conducting sphere (e.g. copper, $\sigma = 6\times10^7\, S/m$) of 20 cm diameter will feature a $T_{sph}(f)$ shifted very much into lower frequencies (Figure 44). The Cu sphere does indeed respond at the higher frequencies, however, that response is quite flat.

For all practical purposes, it is a magneto-quasistatic perfect reflector in that frequency range; and, what it "reflects" via the product $T_{sw}(f)\, T_{targ}(f)\, T_{sw}(f)$ is the response pattern of the SW. The active, relaxation regions of the two frequency responses are effectively disjoint. Excluding the $e^{i\omega t}$ time factor, the complete integrand in the inversion integral,

$$P_{int}(f) = T_{Rx}(f)\, T_{sw}(f)\, T_{targ}(f)\, T_{sw}(f)\, T_{Tx}(f) \tag{49}$$

is shown in Figure 45, left. The spectra are forced to zero at the highest frequencies in part by $T_{sw}(f)^2$, but also by $T_{Tx}(f)$, as a finite shutoff time of ~ 3×10^{-5}s is applied. The TD consequence of all this appears in Figure 45, right: the signals from the sphere with and without SW differ enormously in ET, being virtually identical thereafter.

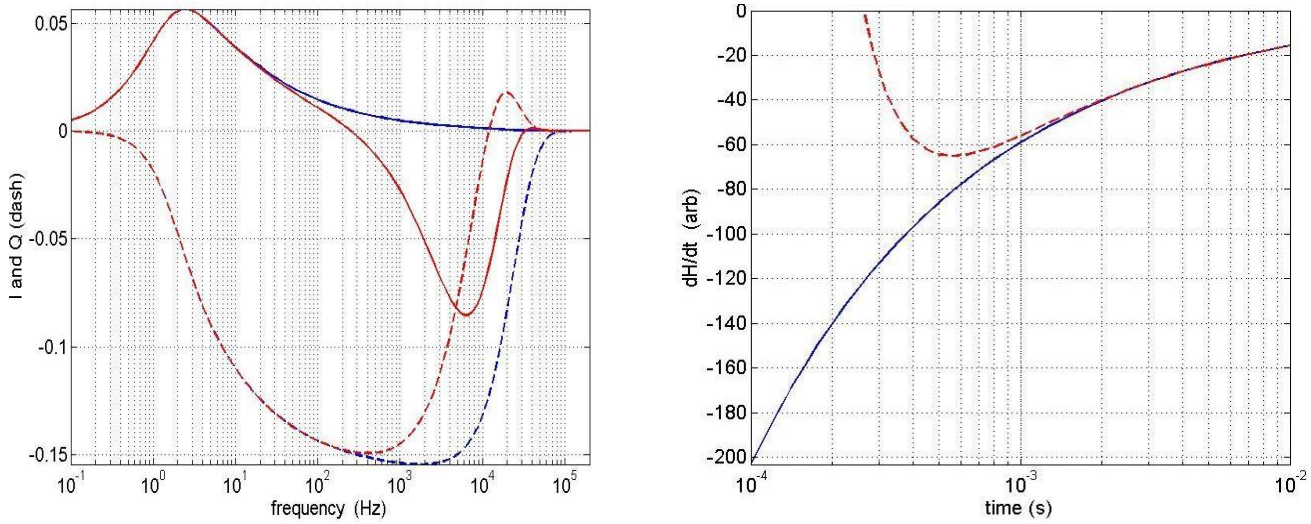

Figure 45. Left: Complete product in the inversion integrand, $P_{int}(f)$ for 20 cm diam CU sphere at 3.35 m, with and without SW effect. Right: TD inversion, with and without SW.

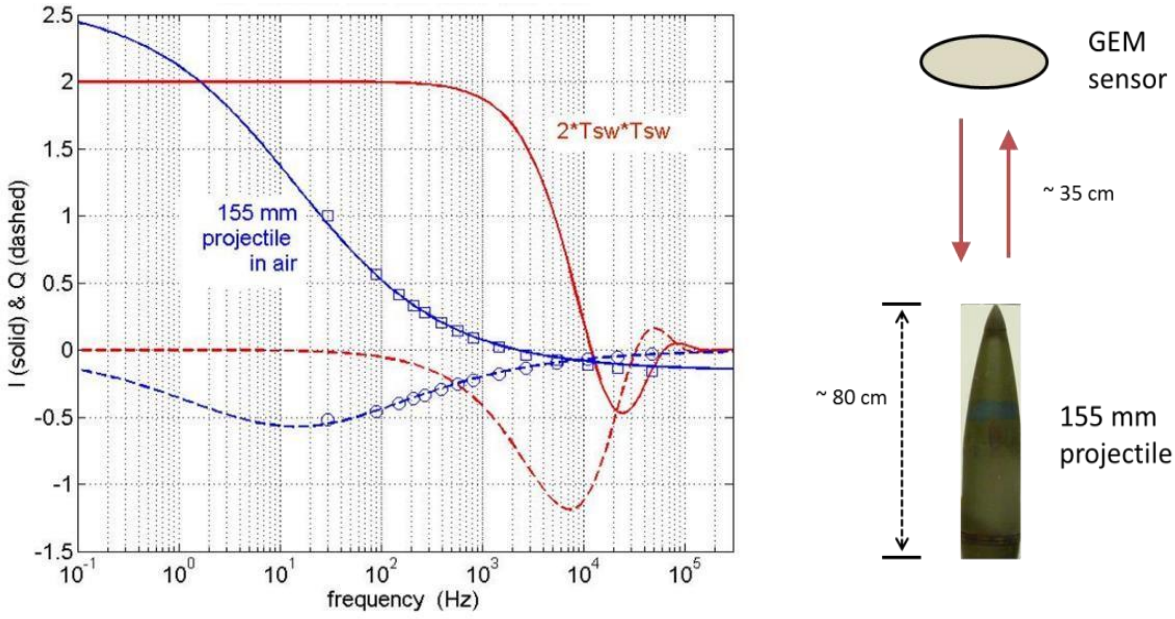

Figure 46. Left: Compared to $T_{sw}(f)^2$, the normalized axial frequency response of a 155 mm diameter projectile, as obtained by a GEM instrument, illustrated on the right. Markers: Measurement. Blue curves: semi-empirical model.

5.8.6 Effects of orientation

Inspired by the effects of this $T_{targ}(f)$ with strong low frequency content, we consider other cases of potential practical interest, specifically, ferrous objects. Above we have considered ferrous spheres and, by extension, cylindrical bodies with similar characteristics, subject to transverse observation. It is well established that elongated ferrous objects produce much stronger low frequency activity when viewed axially rather than transversely [34], [35]. Pursuing this, consider a 155 mm projectile's axial response (Figure 46). Marker values were obtained in the lab with a GEM-3 instrument [36]. The corresponding continuous curves for $T_{targ}(f)$, including extension below 30 Hz, were obtained by tuning convenient FD semi-empirical models [37].

In the lab configuration, the GEM response was dominated by the closer portions of the tip end of the projectile. Doubtless the UXO would produce a different (and probably lower-frequency) response if observed from a greater distance, so this response does not pertain broadly to the whole body. Be that as it may, this constitutes a handy, and an actual $T_{targ}(f)$ for a low-frequency responder. Figure 47 shows the complete inversion integrand, excluding the time factor, for z = 3 and 6 m, with and without SW. Compared to the Cu sphere responder (Figure 45), here differences in the details of target frequency response alter the picture. At z = 3 m, SW alterations of the higher frequency portion of the combined response spectrum are slight, causing a ~ 10% difference between the curves in the TD, entering ET. At 6 m standoff, alterations of the spectra are greater, with commensurately greater TD effects (~ 0.1 ms delay, ~ 25% difference in magnitude). Ultimately, the spectrum of the most active SW region and that of the target relaxation are not so disjoint as for the Cu sphere; the UXO also does not feature such a high-magnitude, very flat response at higher frequency as the Cu sphere does. The latter serves to amplify responses there.

Another UXO with ferrous content shows stronger high frequency response than the 155, while also retaining fundamentally lower frequency relaxation than is inherent in $T_{sw}(f)^2$. The 105 mm HEAT round (Figure 48) was sensed from a tail-end axial position with the GEM; we recall here the same caveats as to expected changes in the frequency response with greater standoff. Figure 49, left, shows that the SW effects do indeed produce strong alteration in the higher frequency range of the inversion integrand. However, while this is in part because $T_{targ}(f)$ is relatively strong in that range, it is not so flat as $T_{targ}(f)$ for the Cu sphere. Overall, examining the respective (155 mm vs HEAT round) FD response spectra does not offer ready explanations of why the corresponding TD responses differ as they do (Figure 45, right, and Figure 49, right). Perhaps in part, when multiplied times $T_{sw}(f)^2$, the $T_{targ}(f)$ pattern for the HEAT round does nothing to increase the uppermost frequency range of the integrand, but its curvature in the vicinity of 1 kHz serves to diminish the pattern of SW effect there. That is, relative to that for the Cu sphere $P_{int}(f)$ for the HEAT round shows SW effects compressed into a slightly smaller region of higher frequencies, hence earlier time. The sheer magnitude of SW effects in Figure 45, left, is also simply greater than in Figure 49, left. Generating larger VET excursions in signal following the shutoff (cf Figure 40), the SW effects for the Cu sphere may simply take longer to recede to the level of the underlying $T_{targ}(f)$ factor. In the very least, we can say these examples show that the finer details of an individual $T_{targ}(f)$ may interact with $T_{sw}(f)^2$ so as to produce substantially different effects in ET.

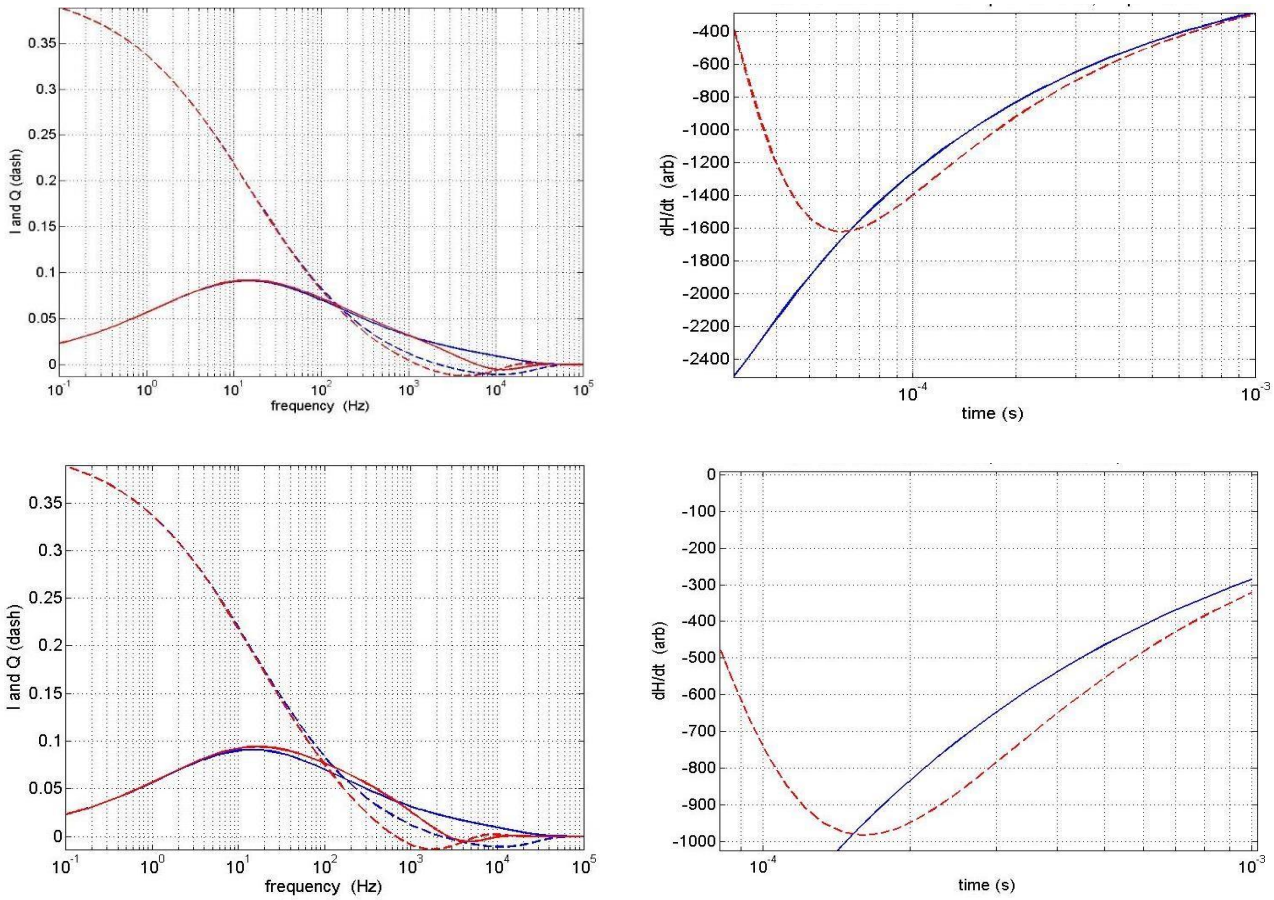

Figure 47. Responses, with (red) and without SW (blue), computed from the frequency response of a 155 mm projectile, with nose towards sensor. Top: z = 3 m. Bottom: z = 6 m. Left: Complete inversion integrand, $P_{int}(f)$, excluding the exponential factor. Right: TD equivalent.

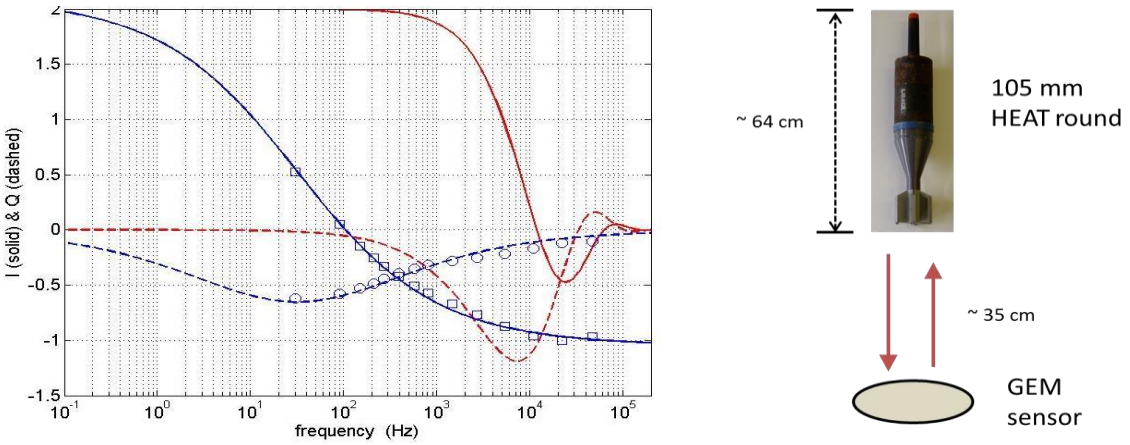

Figure 48. Left: the normalized frequency response of a 105 mm HEAT round (blue), as obtained by the GEM instrument, compared to $T_{sw}(f)^2$ (red). Markers: Measurement. Blue curves: semi-empirical model.

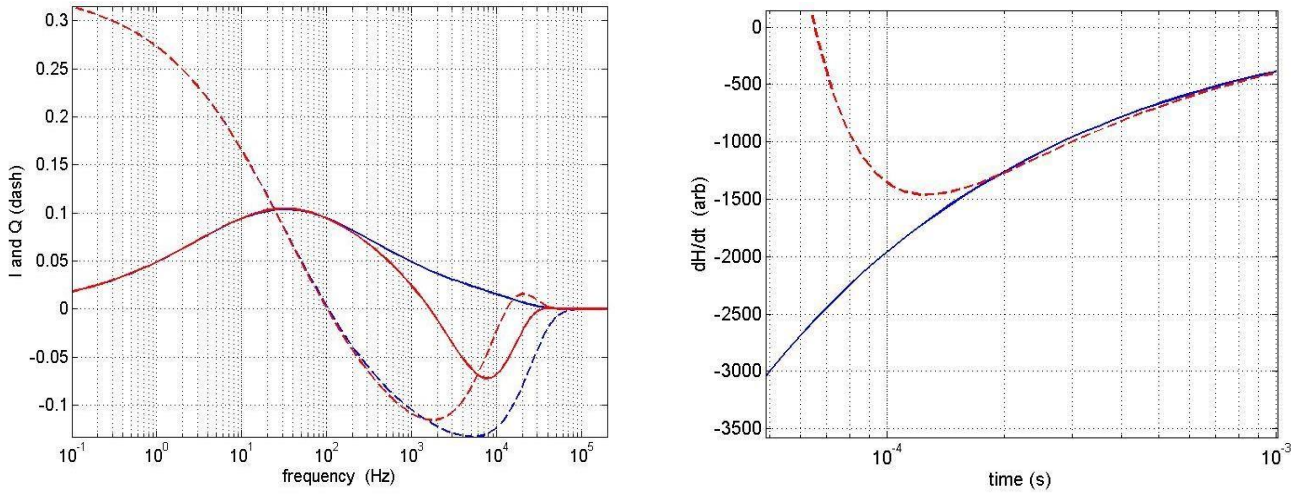

Figure 49. Left: complete inversion integrand, $P_{int}(f)$, excluding the time factor, for HEAT round, without (blue) and with SW (red). Right: TD equivalent.

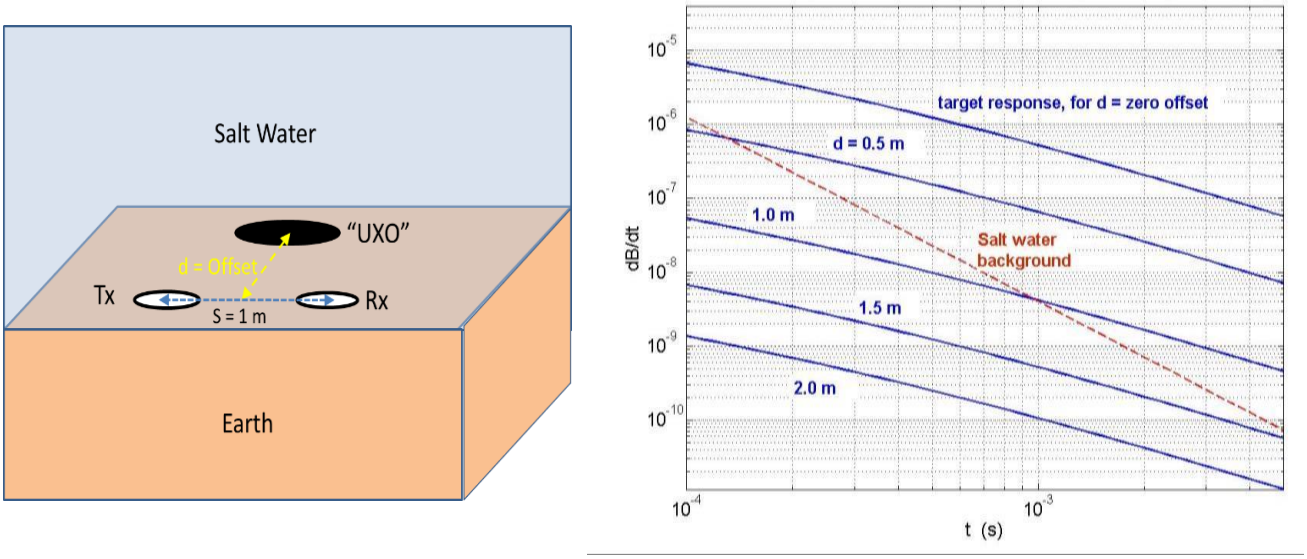

Figure 50. Left, a "UXO" target lies on non-conductive earth at water's bottom; a sensor with separated Tx and Rx sweeps over it through different offsets. Right: Comparison of the SW background signal to the S(f) signal from the target.

The preceding sections looked exclusively at the S(f) due to the target, assuming that it was possible to extract it from the complete received signal. Our goal was to discern the effect of SW on the concatenated fields produced by the sensor and target as those fields passed through SW. In practice, the complete signal will contain both the SW background response as well as the target's S(f). This section addresses the SW background signal, as regards both pattern and

magnitude, relative to that from a target. The test configuration is shown in Figure 50, left. The target lies on the surface of the non-conductive earth surface at water's bottom while the sensor sweeps along that surface as shown. Passing through different offsets, it ultimately sits directly over the target (d =0), with Tx and Rx on either side. The target is a "UXO" in the sense that it is a spherical responder with properties chosen to approximate the magnitude and pattern of frequency response for a prolate spheroid of about the size of a 105 mm shell, under transverse excitation. The sphere's "UXO-like" properties were determined by matching its response to numerical results for the spheroid using the MAS method [34], [35]: Thus, for the sphere, μ_r=100, σ= ×3 10^6 *S m*/ and its radius is 8 cm. To emphasize: the crucial feature of the modeling in this section is that we are concerned with both response pattern *and magnitude*. Hence, in this instance, $T_{targ}(f) \Rightarrow T_{sph}(f)$ is *not* normalized.

Further assumptions of this modeling exercise are that, because of the small standoffs considered, the environment has negligible effects on both the primary field impinging on the target and on its secondary field impinging on the Rx. That is, free space expressions are used for the Tx – target – Rx interaction. For the response at the Rx from the surrounding SW half-space, we rely on (44). Figure 50, right shows that the SW background signal follows a different trajectory from target's S(f), the former following a well-established $t^{-5/2}$ pattern. Overall, the complete signal at the Rx would consist of the sum of the SW response (dashed red curve) and whichever of the solid blue curves applied. The relative strength of the S(f) from the target alone varies greatly in magnitude, depending on how close the sensor is. At zero offset (Tx and Rx straddling the target), the target response is securely larger than the SW background signal over all time of interest. At 1 m offset, the background dominates through ET and only becomes a minor effect at times well above 1 ms. At 2 m offset, the background produces a much stronger signal than the target's S(f) over the entire range shown, from 3 orders of magnitude greater, entering ET, to about 1 order of magnitude greater at 5 ms. Overall, unless the sensor is very close to this quite substantial target, the background SW effect will be a much greater concern than the SW's effect directly on the S(f), as treated in the sections.

5.9 Analysis of the effect of salt water on time domain electromagnetic induction sensing

During the UW TD EMI sensing, the transient electric current (Figure 27) produces a primary EM field. The primary magnetic field penetrates in conducting surrounding environment and inside object (red lines). After a time τ_{on} interval, the Tx current is abrupted. As a result, eddy currents are induced inside conducting bodies, which in turn produce secondary magnetic fields at Rx coils, Figure 51. The total measured EMI signal is a sum of EM signals a) due to conducting water, i.e. direct signal (Figure 51-red lines); b) air-water and water-sediment boundaries (Figure 51 green and violet lines), and c) target (Figure 51 blue lines).

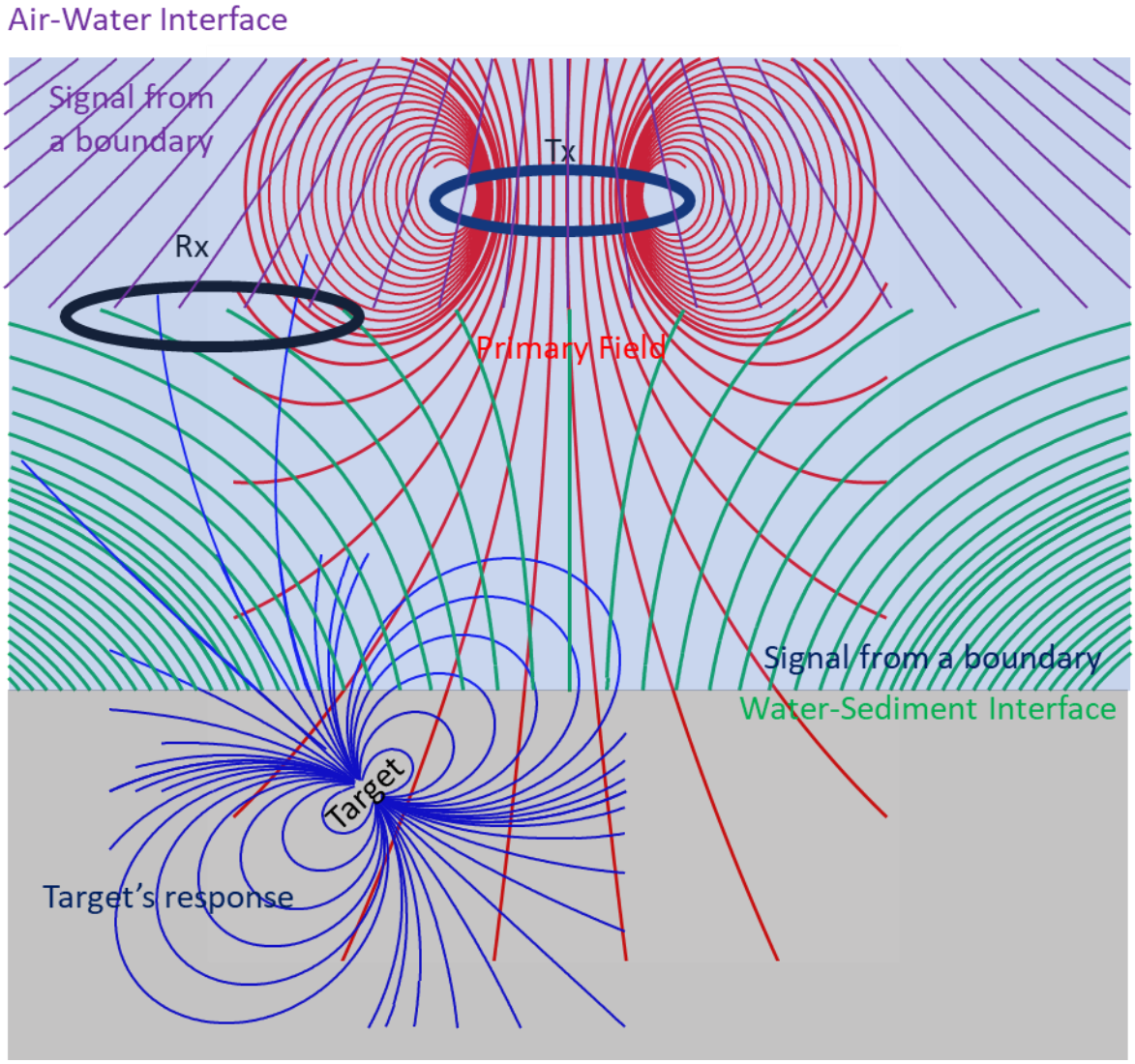

Figure 51. A Schematic diagram of the UW TD EMI sensing.

5.9.1 Primary field after transient Tx current turned off

Let us assume a 2mx1m rectangular Tx loop, carrying a transient electric current (Figure 27), is placed in a conducting environment (Figure 6). Figure 52 shows the calculated transient primary H_z (left) and H_x (right) magnetic fields vs time at x=50 cm, y=0 and z=1 m observation point, (Figure 7) after the transient current is turned off. For comparison, the calculations are done for Tx coil placed in the free space (σ=0) and σ= 5 [S/m] conducting water, and for various τ–turned off time, see eq. (41). These results show that at early time the magnetic fields in conducting water agrees with magnetic fields in air, however at later time the magnetic fields in water decay slower. Namely, H_z (left) and H_x (right) components of magnetic field decays as $t^{-3/2}$ and $t^{-5/2}$, respectively.

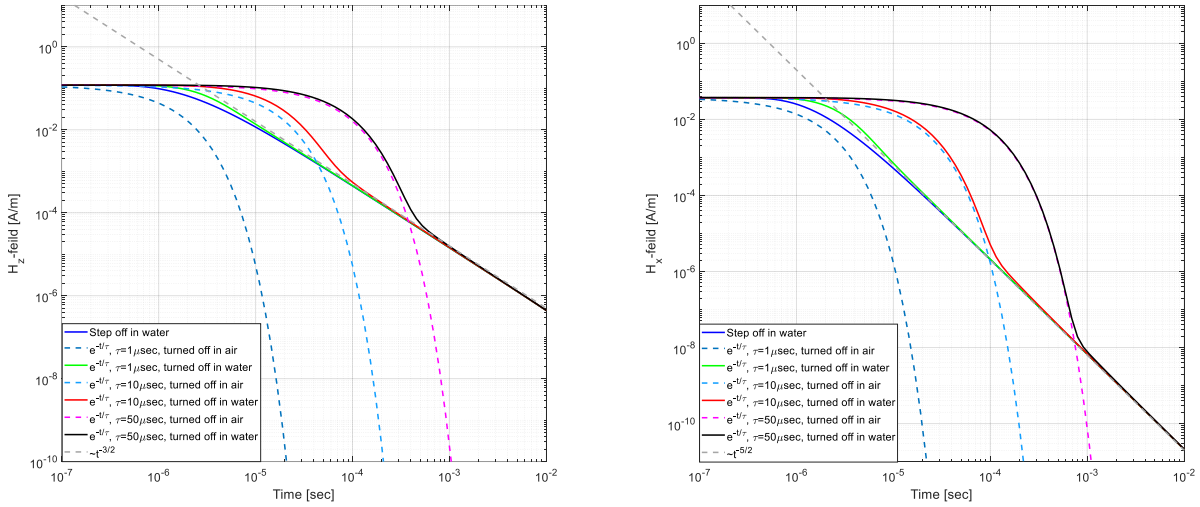

Figure 52. H_z (left) and H_x (right) complements of magnetic field in free space and in conducting environment for various values of t-turned off time, see eq. (41).

5.9.2 Comparisons between experimental and modeled data for direct, air-water and water-sediment responses

Our numerical calculations reveal that in a conducting environment the total measured EMI signal is the sum of signals produced by: 1) the transient current Tx current directly to Rx after the current is turned-off; 2) the air-water and water-sediment boundaries as shown in section 5.5; and 3) targets. To validate our calculated data, the numerical results were compared to measured data presented in the MR-2412 final report. The data were collected at various water depth within Moreton Bay using the UltaTEM system (Figure 53) built by GapEOD. The system consists a 2m x 1m x 1m fiberglass frame, two receiver cubes and one 2m x 1m rectangular, 12 turn, Tx loop placed about the same vertical level as the base of the Rx cubes. Figure 54 and Figure 55 show comparisons between modeled and actual data for background signals for the 2.5 m and 5.8 m water depths. The calculations are done for three (air-water-sediment) layered structure using the cylindrical plane wave decomposition model described in section 3.0 in frequency domain; The frequency domain signals are transformed in time domain using the sine transformation via Anderson's convolution filters [43].

Figure 53. Underwater tests were conducted in Moreton Bay near Brisbane, courtesy to MR-2412 final report, the photo is taken from.

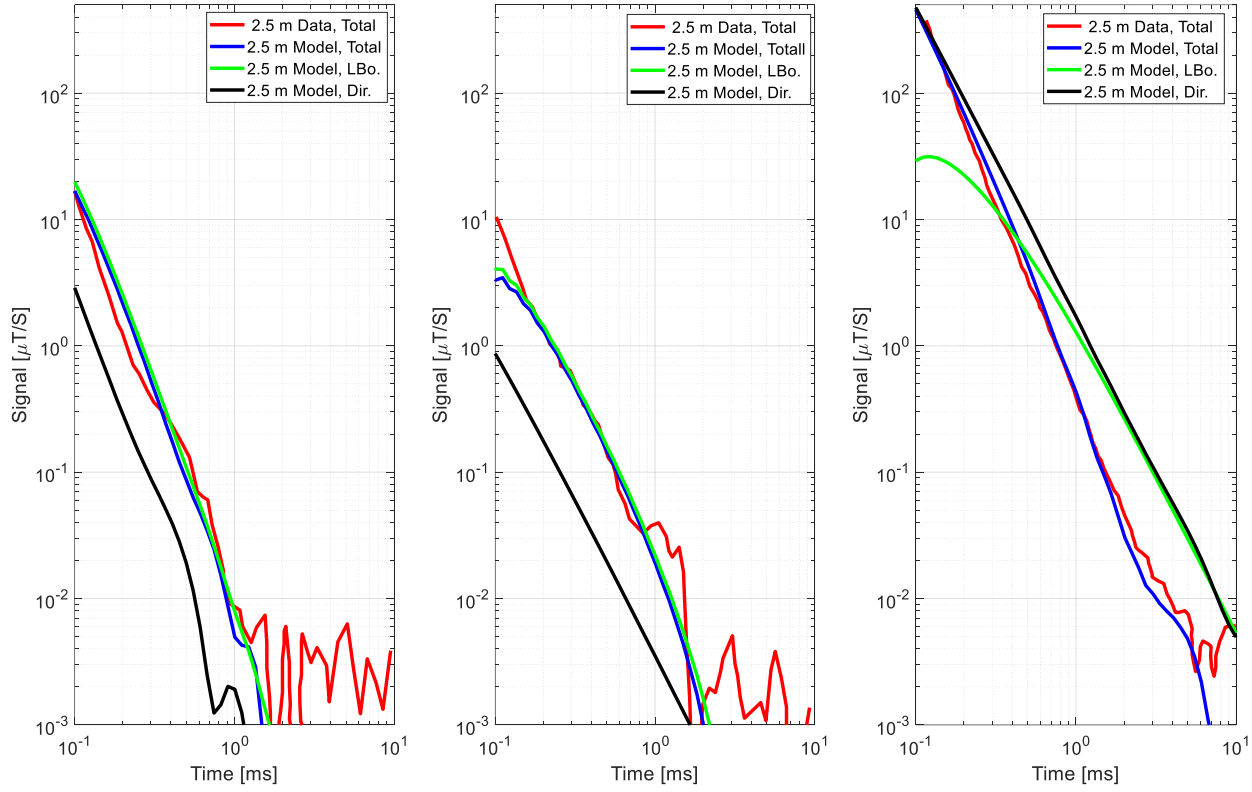

Figure 54. Comparisons between measured and modeled background signals at 2.5m water depth. The modeled signals are calculated using the three layer air-water-sediment structure. The modeled total signal (blue lines) is sum of signals from layer boundaries (green lines) and direct signals from Tx to Rx after transient current is turned off. Left: dH_x/dt, Center: dH_y/dt, and Right: dH_z/dt signals are calculated at x=40 cm, y=1 cm, z=5 cm point from the Tx center.

The conductivities of the three-layer air-water-sediment structure are σ_1=0 (S/m), σ_2=6 (S/m) and σ= 0.5 (S/m), respectively. The water conductivity σ_2=6 (S/m) was measured during data collections and provided in the MR-2412 final report. The sediment conductivity σ= 0.5 (S/m) was estimated from [44] by assuming a 2.4 g/cm^3 grain density and ~1.82 g/cm^3 wet-bulk density. Figure 54 and Figure 55 illustrate good agreements between experimental (red lines) and total modeled signals for the both 2.5 and 5.8 water depths. The numerical data show that modeled direct H_z signals (right graphs black lines) are about twenty times higher than combined signals from air-water and water-sediment boundaries (right graphs green lines). The magnitudes of H_x (left graphs green lines) and H_z (right graphs green lines) signals from the air-water and water-sediment boundaries are comparable, and due to Rx location, the magnitude of the H_y (center graphs) component is smaller than the magnitudes of the H_x and H_z components.

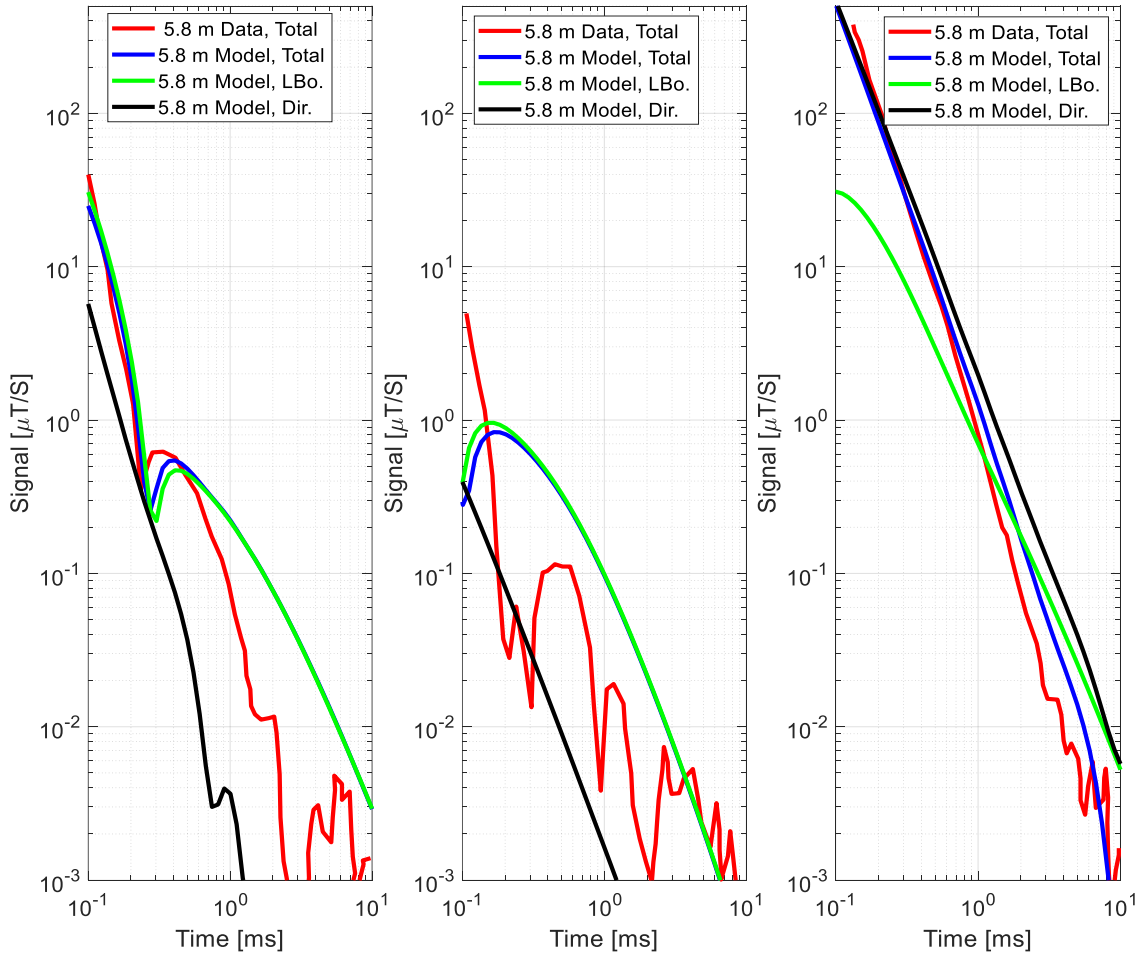

Figure 55. Comparisons between measured and modeled background signals at 5.8m water depth. The modeled signals are calculated using the three layer air-water-sediment structure. The modeled total signal (blue lines) is sum of signals from layer boundaries (green lines) and direct signals from Tx to Rx after transient current is turned off. Left: dH_x/dt, Center: dH_y/dt, and Right: dH_z/dt signals are calculated at x=40 cm, y=1 cm. z=5 cm point from the Tx center.

Figure 56: UAS EMI system: consists of four Tx coils. The radius of Tx-1 is 1.616 m, and radius of Tx2, Tx-3 and Tx-4 coils are 75 cm. It has high density polyethylene tubing, 3-D printed custom connectors and coils are threaded into tubes for protection, and contains nonmetallic parts.

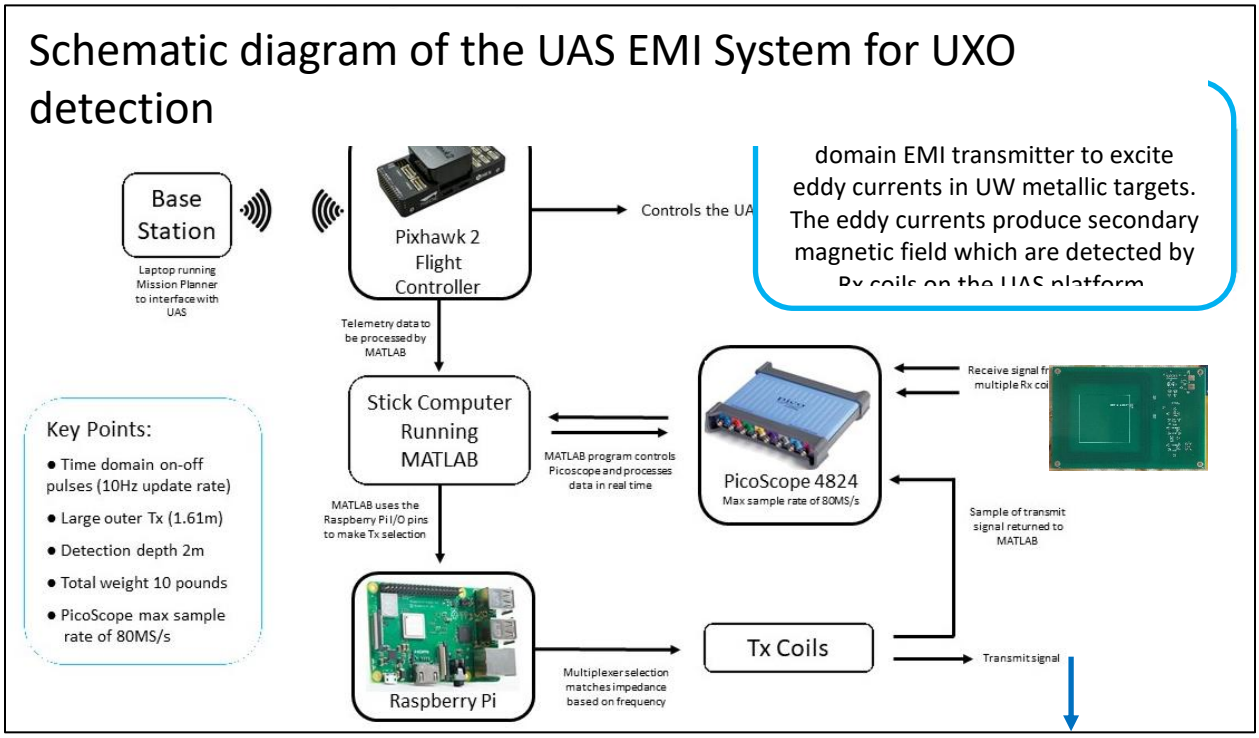

Figure 57. Schematic diagram of DAQ system; the system contains: a stick computer running Windows10; 8-channel Picoscope (max 80MS/s); custom Tx PCB stuffed and tested; Custom Rx PCB delivered; Rasberry Pi to control multi-Tx. Acustom-made Tx board using Mosfet technologies and optimally placed heat sinks for heat dissipation effectively

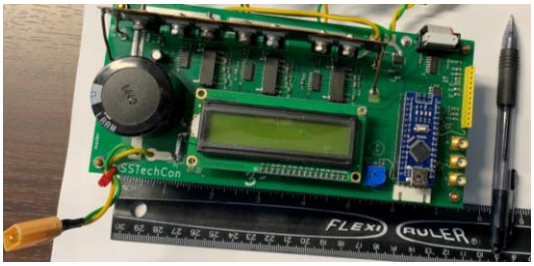

5.10 Experimental studies for UW targets

5.10.1 A sphere in a shallow sea water

To further validate above presented numerical data and understand how underwater environment affects on targets EMI responses we collect and analyze UW TD data set in an ocean shore at University New Hampshire Pier site. The data was collected using the lightweight time domain EMI system, which originally has been built as part of an ongoing AF project for detecting and identifying deep UXO targets at airfields using unmanned aerial system Figure 56. The system has four coplanar transmitter loops and three receivers. The system operates in both static (cued) and dynamic (on drone) modes, and the raw decay measurements are grouped into 30 logarithmically spaced time gates range from 80 μs to 10 ms. The Tx coils are activated sequentially using a microcontroller with custom-made electronics, and the received signals are collected at a combined sample rate of 80MS/s using a Picoscope 4824, that weighs around 1 pound (Figure **56** and Figure 57). Overall, the EMI system, that weights under 10 pounds, consists of one large and three medium size loops; The large Tx provides ability to detect deep targets, and multiple Tx coils help to classify targets. The system has in house built robust and lightweight (1 LB) Tx board. The Tx board provides up to 12 A currents with 40 μs turnoff time using MOSFET technologies and optimally distributed heat sinks for heat dissipation, see Figure 58. In addition, the system uses custom made small and lightweight 10 layer printed circuit 3-channel Rx amplifier boards (gain 400). The Rx, that is 7.5 cm square printed on each 10 PCB layer providing 10 tuns, is a low noise preamp, see Figure 59 and Figure 60.

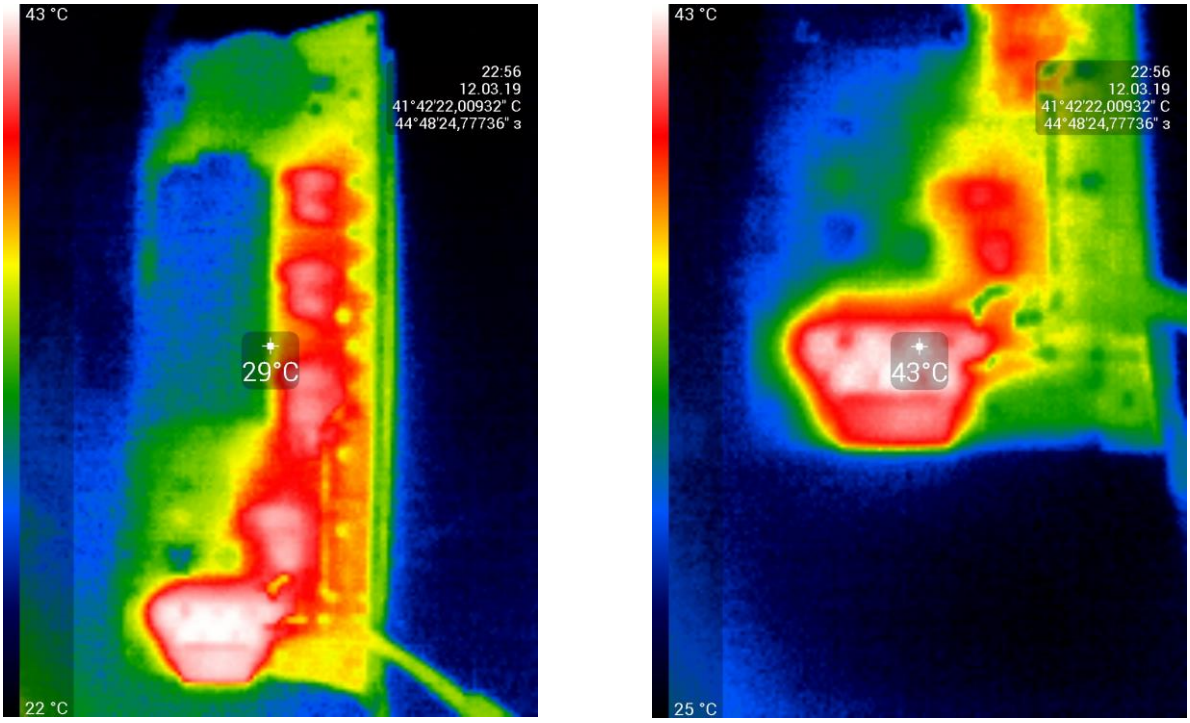

Figure 58. Temperature distribution map on the Tx board surface after 2 hours of continuously operating the system.

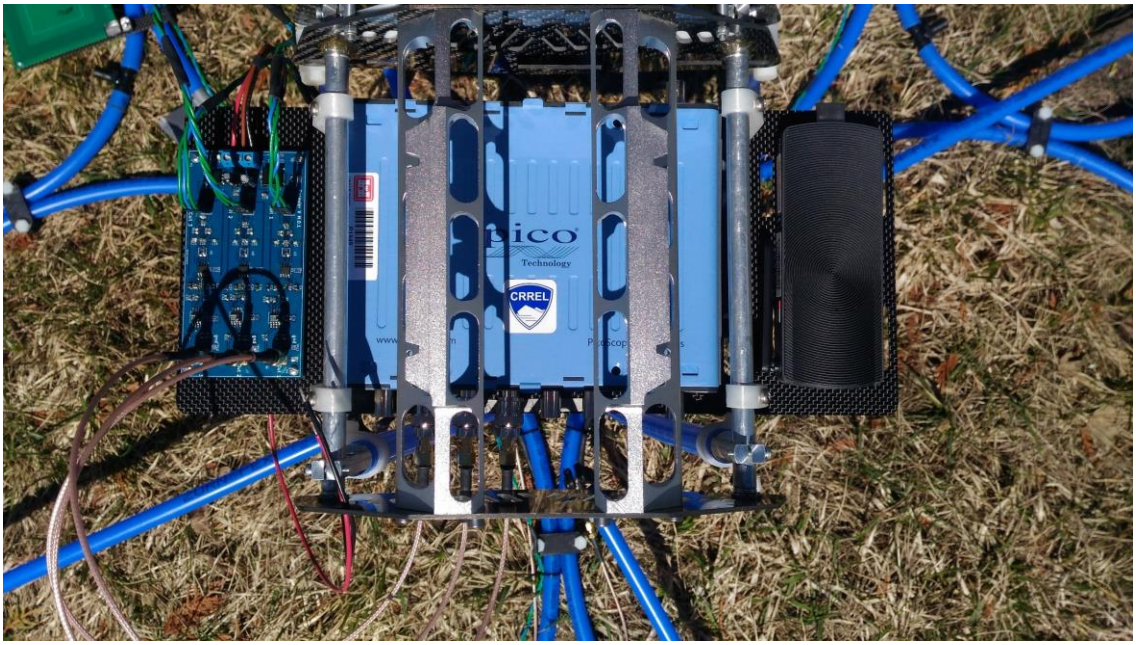

Figure 59. Rx pre-amplifier PBC (left) and picoscope (right)

Figure 60. 10 Layer Rx PCB (green)

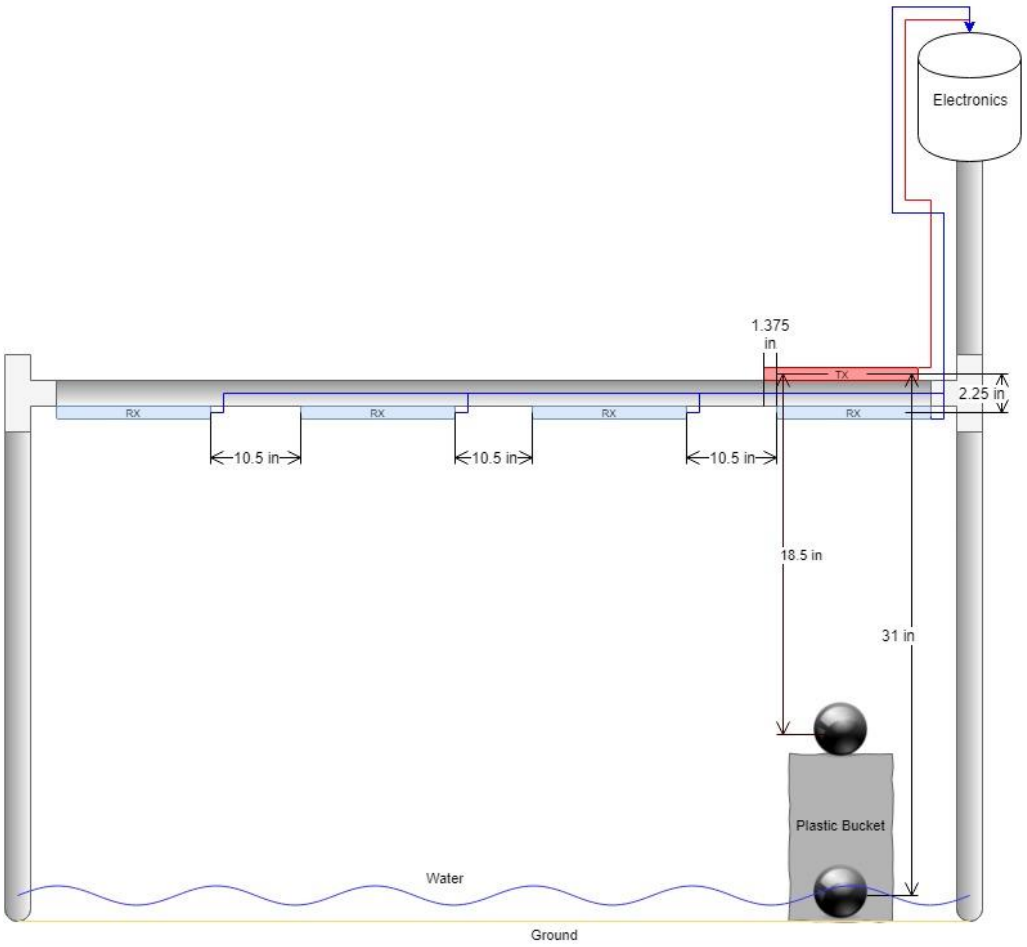

Figure 61. UW data collection setup.

Figure 62. Data collection site.

Figure 63. Underwater data collection for tidal ranges between 0 and 1 ft.

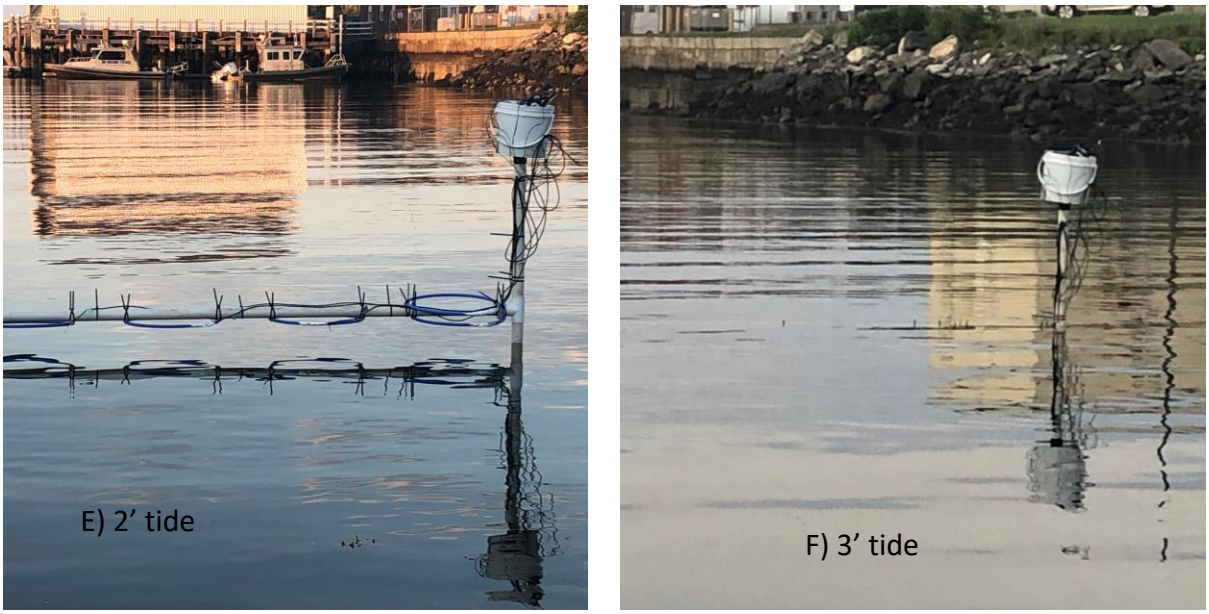

Figure 64. Underwater data collection for tidal ranges between 2 ft and 3 ft.

5.10.2 UW data collection

The time domain UAS system was modified and used for UW data collection. The experimental data collection setup is depicted on Figure 61. The data were collected at University NH pier site, see Figure 62, for different tidal ranges. i.e. both Tx and Rx-s were in air (low tidal range, Figure 63) and were submerged in water (from 1’ up to 3’ tidal range, Figure 64). The DAC electronics were housed in a bucket. The EMI signals were recorded using single z-axis circular Rx coils, Figure 61. The Tx/Rx coils are made with 22 AWG insulated wire and placed inside a ½ “ pex tube.

Figure 65 shows the measured EMI responses versus time for micro-tidal, water depth from 0” to 45 “. The results show that at low water depths (when both Tx and Rx-s are in air) the air-water-sediment boundaries do not produce noticeable signals, however when both Tx and Rxs are submerged in the seawater, than the influence of salt water are noticeable at early times. These results agree qualitatively with the numerical, analytical experimental results presented above. Namely, we have shown that there are several factors that can influence EMI signals in marine environments. The first effect is a transient response from the conducting seawater itself. The second is a change of the primary field at the target and a change of secondary magnetic field back to the receiver due to delays and dispersion of transient signals in conducting media. The third is the EM coupling between the conductive object and the surrounding medium. Studies have shown that these couplings are more significant at higher frequencies and depend on the material properties of the target, such as aluminum, steel, iron etc. And the fourth effect is transient responses from water-air and water-sediment boundaries. The results from the presented data illustrate that among these factors the change of the primary field from transmitter at the receiver

(direct coupling) due to delays and dispersion of transient signals in conducting media are dominant factor.

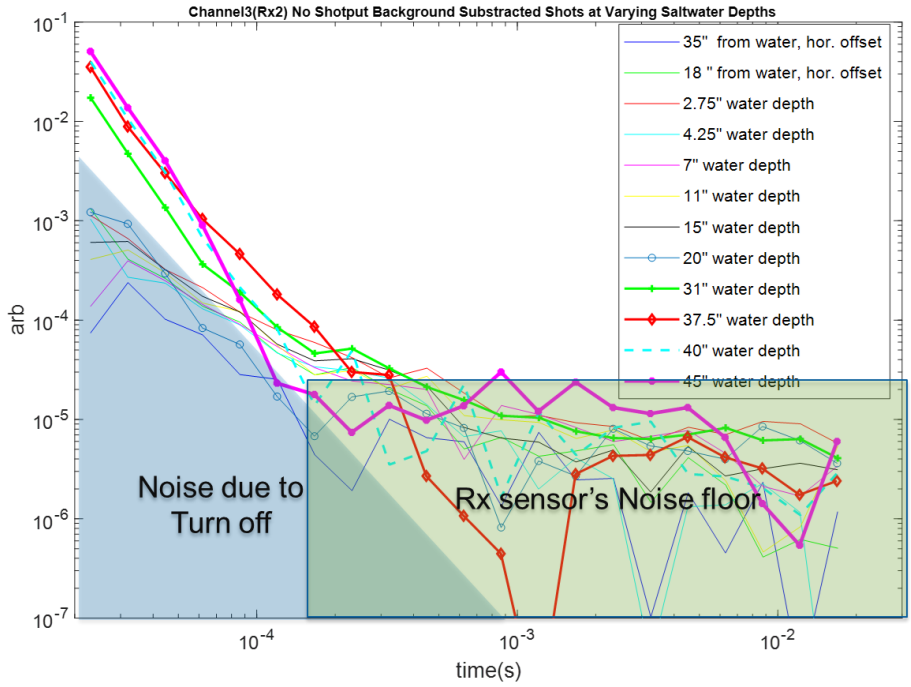

Figure 65. Measured EMI response for varying saltwater depths.

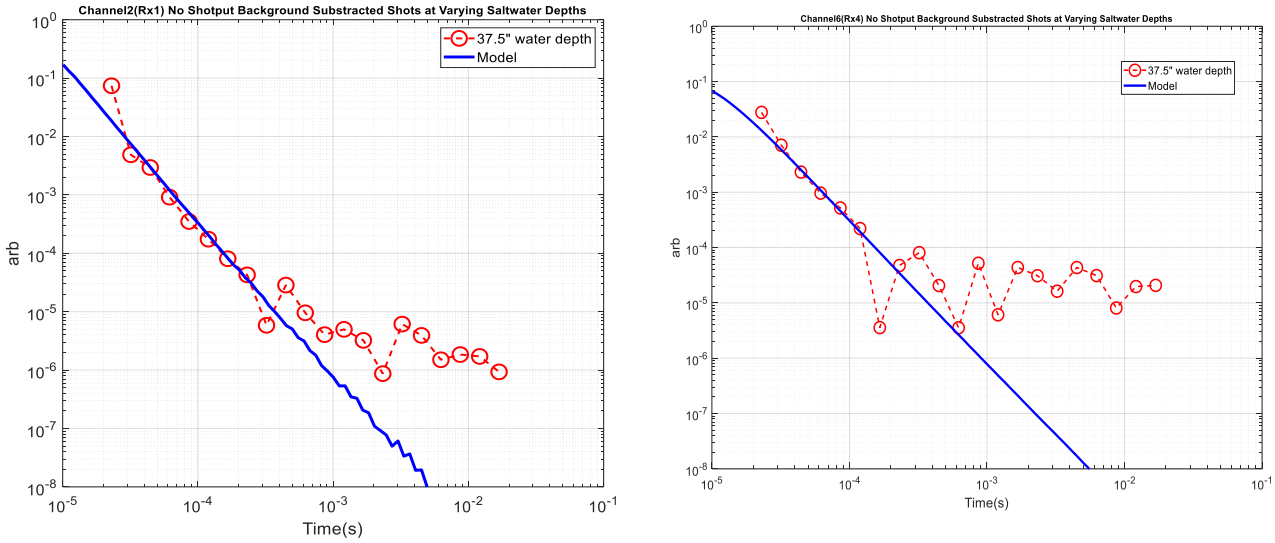

Figure 66. Comparisons between modeled and measured data for submerged Tx and Rx-s; Left: for Rx #2 and Right: for Rx #4, Figure 61.

Finally, we measured and modeled EMI responses for the permeable and conducting sphere. The sphere's geometrical and electromagnetic parameters are: diameter =11.3 cm in diameter and μ_r =100, σ=5.33 $\times 10^6$ *S/ m.* The comparisons between modeled and actual data for different water

depth are depicted in Figure 67 and Figure 68. These results show that spheres' EMI signals are distorted at early time gates, and the distortion move at later time gates when the distance between Rx and sphere is increased.

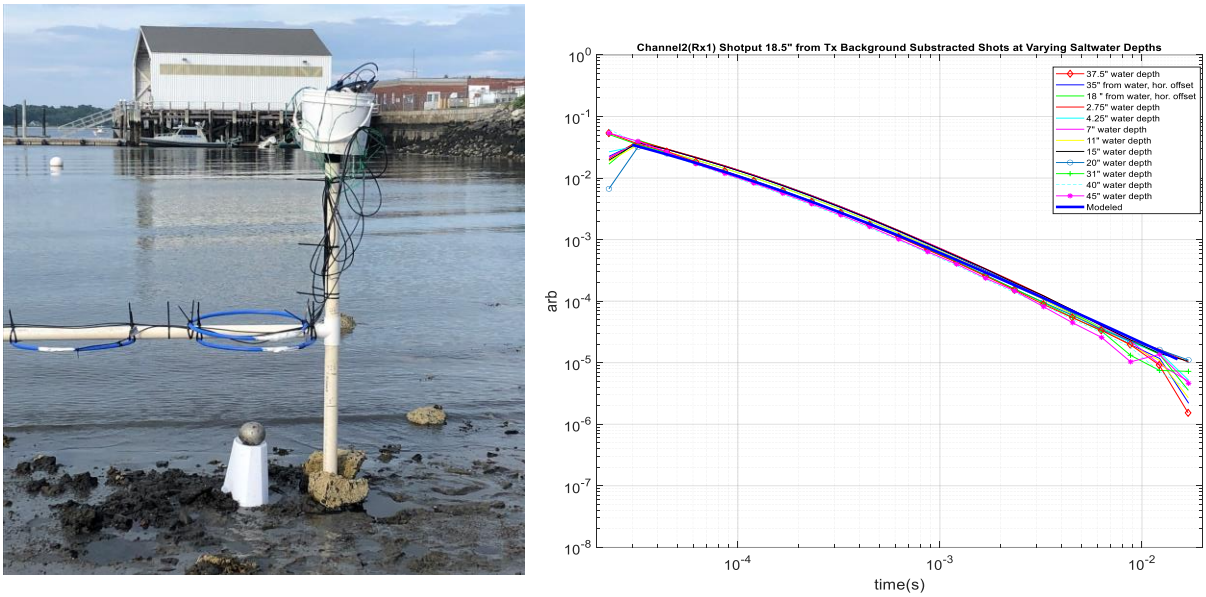

Figure 67. Left: experimental setup; Right: Modeled and measured EMI Responses for a sphere at varying Saltwater depths. The distance between Rx#1 and sphere is 18.6".

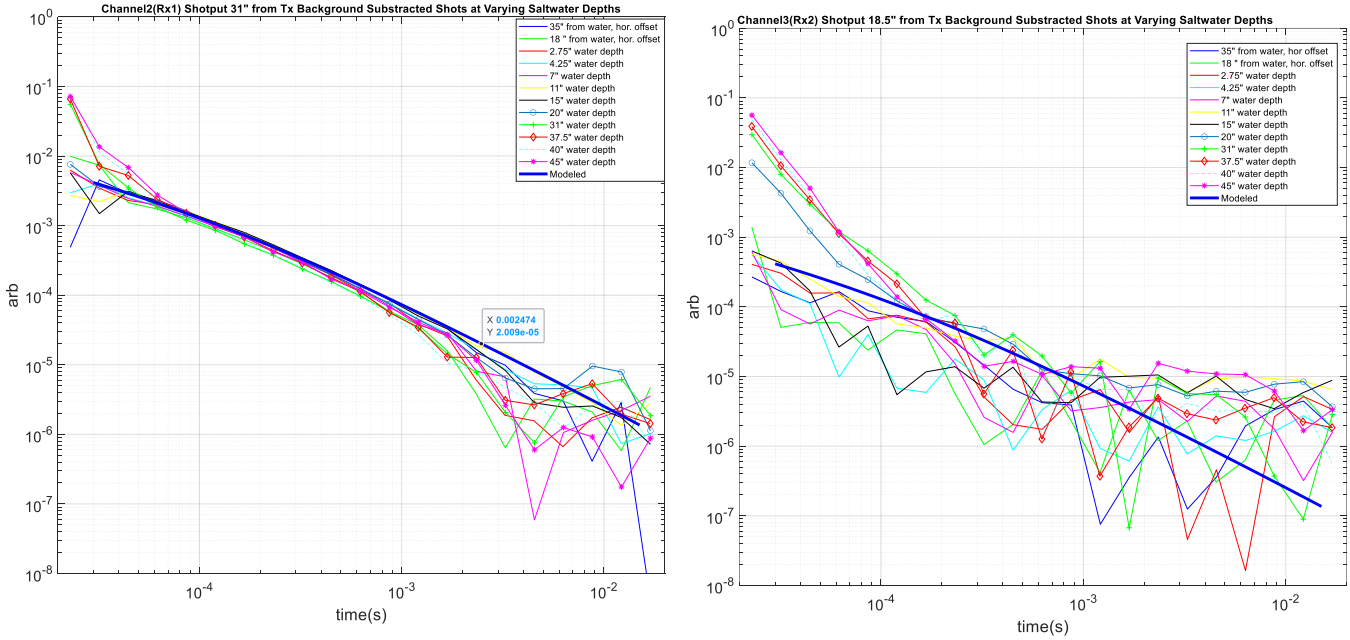

Figure 68. Modeled and measured EMI Responses for a sphere at varying saltwater depths; Left: the signal at Rx#1, the distance between Rx#1 and sphere is 31". Right: EMI responses at Rx#4; the sphere is placed at 18.6" depth and 47.5" laterally off set from the Rx#4 center, see Figure 61.

5.10.3 A 105 mm projectile in conducting environment

Under SERDP MR-2412 Dr. Billings and Dr. Lin-Ping have reported experimental data for a 105 mm projectile placed in both terrestrial and marine environments. They have showed that at later time (beyond 0.5 to 1 ms) the measured data in terrestrial and marine environment are virtually identical, but at early time the data revealed significant discrepancies between the received signals in these environments. The discrepancies were attributed to incorrect background measurement caused, in part, by the requirement to lift and then reposition the frame between measurements. In order, to further understand underline physics of observed data and validate the enhanced EMI models, presented in section 3.3, in this section EMI response of the 105 mm projectile are calculated for both environments and compared to actual data. First, time derivative $\frac{\partial \mathbf{m}(t)}{\partial t}$ of the principal components of the effective magnetic dipole polarization are obtained from the DoD library; then the time derivative of each principal component (Q' = primary, secondary and tertiary) is fitted to the empirical power decay-curves proposed by Pasion and Oldenburg in [45]

$$Q'(t) = \frac{\partial Q(t)}{\partial t} = k\, t^{-b} e^{-gt}. \tag{50}$$

The k, b, and g model fit constant parameters are extracted by via nonlinear least squares, with imposing the constraints $b > 0$ and $g > 0$ to preserve the physical essence of the data. Once these parameters are obtained then each principal component is calculated as

$$Q(t) = \int_0^t k\, \tau^{-b} e^{-g\tau} d\tau \tag{51}$$

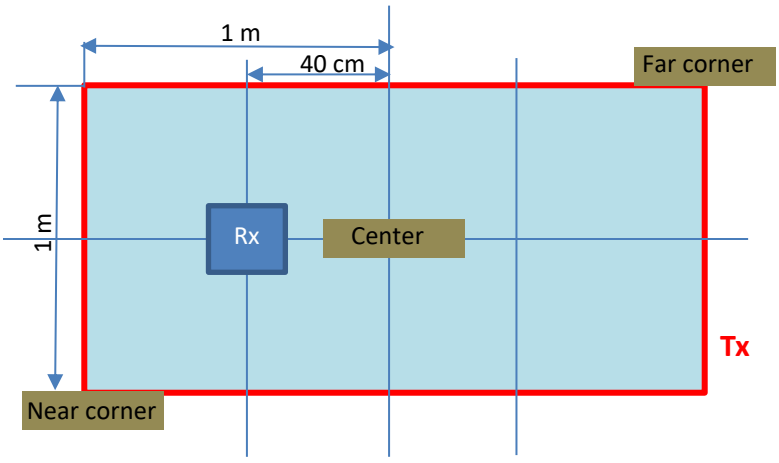

Figure 69. Left: top view of Rx, Tx and 105 mm placements (center, near and far corners) during UW data collection. Right: The UltaTEM system in terrestrial environment.

Figure **69** shows schematic diagram of UW data collection(**left**) and the ultraTEM (**right**) during terrestrial data collection for the 105 mm projectile placed at the bottom center of the frame. According to the MR-2412 final report, the data were collected over the 105 mm projectile placed at the bottom of frame at three position: center, near and far corners, see Figure 69. The measurements were taken for targets at the same locations in the terrestrial and UW environments. During UW data collection, the sensor frame was positioned on the sea floor. Background data were collected and subtracted for target's data. The comparisons between background corrected measured and modeled data for the 105 mm projectile at three different positions under the Tx/Rx frame are depicted on Figure 70. The results show good agreements between modeled and actual data for the 105 mm projectile for both marine and terrestrial environments. At early time gates (between 0.01 msec and 0.1 msec) EMI responses in marine environments due to magnetic dipole polarizability $\frac{\partial \bar{\bar{\mathbf{G}}}(\mathbf{r},\mathbf{r}',t)}{\partial t}\cdot \mathbf{m}(t)$ are about 100-fold stronger than signals for the same target in terrestrial environments due to its time derivative $\bar{\bar{\mathbf{G}}}(\mathbf{r},\mathbf{r}',t)\cdot \frac{\partial \mathbf{m}(t)}{\partial t}$ term. This different is significantly high and if these early time gate signals will be utilized it could increase UW targets detection depth at least twice.

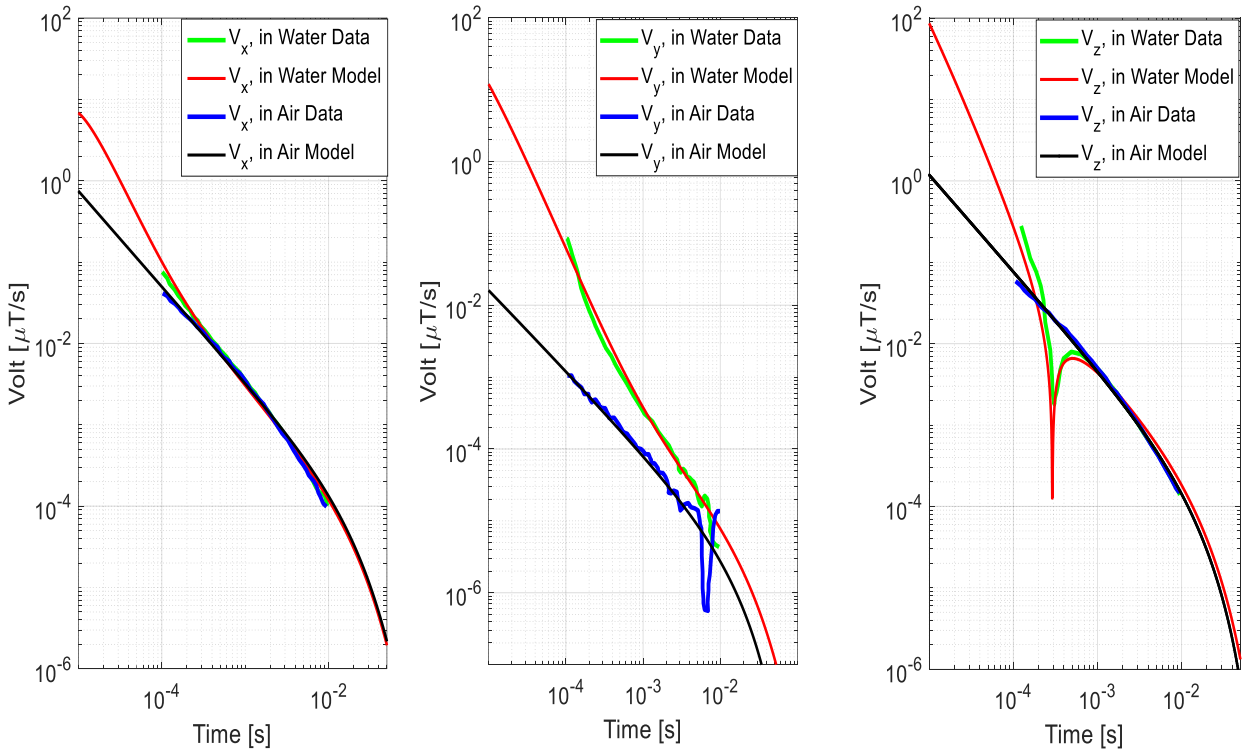

a) Center

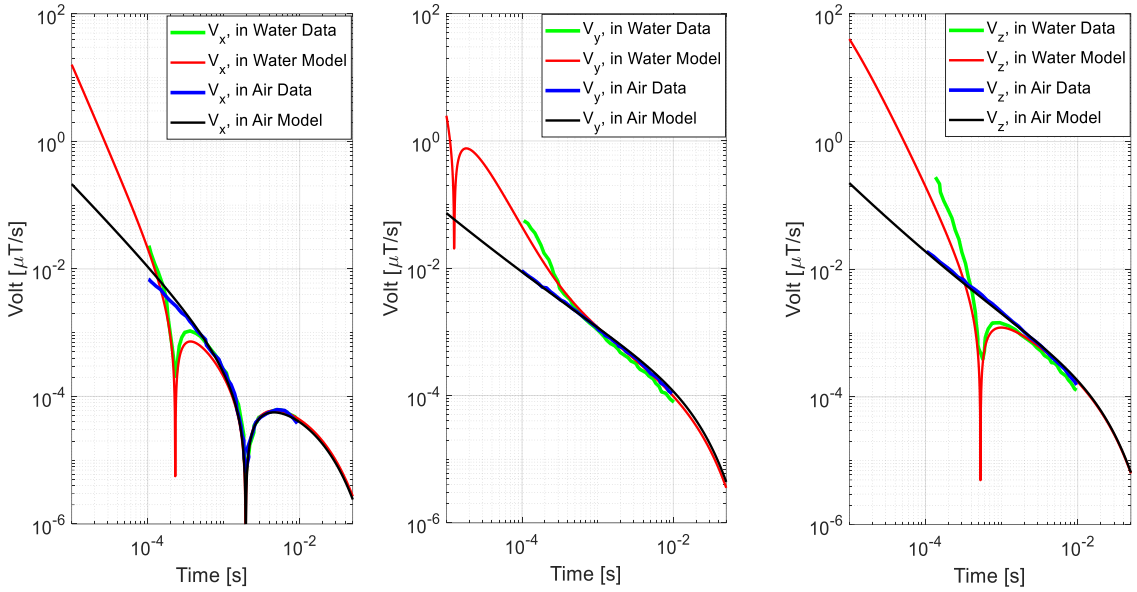

b) Near corner

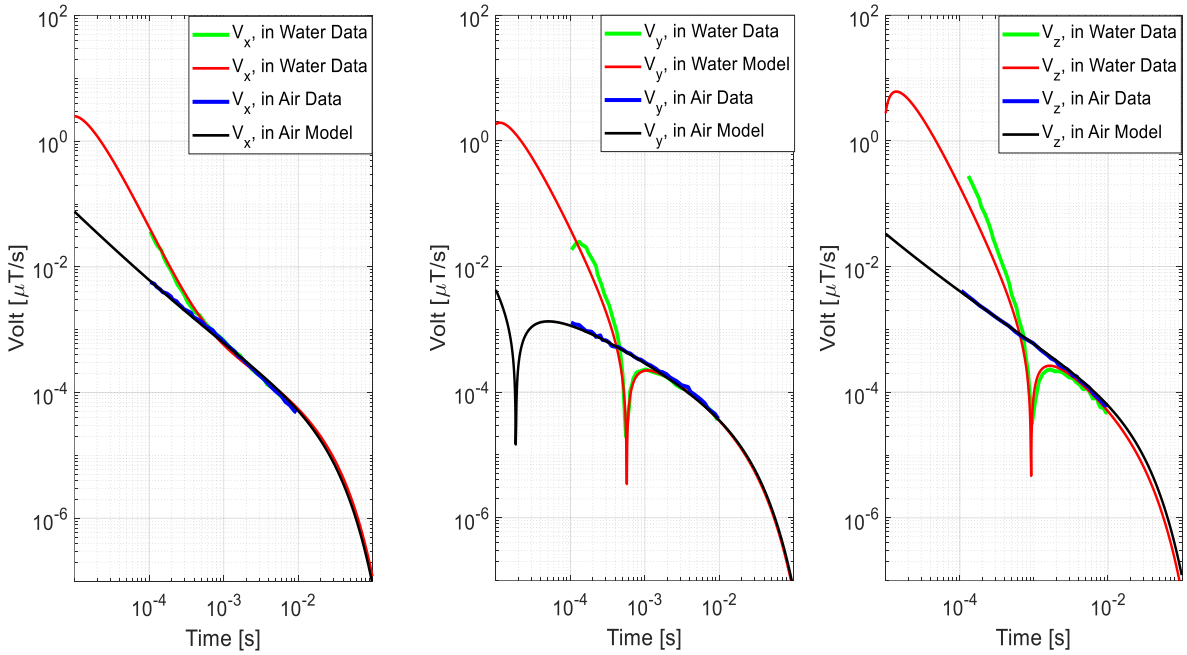

c) far corner

Figure 70. comparisons between modeled and measured data for the 105 mm projectiles placed in marine and terrestrial environments. The modeled data are obtained via the enhanced EMI model see eq. (11) . The conductivity of the water was assumed 6 [S/m]. The enhanced model predicts target's responses accurately for marine and terrestrial environments. (left: X component; center: Y-component, right: Z-component).

6.0 Underwater EMI data inversion

6.1 Underwater Advanced Time-Domain Electromagnetic Array

To illustrate applicability of our advanced EMI forward and inverse models for UW EMI data processing and targets classification, our models were adapted to UW EMI system, and used for processing UW data sets. The data were collected at Duck, NC underwater testing site using advanced time domain electromagnetic array Figure 71. The array was built under the ESTCP MR-201313 project. It consists of eleven, 10-centimeter (cm) three-axis receive cubes, denoted by the cube identifier and an "r" indicating "receiver" (i.e., Ar-Kr), seven 40-cm square transmit coils, denoted by the square identifier and a "t" indicating "transmitter" (i.e., At-Gt), and an outer 1.56-meter (m) square transmit coil (Ht). The resulting total number of data channels is 264. The raw sampling interval is 0.004 milliseconds (ms) and the recorded data are logarithmically averaged over 5 percent windows, resulting in 99 logarithmically spaced decay times ranging from 0.05 ms to 8.124 ms. One hundred measurements are averaged for each recorded measurement.

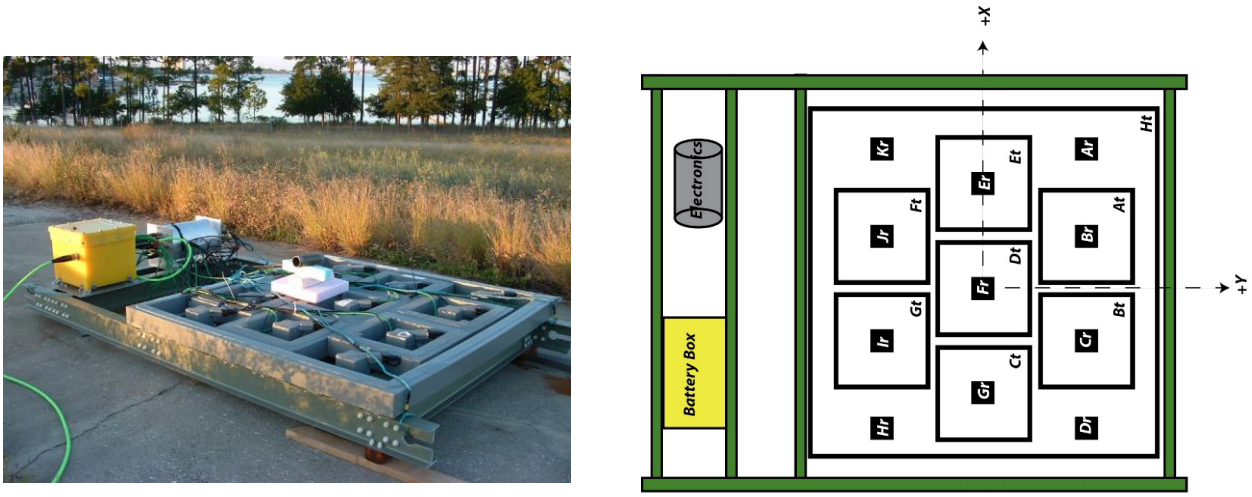

Figure 71: Right: A photo of underwater Advanced Time-Domain Electromagnetic System; left: the system' schematic diagram.

6.2 Ortho-Normalized Volume Magnetic Source Approach for UW EMI Data Processing

The ortho-normalized volume magnetic source (ONVMS) is adapted to UW EMI sensor data sets for modeling UW targets response. The ONVMS is physically complete, fast, accurate, and clutter-tolerant forward models for UXO discrimination. The model assumes that a collection of scatterers can be replaced with a set of magnetic dipole sources, distributed over a volume, that mimic the eddy currents and magnetic response that are induced on the targets by the sensor and that in turn establish the observable secondary field. These induced dipoles and currents are distributed inside the objects in question, and thus the spatial distribution of the responding dipoles (their amplitudes scaled by the primary field) traces a map of "response activity" with a clustering pattern that reveals the locations and orientations of the targets present within.

The time derivative of magnetic field due to the i-th source can then be expressed at any observation point **r** and time *t* as the matrix-vector product

$$\frac{\partial \mathbf{H}_i(\mathbf{r},t)}{\partial t} = \bar{\bar{\mathbf{G}}}(\mathbf{r},\mathbf{r}_i,t)\cdot \frac{\partial \mathbf{m}_i(\mathrm{t})}{\partial t} + \frac{\partial \bar{\bar{\mathbf{G}}}(\mathbf{r},\mathbf{r}_i,t)}{\partial t}\cdot \mathbf{m}_i(\mathrm{t}) \tag{52}$$

where the tensor Green function $\bar{\bar{\mathbf{G}}}(\mathbf{r},\mathbf{r}_i,t)$ and its derivative are $\frac{\partial \bar{\bar{\mathbf{G}}}(\mathbf{r},\mathbf{r}_i,t)}{\partial t}$ given in detail in equations (8) and (12). $\mathbf{m}(t) = \bar{\bar{\mathbf{M}}}(t)\cdot \mathbf{B}^{pr}$. The primary magnetic field $\mathbf{B}^{pr}$ from each (At-Gt) Tx coil to the i-th source location $\mathbf{r}_i$ is calculated using eq. (16). When there are several such sources, the total field can be expressed as a superposition:

$$\frac{\partial \mathbf{H}_i(\mathbf{r},t)}{\partial t} = \sum_{i=1}^{M} \bar{\bar{\mathbf{G}}}(\mathbf{r},\mathbf{r}_i,t)\cdot \frac{\partial \mathbf{m}_i(\mathrm{t})}{\partial t} + \sum_{i=1}^{M} \frac{\partial \bar{\bar{\mathbf{G}}}(\mathbf{r},\mathbf{r}_i,t)}{\partial t}\cdot \mathbf{m}_i(\mathrm{t}) = \begin{bmatrix} \bar{\bar{\mathbf{G}}}_1 & \bar{\bar{\mathbf{G}}}_2 & \cdots \end{bmatrix} \begin{bmatrix} \mathbf{m}_1' \\ \mathbf{m}_2' \\ \vdots \end{bmatrix} + \begin{bmatrix} \bar{\bar{\mathbf{G}}}_1' & \bar{\bar{\mathbf{G}}}_2' & \cdots \end{bmatrix} \begin{bmatrix} \mathbf{m}_1 \\ \mathbf{m}_2 \\ \vdots \end{bmatrix} \tag{53}$$

From the equation (53), the time derivative of the scattered magnetic field at any point outside a target's volume can be represented using a basis of orthonormalized functions as

$$\frac{\partial \mathbf{H}(\mathbf{r},t)}{\partial t} = \sum_{i=1}^{N_p} \bar{\bar{\psi}}_i(\mathbf{R}_i,t)\cdot \mathbf{b}_i' + \sum_{i=1}^{N_p} \bar{\bar{\psi}}_i'(\mathbf{R}_i,t)\cdot \mathbf{b}_i, \tag{54}$$

where $\mathbf{R}_i = \mathbf{r} - \mathbf{r}_i^{p}$, $\bar{\bar{\psi}}_i(\mathbf{r},t)$ and $\bar{\bar{\psi}}_i'(\mathbf{R}_i,t)$ belongs to the basis, $\mathbf{b}'$ and $\mathbf{b}_i$ are expansion coefficients. As a first step, the orthonormal functions $\bar{\bar{\psi}}_i$ and there time derivatives are constructed as Gram-Schmidt orthonormal linear combinations of Green's functions; the linear independence of tensor Green's functions then allows one to compute the amplitudes $\bar{\bar{\mathbf{M}}}_i(t)$ and their time derivatives of the polarizability tensor elements without solving a linear system of equations.

6.3 Global optimization technique for UW EMI Data Inversion

UW EMI data inversions are done using a combined ONVMS and global optimization (DE-differential evaluation) algorithm. Since, the scattered field from any object whose location and orientation are known depends linearly on the magnitudes of its responding sources, therefore the procedure starts by giving initial values of the attitude parameters and using these estimates, along with the measured data, to determine the source amplitudes by solving a linear system of equations. The amplitudes thus found are fed into a nonlinear objective function that quantifies the mismatch between measured data and model predictions and whose (DE-determined) minimum serves to refine the estimates for location and orientation. The procedure continues to alternate between

these linear and nonlinear stages until it reaches convergence (or a preset maximum number of iterations). The responding amplitudes are then stored and used in a later classification step, while the location and orientation parameters are used during target excavation.

Differential evolution uses N_p -dimensional parameter vectors **v**,

$$\mathbf{v}_{p,G},\ p=1,2,\ ...,\ N_p \tag{55}$$

where G is a generation/iteration index. In our case $\mathbf{v}=\{x_0,y_0,z_0,\theta,\phi\}$; the first three are the object's location and the other two are the polar (θ) and azimuthal (ϕ) Euler angles that define its orientation (by using only two angles we are assuming that UXO are effectively BOR). The objective function to be minimized is defined as

$$F(\mathbf{v})=\frac{1}{(MN_t)^2}\sum_{m=1}^{M}\sum_{t_c=1}^{N_t}\left|\frac{\partial H_m^{\mathrm{sc}}(\mathbf{v},t_{t_c})}{\partial t}-V_{m,t_c}^{\mathrm{data}}(\mathbf{v})\right|^2, \tag{56}$$

where $H_{m,t}^{\mathrm{sc}}(\mathbf{v})$ and $V_{m,t_c}^{\mathrm{data}}(\mathbf{v})$ are respectively the theoretical prediction (for vector eq. (54)) and the measured voltage data at the m-th Rx (of M) and the t_c -th time channel (of N_t). The DE optimization process itself can be subdivided into three steps:

1) The first step creates random initial populations $\mathbf{v}_{p,G},\ p=1,2,\ ...,\ N_p$, that span the entire parameter space. For a given $\mathbf{v}_{p,G}$ in the generation, a linear system of equations is constructed by matching measured data to the secondary magnetic field from (54). This system is linear in $\bar{\bar{\mathbf{M}}}_i(t)$ and is solved directly for those parameters.

2) The second step is the calculation of the time derivative secondary magnetic field (53) for each of the $\mathbf{v}_{p,G}$, which is computationally very efficiency and an attractive alternative for performing real-time inversion via the ONVMS technique.

3) Next comes the evaluation of the cost function eq.(56) for each population member and the storage of the best sets of parameters. At each step, the DE algorithm produces an estimate of position and orientation. By examining and sorting the cost function at each step, the best-half of the population is chosen as the next generation's parameters, whereas the bottom half is discarded. Thereafter the next generation is created by taking the parameters in the previous generation and applying crossover and mutation operations on them. The three steps are repeated until the maximum number of generations has been reached or until the objective function reaches a desired value.

6.4 Extracting UW UXO targets classification feature parameters

To illustrate the applicability of the combined DE -ONVMS for extracting UW UXO targets classification feature parameters, such as effective polarizabilities, we conducted studies in UW time domain electromagnetic array data inversion and discrimination. The data reported here were collected under the ESTP MR-201313 project at Duck, NC test site, and provided to us by Dr.

Steinhurst, of NAEVA, and Dr. Bell of Leidos. Figure 72 (left) shows target locations relative to the array during in-water measurements. The targets were buried into the bottom. Namely, small targets (37 mm, Small-ISO, 20 mm) were immersed in the seabed between 0 and 5 inches, and large targets were buried up a foot. The sensor was placed above targets stationary, and data were collected for target located under each six position. Figure 72 (right) and Figure 73 show comparisons between library and extracted effective polarizabilities for 81 mm projectile placed under positions 1,3,4,5 and 6. Similarly, Figure 74 and Figure 75 show extracted effective magnetic polarizabilities for a 37 mm projectile, 60 mm mortar, 81mm and 105 mm projectiles.

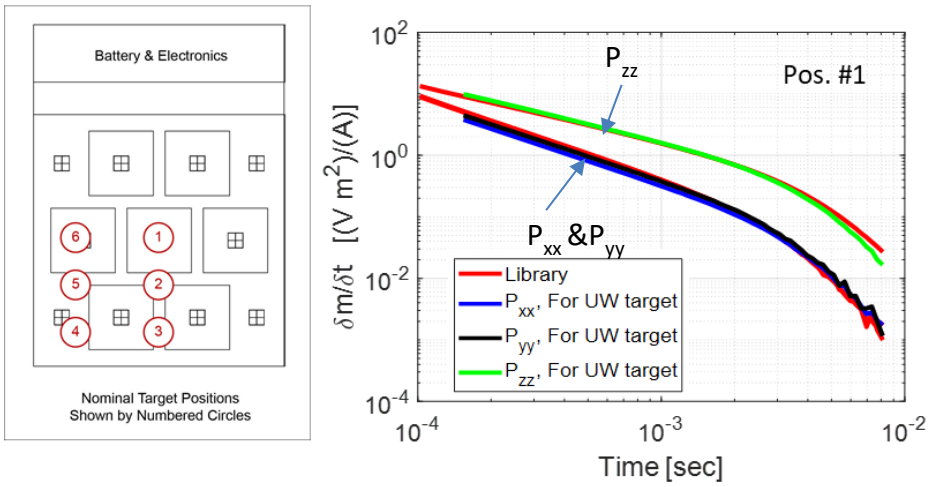

Figure 72. Left: UW target locations respect advanced time-domain electromagnetic array. Right: Comparisons between library and extracted effective polarizabilities for an 81 mm projectile placed under position 1 relative to the array in-water measurement.

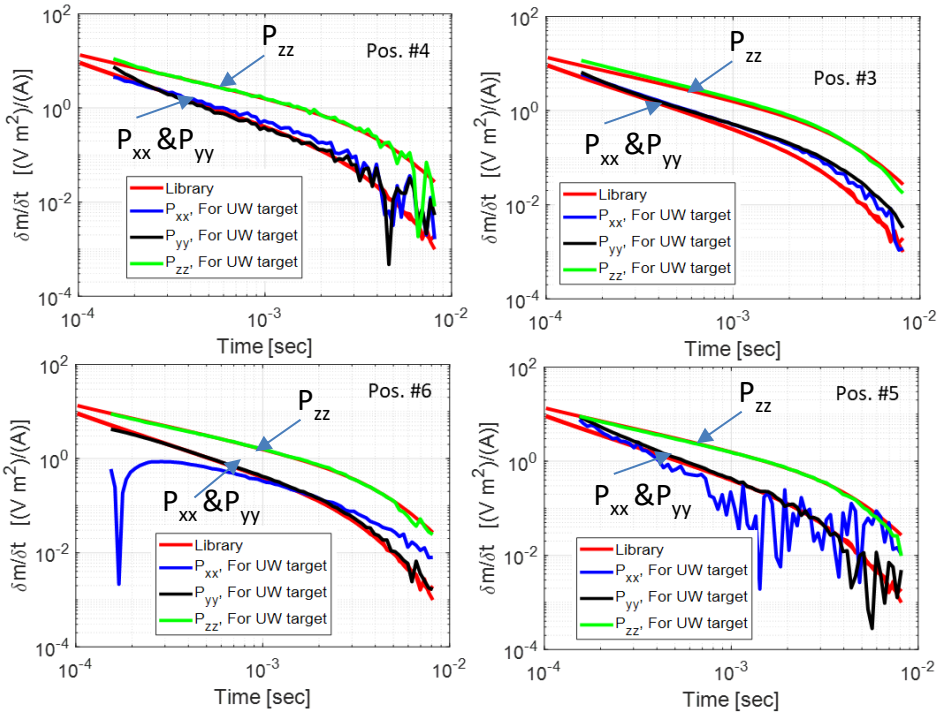

Figure 73. Comparisons between library and extracted effective polarizabilities for an 81 mm projectile placed under positions 3,4,5, and 6 relative to the array in-water measurement.

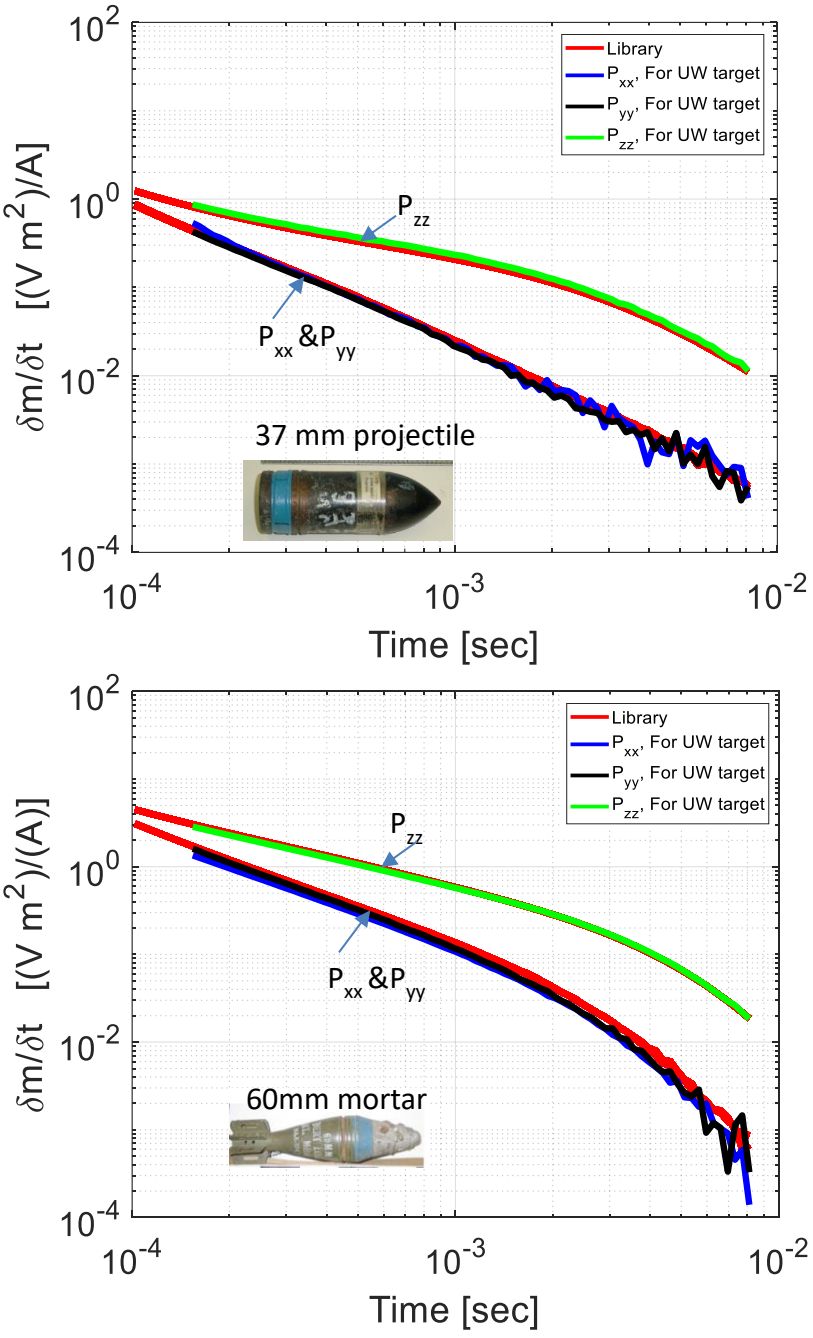

Figure 74. Comparisons between library and extracted effective polarizabilities for a 37 mm projectile and 60mm mortar placed under position 2 relative to the array in-water measurement

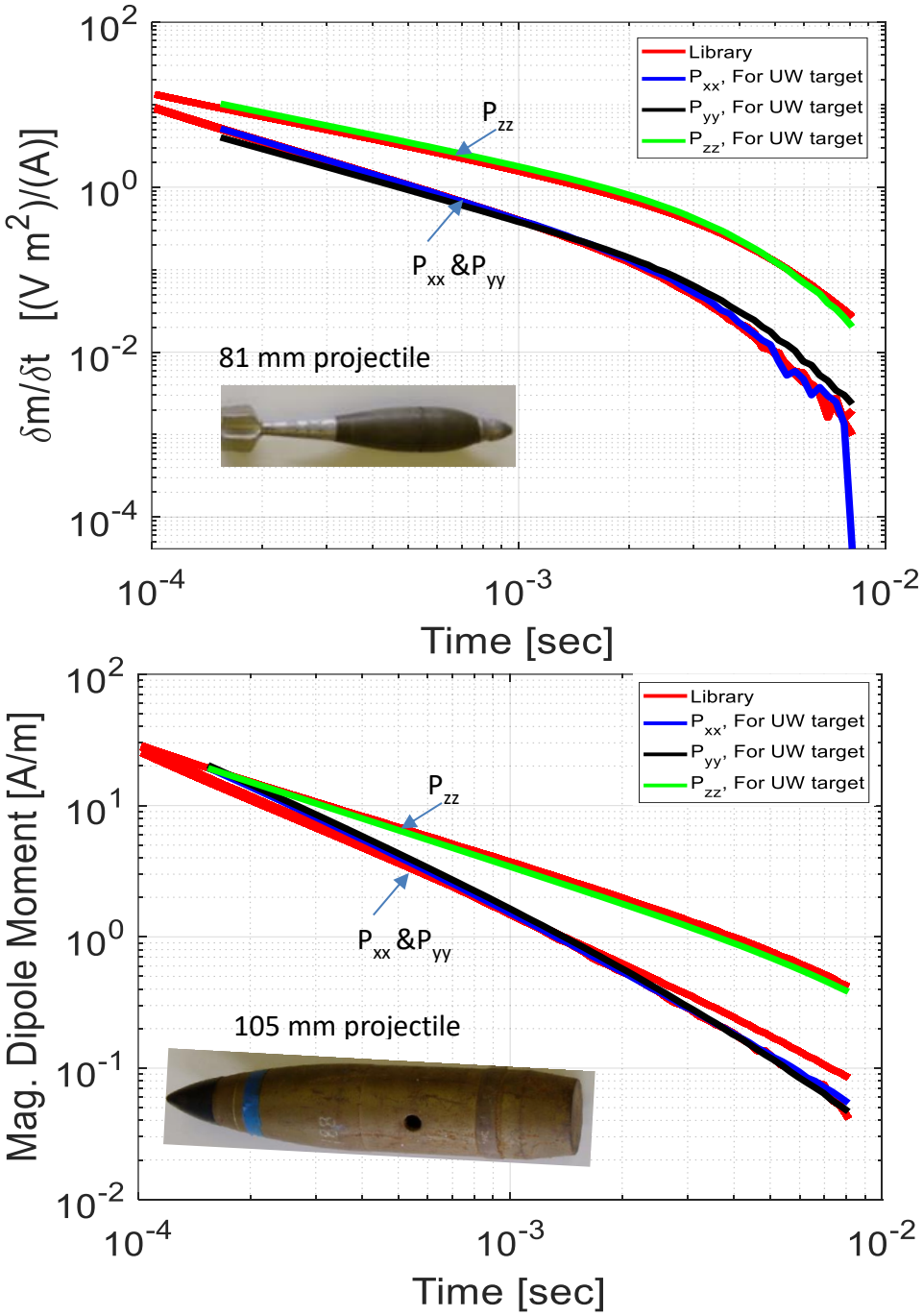

Figure 75. Comparisons between library and extracted effective polarizabilities for an 81 mm and 105 mm projectiles placed under position 2 relative to the array in-water measurement.

The data were inverted using the combined DE and ONVMS model. Due to proximity between Tx array and a target, the voltage produced by the induced magnetic polarizability $\bar{\bar{\mathbf{M}}}_i(t)$, i.e. $\frac{\partial \bar{\bar{\mathbf{G}}}(\mathbf{r},\mathbf{r}',t)}{\partial t} \cdot \mathbf{m}(t)$ term in the eq. 11, was neglected. In the ONVSMS three arbitrarily distributed interacting dipoles were used for predicting targets EMI signals accurately. The source positions were determined using DE. The inverted effective magnetic polarizability tensor principal elements are depicted in Figures 74-75 for small (37 mm projectile), medium (60 mm mortar and 81 mm projectile) and (large 105 mm projectile) size UXO targets. The combined DE-ONVMS algorithm accurately inverts the primary effective polarizability element for all targets from in-water EMI data sets for position # 1 and 2. Although the inverted primary polarization P_{zz} are very robust for each six position, the results show that the inverted secondary and tertiary effective polarizabilities are degraded for targets placed at off center i.e. position #3,4,5 and 6, Figure 73. Thus, the combined DE-ONVMS approach can extract UW targets classification feature parameters accurately, making the method our preferred tool for the UW EMI data processing and targets classification.

7.0 Assessing Advanced EMI models and signal processing algorithms for underwater targets detection and classification

7.1 introduction

This section studies applicability of the advanced EMI models and signal processing approaches for UW targets detection and classification from the UltraTEMA Marine towed system. Namely, detection and classification results are presented for UltraTEMA calibration and blind grid data sets collected at Sequim Bay, WA test site.

Remediation of unexploded ordnance (UXO) contaminated underwater environments at Department of Defense (DoD), USA navy, Marine Corps and Department of Energy (DoE) is expensive and very slow. Recently, the SERDP and ESTCP programs have funded more than fifteen projects to develop and test underwater targets detection and classification sensors and signal processing approaches. Although, most underwater targets sensing technologies such as, magnetometry, side scan sonar and laser line scanners can provide wide-area coverage, they do not provide enough information to identity UW UXO targets from the widespread buried clutter. To overcome this problem and to reduce the cost and accelerate the pace of cleanup, advanced sensing technologies and associated data processing and analysis methods were developed for distinguishing UW buried UXO from the vast quantity of harmless scrap metal found on all munition response sites. Among these systems a UW EMI sensor, called the UltraTEMA-marine towed array, has emerged as one of the potential single-pass marine dynamic classification technologies for wide-area assessment and full coverage surveys.

The single pass UW EMI sensing and targets identification technology has three main stages: detection, inversion, and classification [46]. Detection of UXO can be considered a binary-hypothesis problem in which one must determine whether there are objects present or not. The UltraTEMA system, that consists of four Tx coils and twelve vector receivers, illuminates targets from multiple directions and records targets responses in a vector form, with unprecedented spatial resolution. As a result, the system allows to detect and characterize UW buried objects completely from each dynamic data point.

During the second step of the process, background-corrected data are inverted to extract target parameter information. Both intrinsic target information (classification features) and extrinsic target information (location and orientation) are determined simultaneously. Under this project, our team has adapted and tested a physically complete, fast, accurate, robust, and clutter-tolerant forward model, called the ONVMS method for UW targets detection and classification. The method starts from the assumption that the measurable secondary magnetic field from the target is radiated by a set of elementary dipole sources infused throughout a volume at a set of singular points [47]. The Green's Functions that connects these sources with the measured field are transferred into orthonormal basis functions to streamline the calculations. The spatial distribution of the responding dipoles (their amplitudes scaled by the primary magnetic field) traces a map of "response activity" that reveals the targets below. This ONVMS model [47] is a generalization of the dipole model that simultaneously allows for the presence of several targets in the field of view of the sensor. Additionally, ONVMS supports the possibility that one or more of the targets is of

such complexity—by being large or heterogeneous, for example—that it requires more than one dipole to account for the spatial or temporal nuances of its response. The need to determine the source locations and their intrinsic features results in a computationally costly nonlinear inversion. The inversion defines an objective function that provides a measure of the misfit between predictions and measurements and performs a least-squares minimization. These objective functions tend to have many local minima, resulting in incorrect predictions. There is a procedure that uses elementary sources to locate a singularity directly but its generalization to multi-target scenarios is not straightforward. To avoid this difficulty, our group has employed a two-step inversion approach that combines the ONVMS technique with DE, a continuous genetic algorithm[46], [47]. The procedure alternates between linear ONVMS time-dependent-amplitude determinations and DE location searches, iterating until it reaches convergence.

At the final stage of the process, it is necessary to classify the detected objects as UXO or clutter and, if the former, to determine the type of UXO. This classification step uses data derived from calibration and/or pre-existing library anomalies, associated intrusive ground truth data, and statistical classification tools.

This section describes and quantifies the performance of UW UXO discrimination process that is based on enhanced EMI models, such as orthonormalized volume magnetic source and the differential evolution (DE) approach, which were applied to single-pass marine dynamic data sets called at calibration and blind grids at Sequim Bay, WA test site using the UltraTEMA system.

7.2 Objective of the Demonstrations

The principal objective of this study is to adapt the enhanced UW EMI models and signal processing approaches to the single-pass marine dynamic data sets and demonstrate the capability and reliability of new classification models under real world scenarios. Specific technical objectives were:

- Process single-pass UW EMI datasets collected at calibration and blind grids at Sequim Bay, WA test site using the UltraTEMA system. Establish the limitation and valid range of application of enhanced UW EMI models for targets classification in aquatic environments. Specifically, take into account the number of objects in a close proximity to the sensor, the size and material heterogeneity of those targets, the marine environments EMI responses influencing successful application of the methods, and the performance of the methods based on background noise levels.
- Identify robust classification features which successfully and robustly distinguish UXO targets from non-hazardous objects. Specifically, the technology should:
    a. Identify all seeded and native UXO, and;
    b. Eliminate at least 60% of targets that do not correspond to targets of interest (TOI).
- Document the applicability and limitations of the advanced EMI technologies for processing dynamic data.

Demonstrate a robust target-picking and background-noise-subtraction approach for advanced EMI dynamic data using inverted extrinsic parameters. This entails the extraction of discrimination features like the total ONVMS (i.e., the effective polarizability) and use of a

statistical model-based approach to select robust classification feature vectors for a specific UXO Live Site that can reliably and effectively discriminate hazardous TOI from non-hazardous items.

7.3 Testbed

In 2019, the SERDP/ESTCP MR program established a testbed site at Sequim Bay, WA. The site, that encompasses native UXO free 5-30 m deep water with mixture of muddy and sandy sediments, is designed to evaluate multiple UW sensing technologies for UW UXO targets detection and classification under different environmental setting. The Pacific Northwest National Laboratory (PNNL) runs the site and provides operational, logistical, and facilities support. As a part of this demonstration there were two calibration lanes and the blind-test area. The first calibration lane was set-up for preliminary testing of UltraTEMA sensor.

Table 1. Calibration targets ID and descriptions

Target ID	Description	Placement
I001	8" ISO pipe	x-orientation (East-West)
I002	8" ISO pipe	y-orientation (North-South)
I003	8" ISO pipe	z-orientation (Vertical)
I004	8" ISO pipe	x-orientation (East-West)
I005	8" ISO pipe	y-orientation (North-South)
I006	8" ISO pipe	z-orientation (Vertical)
I007	12" ISO pipe	x-orientation (East-West)
I008	12" ISO pipe	y-orientation (North-South)
I009	12" ISO pipe	z-orientation (Vertical)
I010	12" ISO pipe	x-orientation (East-West)
I011	12" ISO pipe	y-orientation (North-South)
I012	12" ISO pipe	z-orientation (Vertical)
C004	Anchor	On seabed
C006	Scuba Tank	On seabed
C007	Cement Block	On seabed
R001	Howitzer Replica	Buried
R003	Howitzer Replica	On seabed
U002	155 mm Howitzer	On seabed
U008	105 mm M60	Buried
U012	155 mm Howitzer	Buried
U018	105 mm Heat	On seabed
U204	105 mm M60	On seabed
U206	105 mm Heat	Buried
U213	81 mm M821	On seabed
U226	81 mm M889A	On seabed
U229	60 mm M49	On seabed
U230	40 mm L70	On seabed

The lane was 85m long and had six medium and six large ISOs 2m to the left or right of the centerline with two of each item oriented along-track, two across-track and two vertically, see Table 1. The second calibration lane, parallel to the first calibration lane, was set-up for assessing both the UltraTEMA and MuST systems, Figure 76. This lane comprised a number of different UXO surrogates (60 and 81mm mortars, 40-, 105- and 155-mm projectiles) and clutter items (scuba tank, anchor and cement block), Table 1. The second calibration lane, parallel to the first calibration lane, was set-up for assessing both the UltraTEMA and MuST systems, Figure 76. This lane comprised a number of different UXO surrogates (60 and 81mm mortars, 40-, 105- and 155-mm projectiles) and clutter items (scuba tank, anchor and cement block), Table 1.

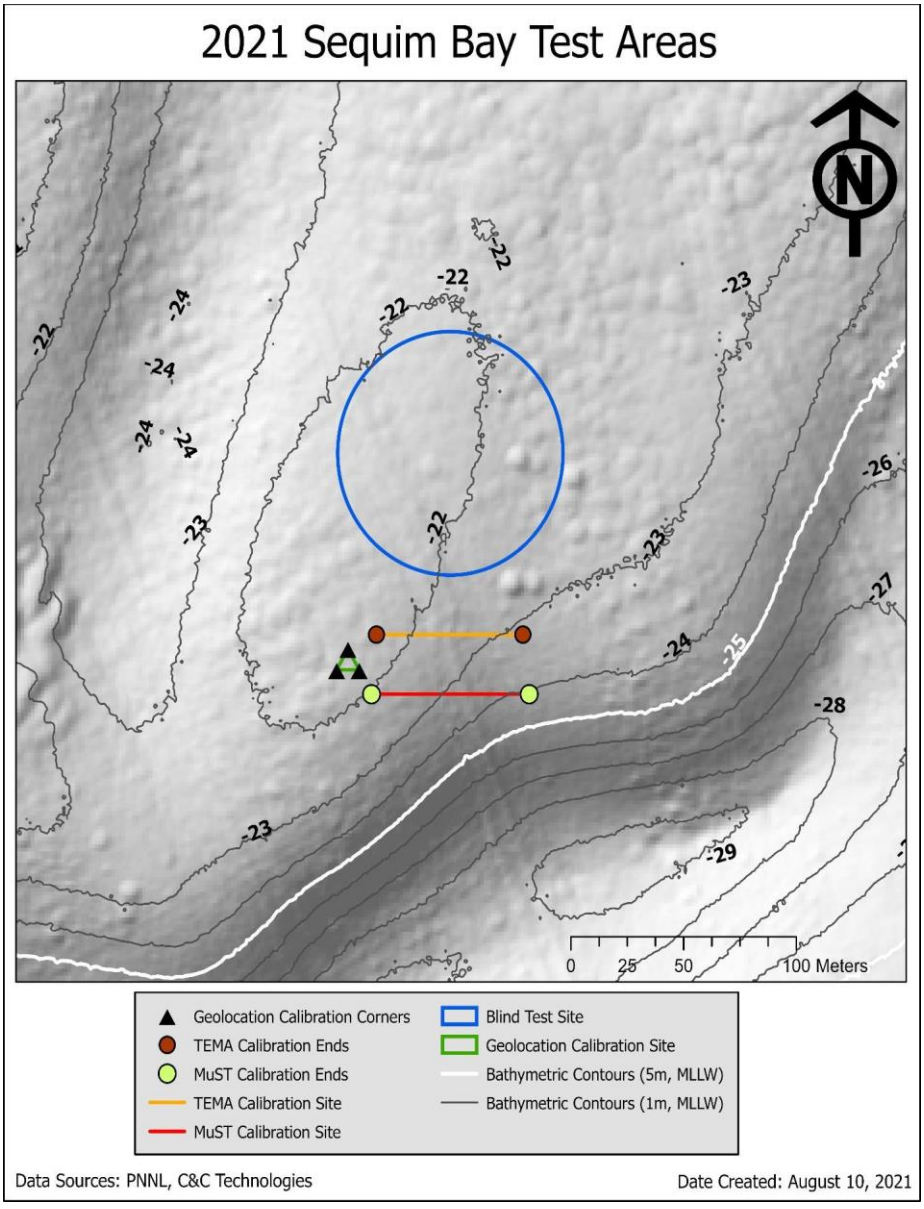

Figure 76. Sequim Bay calibration and blind grids test areas.

7.4 Modeling UltraTEMA System

The Sequim Bay calibration and blind grid data sets were collected using the UtlraTEMA system. The UltraTEMA system consists of four transmitter coils and twelve vector receiver sensors Figure **77**. Thus, the system measures complete EMI response of a target at each dynamic data point and provides 144 data value at each nth (n=1,2, .., 25) time gate.

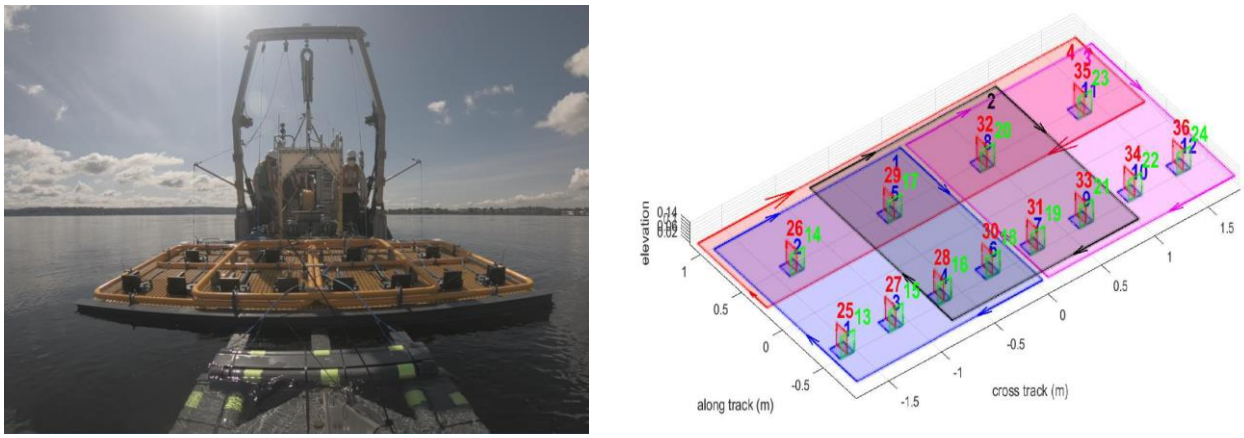

Figure 77. **Left:** Actual UltraTEMA and (**Right:)** its schematic diagram.

The UltrTEMA transmitters are modeled as infinitesimally thin wires. The complete primary field produced at any observation point **r** by the *T*th loop is determined from the Biot-Savart law,

$$\mathbf{B}_T(\mathbf{r}) = \frac{\mu_0}{4\pi}\sum_{i=1}^{N_{Tx}} \frac{I_T[\Delta\ell_{T,i}\times\mathbf{R}_{T,i}]}{R_{T,i}^3}, \quad T=1,2,3,4., \tag{57}$$

where, for the *T*th transmitter loop, $\mathbf{R}_{T,i} = |\mathbf{r}-\mathbf{r}'_{T,i}|$, $\mathbf{r}_{T,i}$ $\mathbf{r}'_{j,i}$ is the location of the *T*-th current element, and $\Delta\ell_{T,i}$ is the tangential length vector for the *i*-th subsection of the loop. In all subsequent analysis, unless otherwise noted, each transmitter coil (*T* = 1,2,3,4) was divided into $N_{\text{Tx}} = 40$ subsections and the primary magnetic field $\mathbf{B}_T(\mathbf{r})$ was calculated using equation (57).

Each of UltraTEMA twelve cube Rx measures the induced voltage along three orthogonal directions. The induced voltage is the negative of the time derivative of the secondary magnetic flux through each coil. The induced voltage on the *R*th cube (*R* = 1,2,3,4) along the αth direction (α = *z*,*y*,*x*) is calculated as

$$V_R^{\alpha} = -\int_{S_R^{\alpha}} \frac{\partial \mathbf{B}}{\partial t}\cdot d\mathbf{s}_R^{\alpha} = \sum_{i=1}^{N_{Rx}} \frac{\partial \mathbf{B}_i(\mathbf{r}_{i,R}-\mathbf{r})}{\partial t}\cdot\hat{\mathbf{n}}_{\alpha}\Delta s_{i,R}^{\alpha} \tag{58}$$

where s_R^α is the area of the receiver in the α th direction of the *R*th Rx cube (which is 15 × 15 cm^2), $\Delta s_{i,R}^\alpha$ and $\mathbf{r}_{i,R}$ are respectively the *i*th sub-area and observation point on the surface s_R^α, and $\hat{\mathbf{n}}_\alpha$ is normal to s_R^α. $\mathbf{B}(\mathbf{r}_{i,R}^\alpha) = \mu_o \mathbf{H}(\mathbf{r}_{i,R}^\alpha)$ is the magnetic field produced by a magnetic dipole/charge source placed at point **r**;

7.5 UltraTEMA Data Pre-processing and Background Correction

We received calibration and blind UltraTEMA sets in ascii format from the SERDP office. The EMI data were co-registered with the sensor's underwater Global Positioning System (GPS) and an inertial measurement unit (IMU) data set. In addition, the EMI data were normalized to the corresponding transmitter currents maximum $\max(I_T)$ as

$$D_T^i(t_q) = S_{T,i}(t_q) \Big/ \max(I_T) \tag{59}$$

The background signals are removed for each time t_q, $q = 1,2,...,25$ channel using detrending algorithm with 10 m window length line-by-line.

7.1 Targets detection

We used two: (1) the traditional amplitude response matric approach – using measured signals peak values above the 4 mV/A threshold; and (2) using an advanced anomaly selection procedure exploiting the locations of all responding ONVMS for each point of the dynamic data.

Comparisons between predicted target locations, estimated using traditional and advanced target picking algorithms, and actual targets locations measured intrusively by provided by the PNNL at the calibration area are showed in Figure 78 and Figure **79**. The comparisons show that the advanced anomaly selection approach maps the subsurface targets accurately and provide significantly improved anomaly locations compared to the traditional amplitude thresholding approach, particularly for small targets i.e for small SNR, see Figure **79**. In addition the results show that the traditional detection threshold based approach missed targets #U229 (60 mm mortar) and #U230 (40 mm projectile), where else the advanced targets detection algorithm detect and locate both anomalies, see Figure 79 and Figure 80. And as expected both approaches did not detect a cement block.

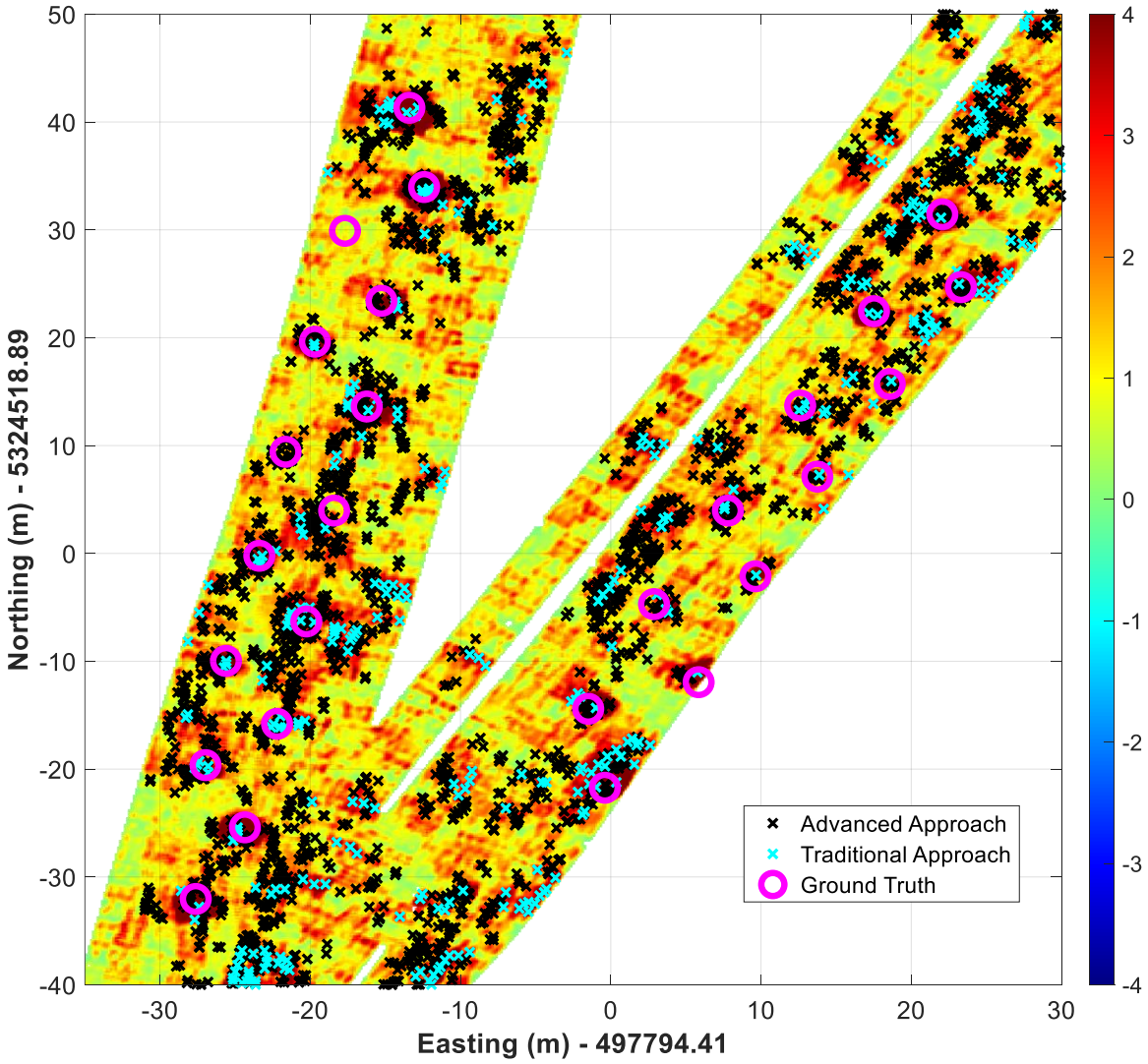

Figure 78. Color map: Mapped response amplitude [uV/A]; Locations of detected targets using the traditional response metric (cyan crosses) and advanced anomaly (using all inverted locations) section approach (Black crosses), respectively. Magenta circles: Ground truth of targets locations.

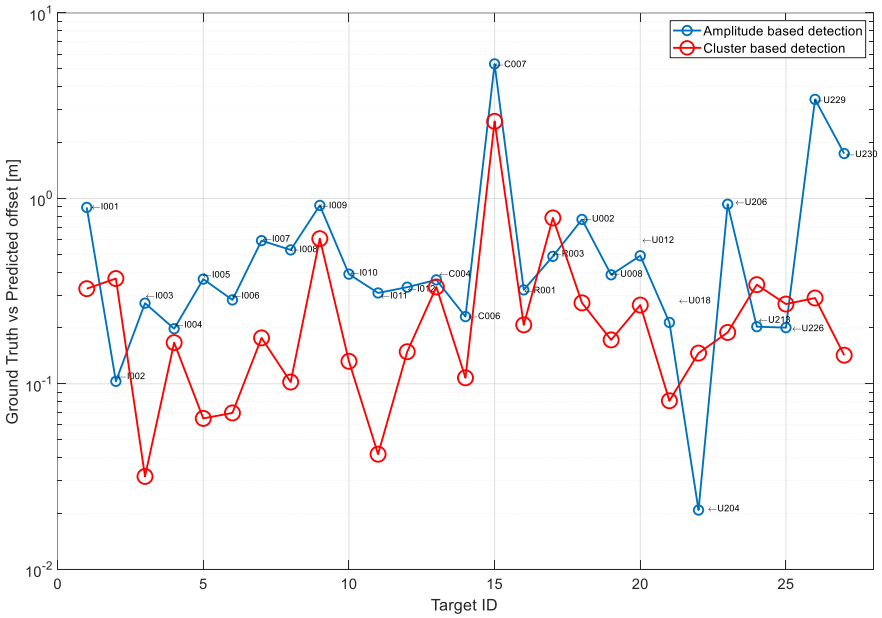

Figure 79. Difference between the predicted and actual locations for Calibration targets.

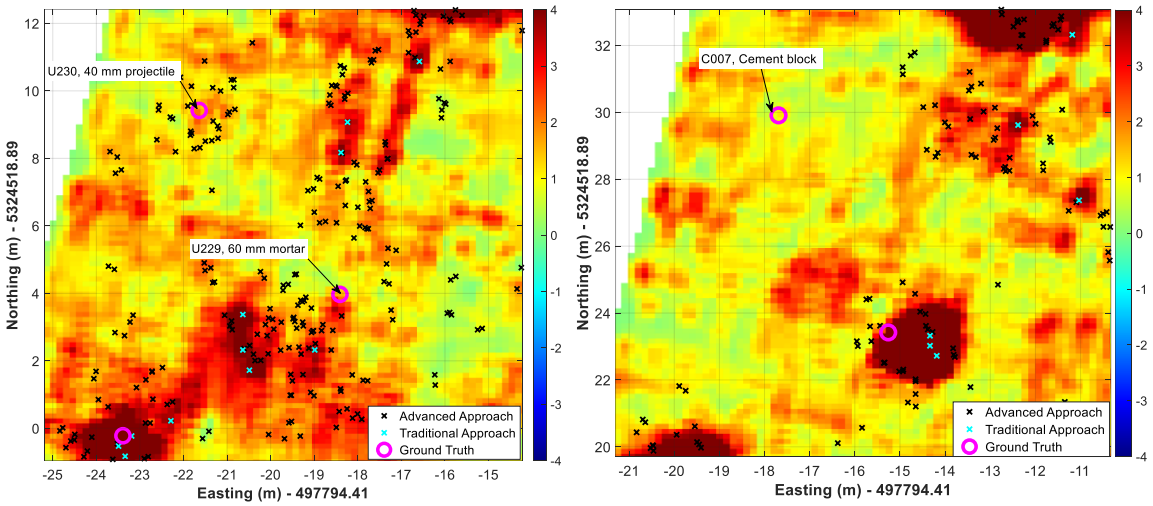

Figure 80. **Right:** Amplitude (uV/A) based detection map near targets U229 and U230(40 mm projectile). **Left:** Amplitude (uV/A) based detection map near targets C007 (cement block). Locations of detected targets using the traditional response metric (cyan crosses) and advanced anomaly (using all inverted locations) section approach (Black crosses), respectively. Magenta circles: Ground truth of targets locations.

7.2 Extracting targets classification features

The enhanced EMI models and data processing algorithms extract the intrinsic parameters of UW targets for each dynamic data point. These extracted features, i.e. the effective magnetic dipole polarizabilities, allow us to classify targets as TOI and no-TOI with high confidence. To demonstrate applicability of the enchanted models for UW targets classification, UW UltraTEMA dynamic calibration data set was inverted, and targets figure parameters were extracted and analyzed classification point of view. Figures 81-85 show the effective primary (green lines), secondary (black lines) and tertiary (blue lines) for UW scuba tanke, 8" and 12" ISO pipes, 105 mm HEAT, 105 mm, 155 mm and 40 mm projectiles, and 81 mm and 60 mm mortars. The extracted effective polarizabilities are compared to the corresponding library targets polarizabilities. The results show that the effective polarizabilities are stable and in good correlation with the library polarizabilities. Thus our UW dynamic EMI data processing and classification algorithms are able to completely characterize and classify anomalies.

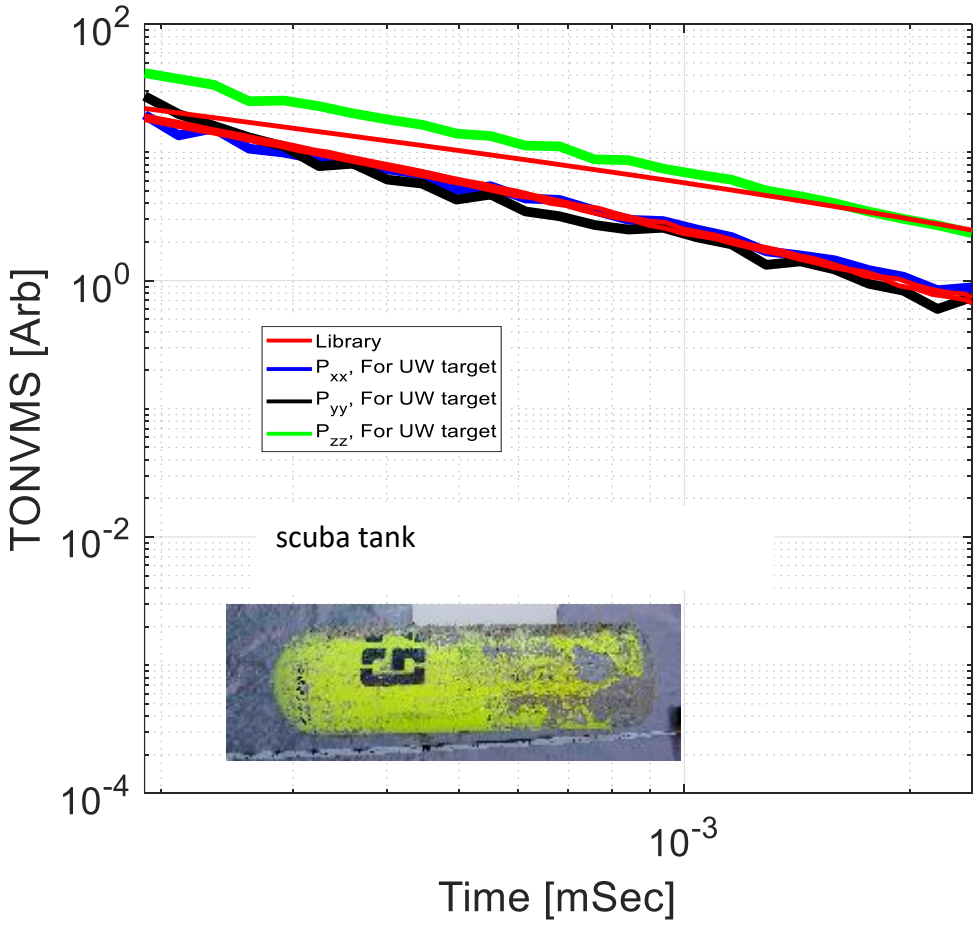

Figure 81. Comparisons between a 105mm projectile library and extracted effective polarizabilities from dynamic UW UltraTEMA data set for a calibration scuba tank target.

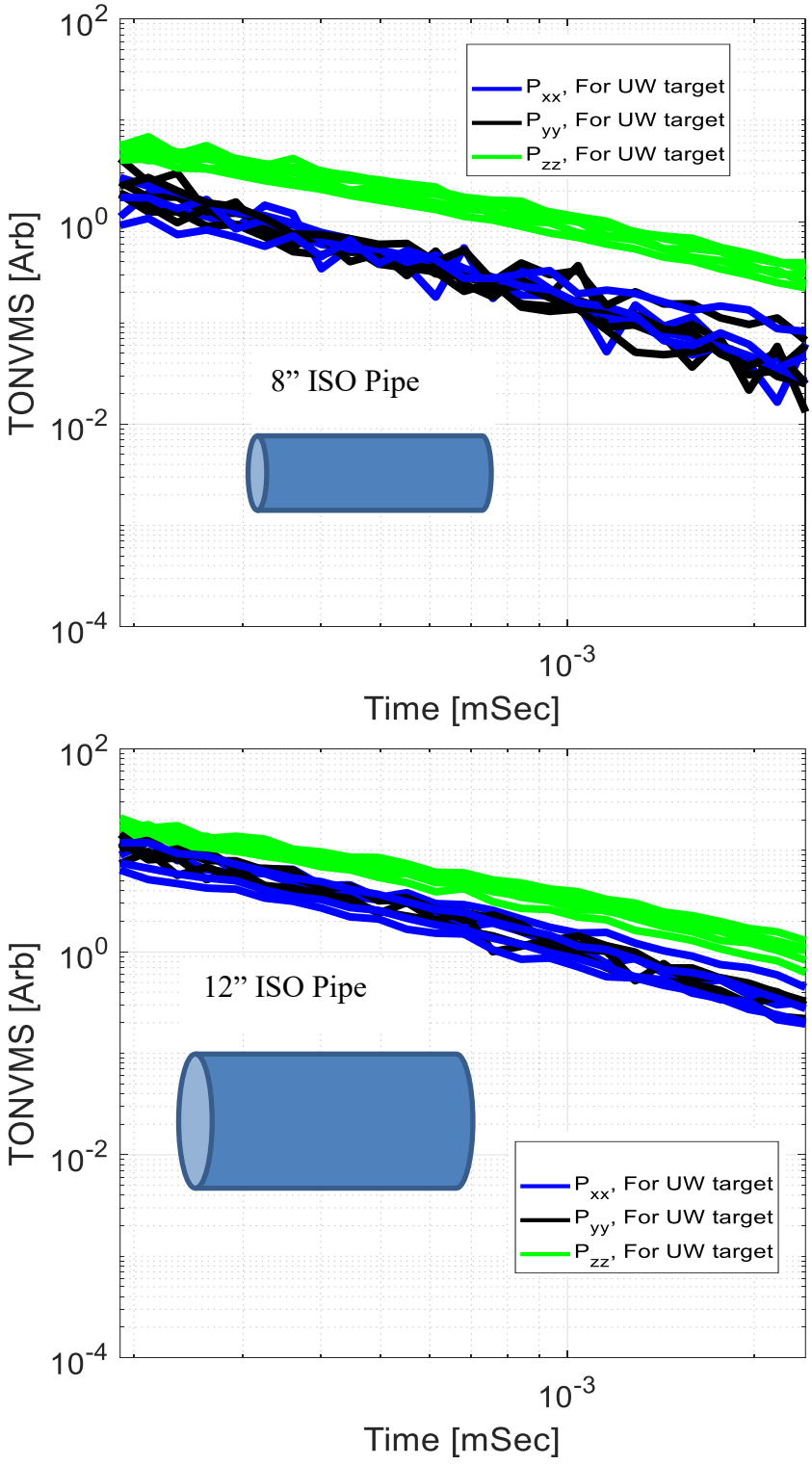

Figure 82. Extracted effective polarizabilities from dynamic UW UltraTEMA data set for 8" (**top**) and 12" (**bottom**) ISO pipes placed in the calibration area.

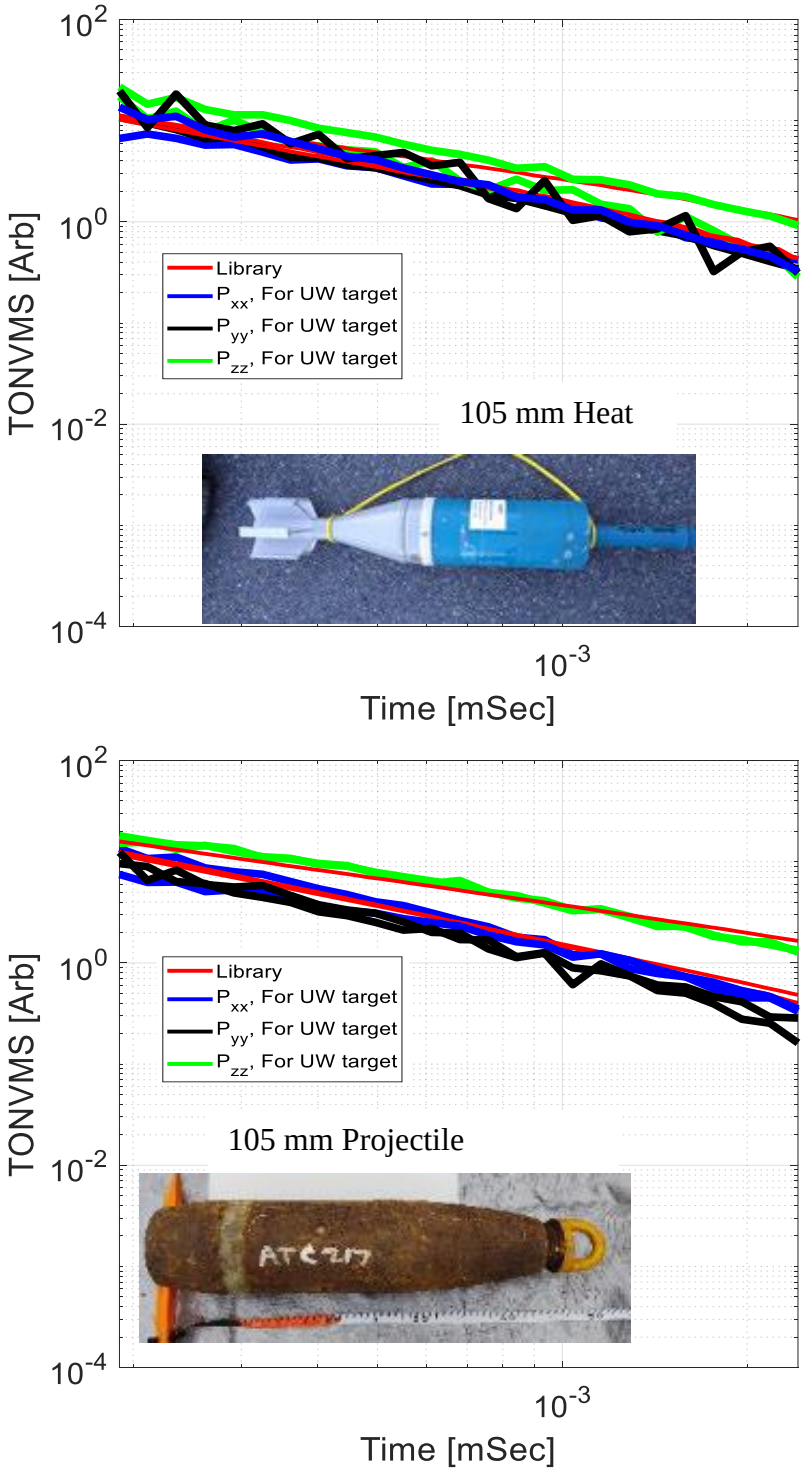

Figure 83. Comparisons between library and extracted effective for calibration UW 105 mm HEAT (**top**) and 105mm projectiles (**bottom**).

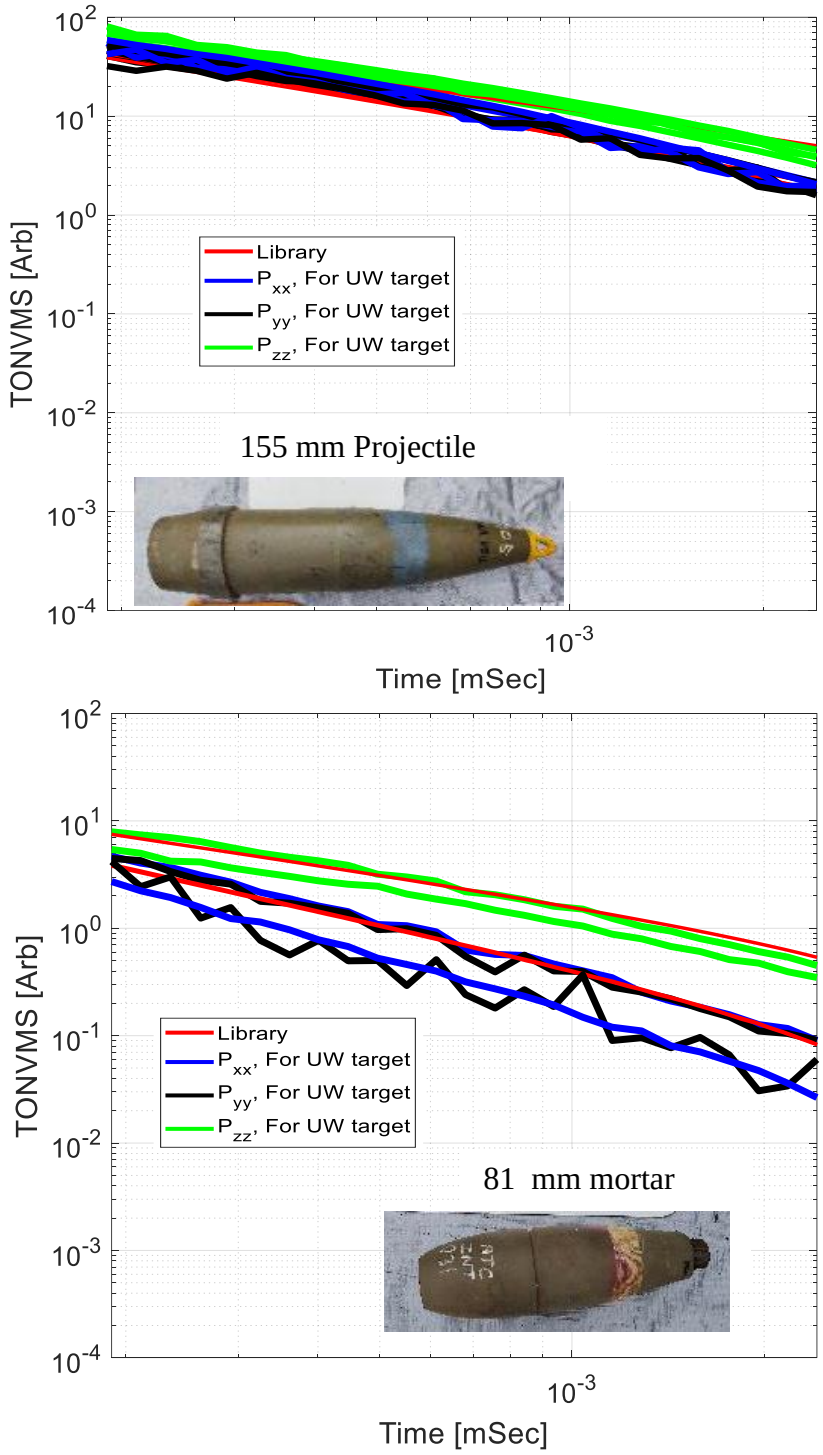

Figure 84. Comparisons between library and extracted effective polarizabilities for calibration UW 155 mm projectiles (**top**) and 81 mm mortars (**bottom**).

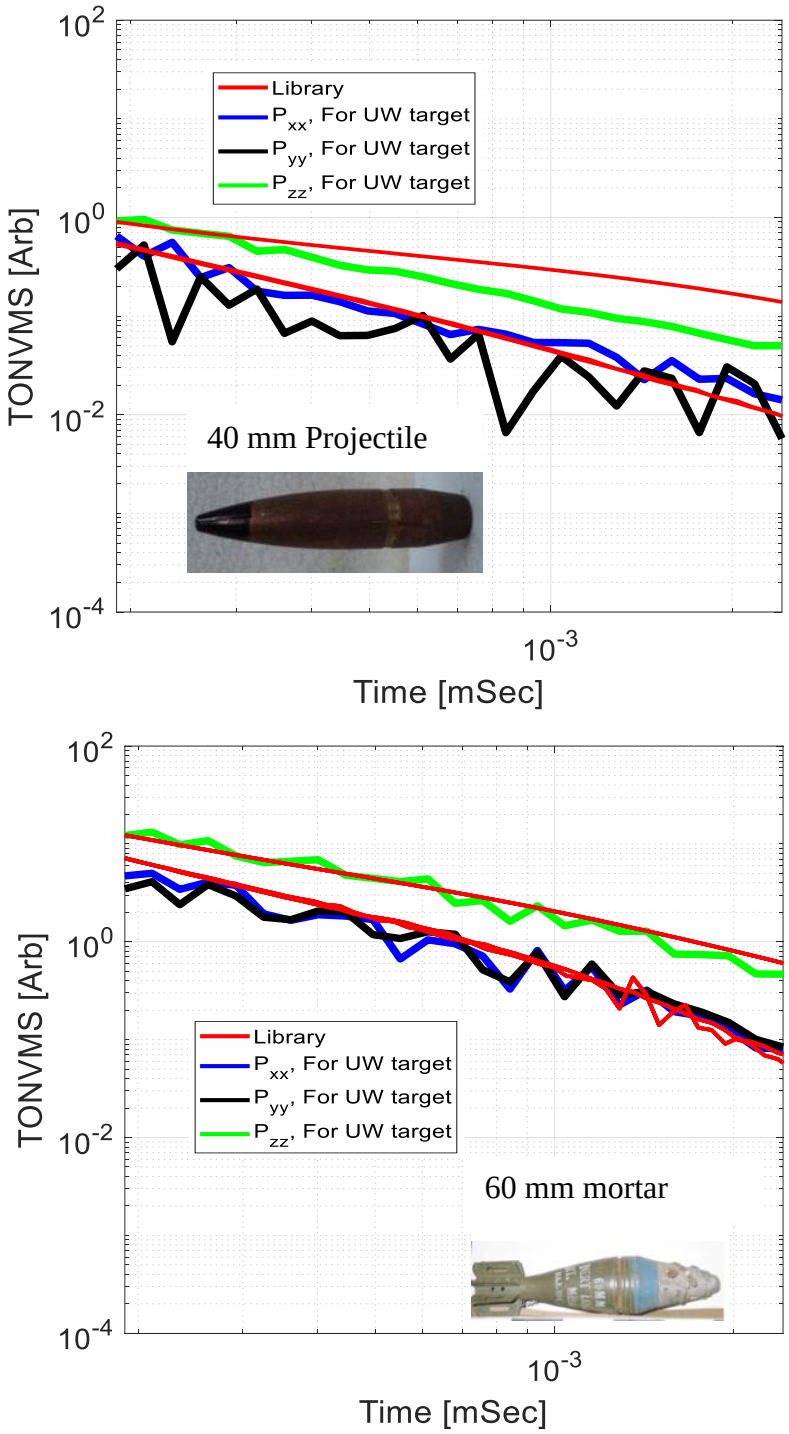

Figure 85. Comparisons between library and extracted effective polarizabilities for calibration UW a 40 mm (**top**) projectile and 60 mm mortar (**bottom**).

7.3 Blind Grid inversion and classification studies

One of the main goals of the enhanced forward and inverse EMI models is to map, locate and identify all TOI in a complex UW environment. At the end of the project, we have received UW UltraTEMA data sets collected at Sequim Bay blind grid area, see Figure 76. The targets detection map is depicted in Figure 86. During this study, first background responses were removed, then targets were detected using the field-based threshold approach, third all dynamic data points within 3 meter radius around the each detected anomaly were processed using the combined enhanced EMI models– DE using a multiple source inversion approach, and the intrinsic (such as effective dipole moment i.e total ONVMS) and extrinsic (targets location) parameters of the targets were extracted, clustered and used for classification.

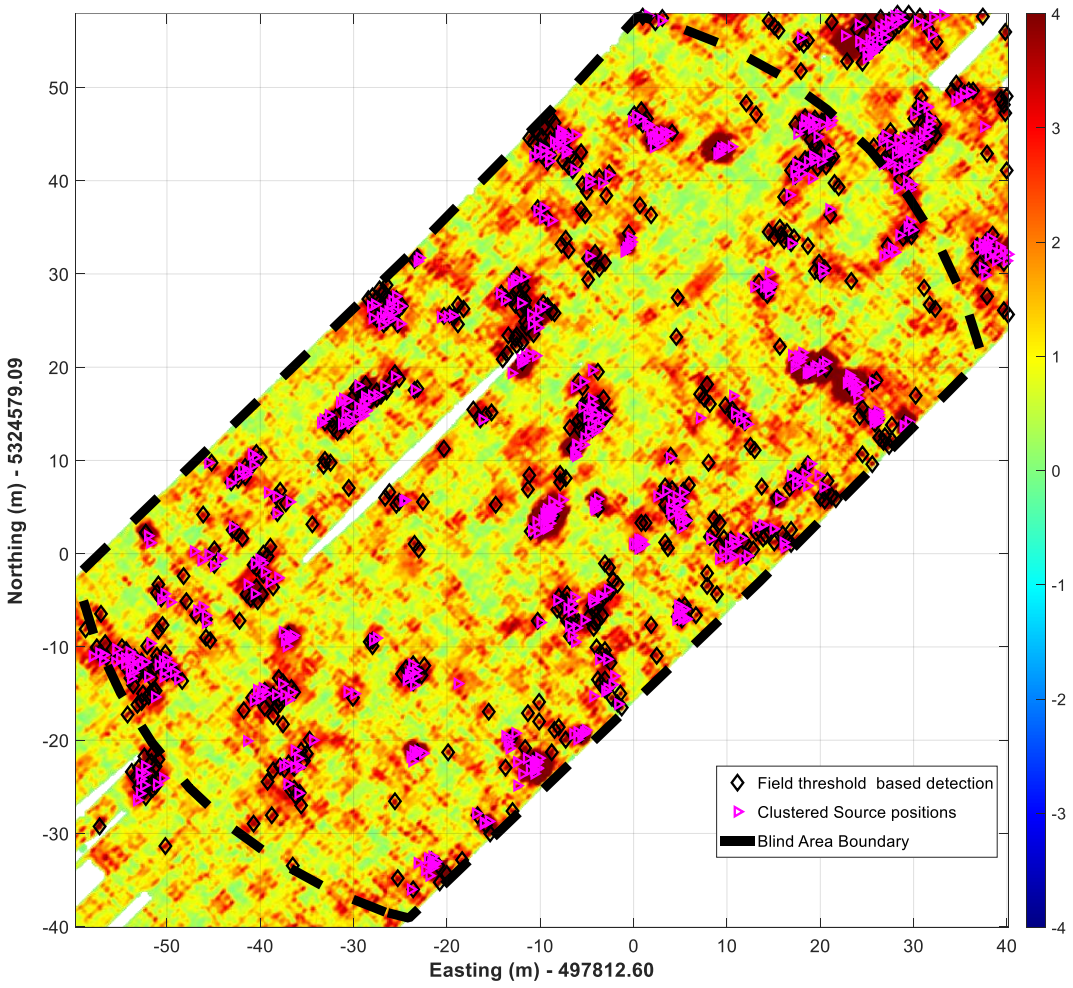

Figure 86. Blind grid detection map. Color map: Mapped response amplitude [uV/A]; Locations of detected targets using the traditional response metric (black diamonds) and clustered and clustered and filtered inverted source locations (using inverted locations around each detected anomaly magenta triangles), respectively

Suspected TOI-s were:

- 155 mm Howitzer
- 105 mm projectiles
- 81 mm projectiles
- 60 mm mortars

The final prioritized dig list was created and submitted to the IDA for scoring. The independent scored result in the form of a ROC curve is depicted in Figure 87. The

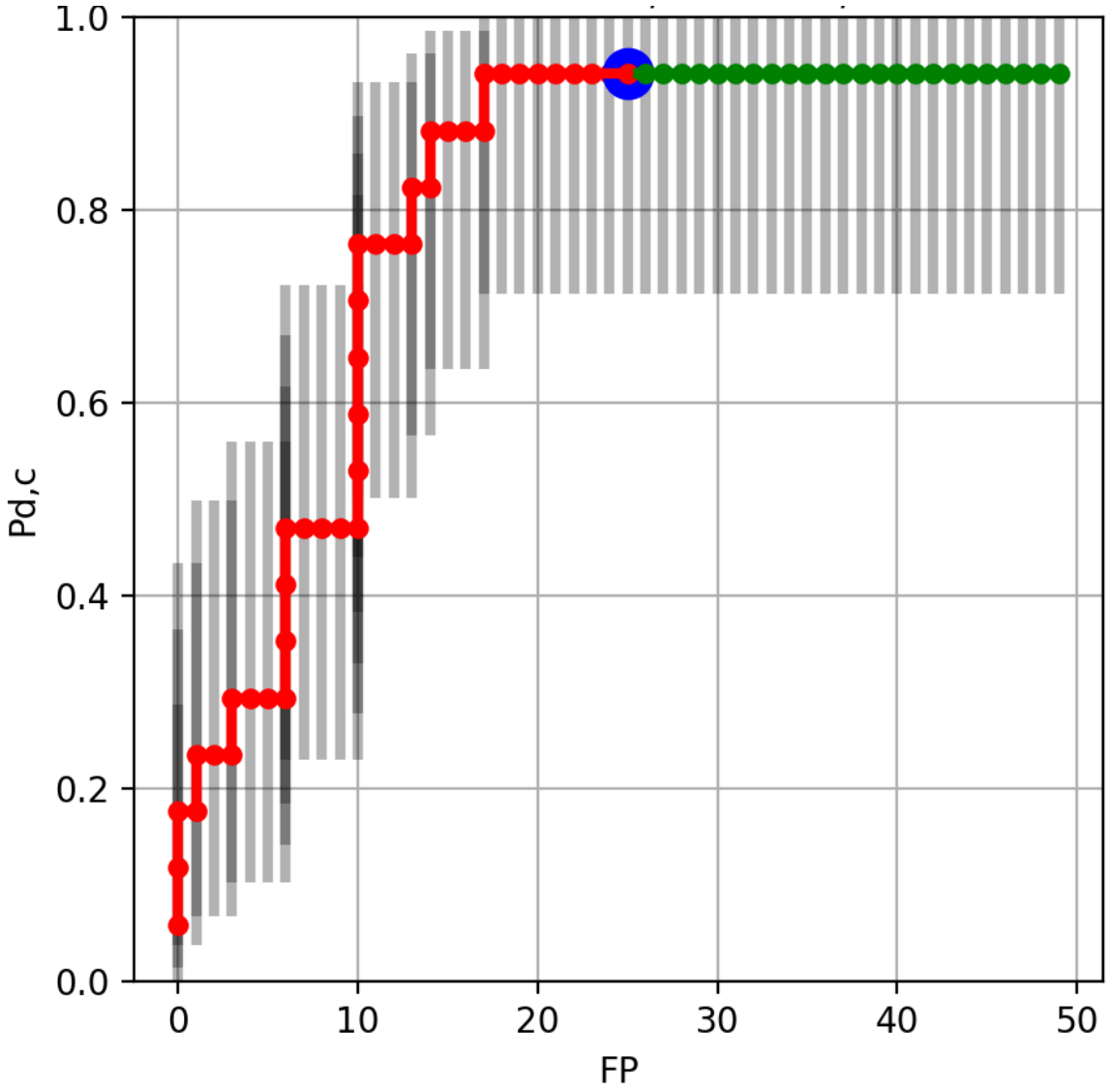

Figure 87. ROC result for the 2021 Sequim Bay Blind Test UltraTEMA data using enhanced EMI models.

The independently scored result shows that of the sixteen TOIs out of seventeen were ranked correctly as “Dig” before the dig-stop point, along with additional twenty-five false positive targets. There was one false negative, the processed missed one out of two 60 mm mortar.

To understand the cause of missing one TOI, we conducted RCA after receiving the ROC and approximate location of the missed anomaly. The Figure 88 illustrates location of the missed anomaly on the detection map. The result shows that the field threshold detection algorithm did not detect the anomaly, and therefore none of dynamic data points were inverted and analyzed near the missed anomaly.

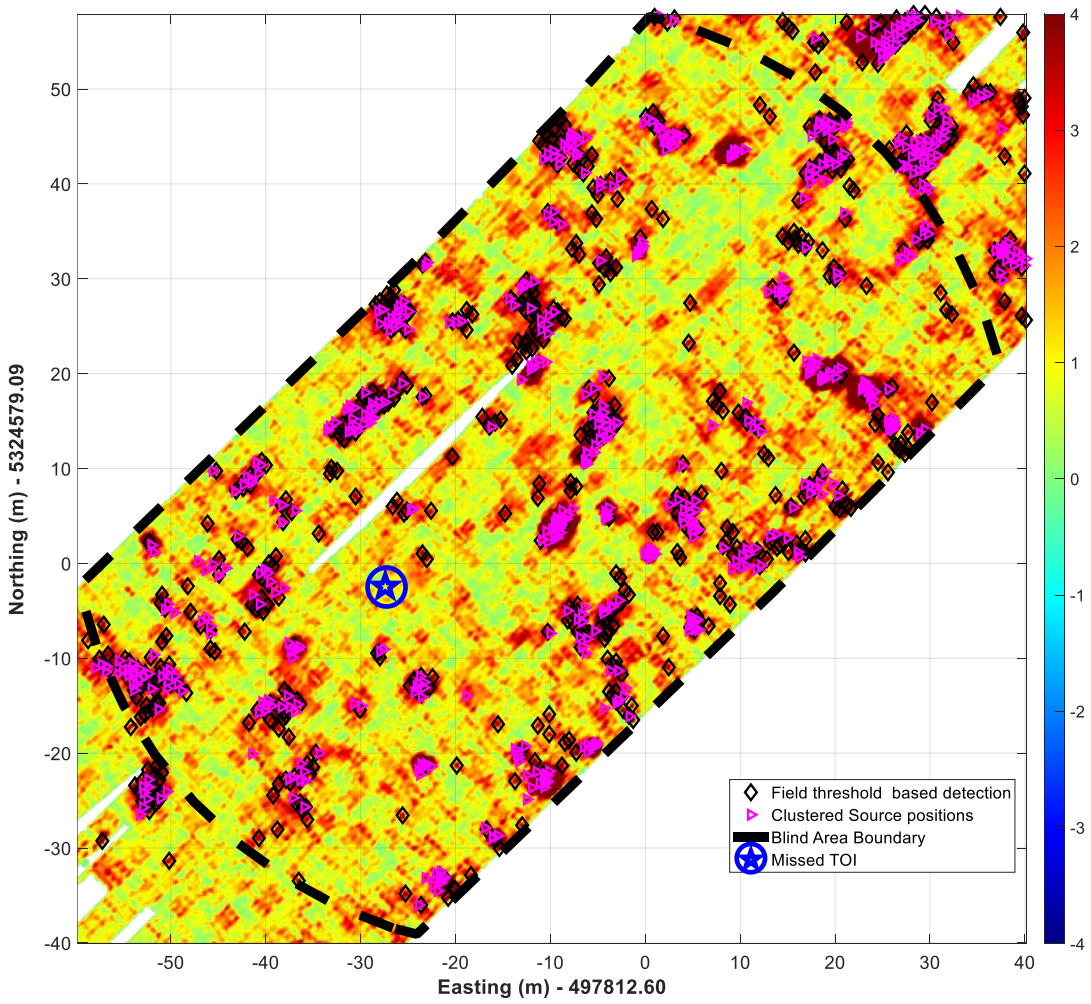

Figure 88. Blind grid detection map with missed TOI location.

To assess applicability the enhanced EMI models underwater targets classification capabilities, we extracted, inverted and analyzed dynamic data points around the missed anomaly. The extracted clustered locations are depicted on Figure 89. The analyses show that there are several clusters centroid locations within 2-meter radius for the missed 60 mm mortar location.

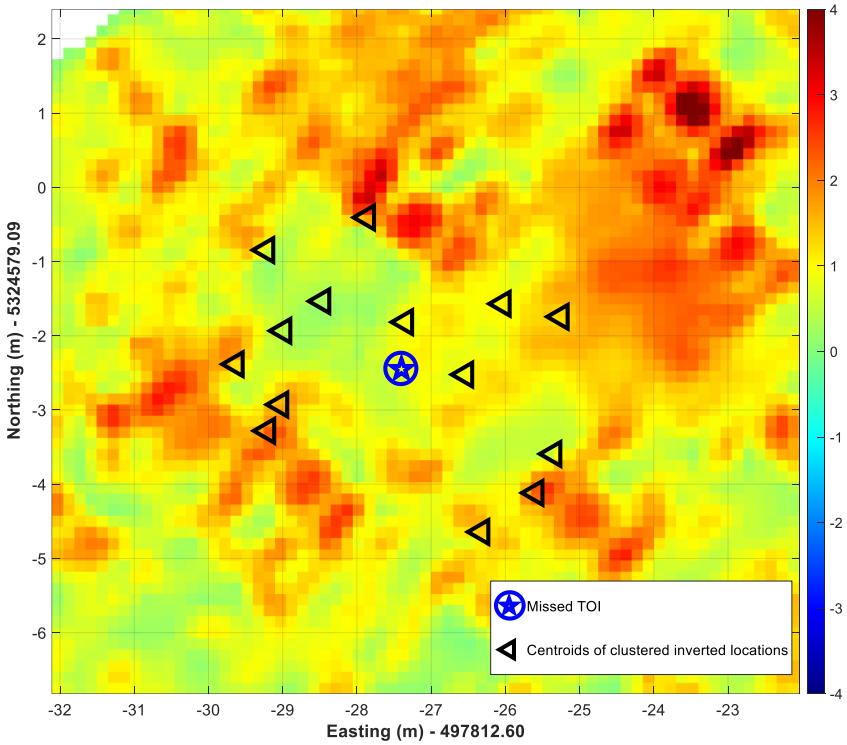

Figure 89. Centroids of clustered inverted locations around the missed UW 60 mm mortar on detection map.

Finally, we analyzed the extracted effective polarizabilities for each cluster around the missed TOI. A good correlations between extracted and library polarizabilities is showed on Figure 90.

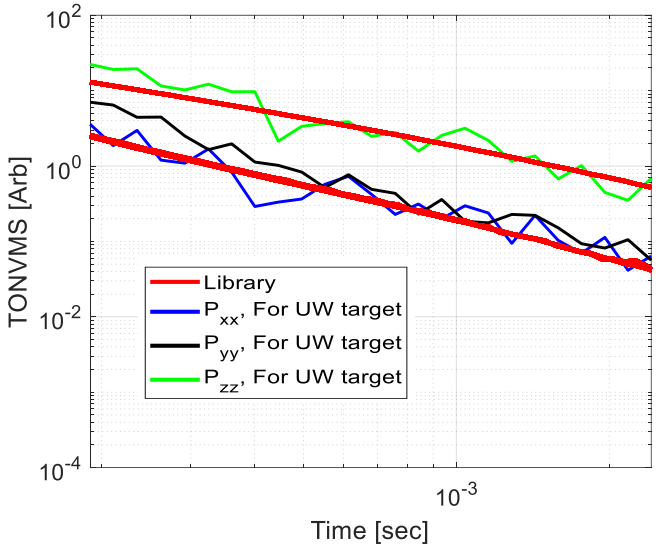

Figure 90. Comparisons between library and extracted effective polarizabilities for the missed 60 mm mortar.

8.0 Conclusions

In this final report:

1. low frequency EMI signals diffusions are studied in three-layer air-water-sediment structures with and without highly permeable and conducting targets in both frequency and time domain. Frequency domain calculations are done using the method of auxiliary sources together with the cylindrical plane wave expansion technique. The frequency domain signals are translated into the time domain using Fourier cosine/sine transforms and Anderson filters. The studies show that water-air and water-sediment boundaries produce nonnegligible EMI responses, which vary with respect to the transmitter loop size, sediment conductivity and magnetic susceptibility, as well as the distances between the loop and water-air and water-sediment boundaries. The comparisons between reflected signals and the response from a conducting, permeable and non-permeable sphere illustrate that the background signals (=total response from layer boundaries) are higher than the response from the sphere/105mm-projectile at early times. A new scheme is proposed for extracting a target's true EMI responses.

2. Transient EMI problems are solved directly in time domain using the unconditionally stable Crank-Nicolson FDTD method. The stability of the CN-FDTD scheme is derived and showed that the method is unconditionally stable not only for large time steps but also for non-uniform time steps. The studies are done for a uniform conducting space and for three-layer air-water-sediment structures with and without a conducting, permeable and non-permeable cylinder embedded in conducting sediment. The studies show that uniform conducting as well as three-layer air-water-sediment produce EMI responses, which vary with respect to conductivity and with the distances between the target and observation point. The comparisons between background signals and the response from a conducting, permeable and non-permeable cylinder illustrate that the background signals are higher than the response form the cylinder at early times. These high background signals move to later time channels as the distance between the target and observation points increases. The secondary signals associated with a target must be extracted from a complete signal that also contains the response of the mass of salt water as background.

3. The modeled results were validated against actual data for an advanced EMI system placed in marine environments. The comparisons showed good agreement between modeled and measured data for UltraTEM system placed in 2.5 m and 5.8 m water depth marine environments. In addition, the numerical results demonstrated that: a. direct signals (i.e. response from surrounding medium) from transmitter to the Rx coils after Tx currents are turned-off is about 12 times higher than signals from layer boundaries, i.e. the primary magnetic fields do not decay rapidly due to eddy currents in the surrounding conducting medium; b) the primary magnetic fields vertical (z) and horizontal (x, y) components decay as $t^{-3/2}$ and $t^{-5/2}$ after the horizontal Tx loop's current is turned-off; c) the induced electric field (eddy currents form) slowing moving "smoke rings". The magnitudes of the eddy currents, distributed along depth, converge to a constant value, whereas the magnitudes of

the eddy currents, distributed along lateral directions, increases as the lateral distance for the Tx center increases.

4. Enhanced EMI models are developed to accurately account for transient responses from: UW targets, layer boundaries and transmitters/receivers surrounding medium. The enhanced approach, that combines the transient magnetic dipole's model and time domain image technique, is a fast and physically complete model. The measured voltage due to enhanced transient magnetic dipole in conducting media is a sum of voltage produced by the time derivative of the magnetic dipole moment (same as for the land-based EMI problem) and the magnetic dipole moment itself (a new term). The enhanced models were validated against analytical and experimental data sets. The results showed that voltage due to the magnetic dipole moment (the new term) is about 100 times higher than signals produced by the time derivative of the magnetic dipole moment at the very early times (between 10 and 100 us).

5. The advanced EMI data inversion approach, that combines enhanced models, ONVMS and DE algorithms, are adapted to UW EMI data sets. The inversion model was applied UW data set collected at Duck, NC test site. The targets classification feature parameters were extracted and compare to the DoD library targets parameters. Excellent agreements were demonstrated between the inverted and DoD targets' effective polarizabilities.

6. The enhanced EMI data inversion and signal processing approaches are applied to dynamic UW UltraTEMA data sets. Each dynamic point data were processed, targets' classification feature parameters were extracted, and targets identified using a fingerprinting matching technique. The results illustrated that our UW dynamic EMI data processing and classification algorithms can completely characterize and classify both UW surface (unearthed) and buried UXO targets.

7. The blind test area classification studies have revealed that:
    a. although the inverted locations are clustered tightly, the geolocation errors between ground truth and the inverted locations are within couple of meters. These large geolocations errors could be related to sensors geolocations; GPS antenna position; rotation angles convention, and the transferring inverted locations from local to global coordinate system. Additional studies should be conducted to identity and mitigate the main geolocation error attribute.
    b. the enchanted EMI models were able to locate and classify corrected all but one small 60 mm mortar (1 False negative) with 25 false positives in the UltraTEMA test area.
    c. extracted effective polarizabilities (TONVMS) are noisy from time-channel to time-channel. This noise maybe related to sensor UW motion and/or wiring. The cause of the noise needs to be investigated.

8. The route cause analyses for the missed one of the two 60mm mortars illustrated that all dynamic data points should be inverted using a multi-source inversion approach. The extracted locations and effective polarizabilities should be used to detect and classify, respectively, all UW targets.

9.0 Project-Related Publications

[1] Fridon Shubitidze, Kevin O'Neill, Benjamin E. Barrowes, Dartmouth College (USA); John B. Sigman, "Accounting for the influence of salt water in the physics required for processing underwater UXO EMI signals", *Proceedings of SPIE 2018*

[2] F. Shubitidze, *and et al. "*Modeling Targets EMI Responses in an Underwater Environment*", SAGEEP-2018*

[3] Fridon Shubitidze, Benjamin E. Barrowes, O'Neill, "Investigating time domain EMI signals diffusion in a conducting environment for UXO detection and classification", *SPIE* Defense + Commercial Sensing, *Baltimore.* April 14-April 18, 2019.

[4] Kevin O'Neill, Fridon Shubitidze and Benjamin E. Barrowes, "Analysis of the effect of salt water on time domain electromagnetic induction sensing of submerged metallic objects", *SPIE* Defense + Commercial Sensing, *Baltimore.* April 14-April 18, 2019.

[5] Fridon Shubitidze, Benjamin Barrowes, K.O'Neill, "Advanced Forward and Inverse Models Applied to Underwater EMI Data Sets", SERDP-ESTCP Symposium, 2018, November 27-29, 2018.

[6] Tornike Shubitidze ; Benjamin E. Barrowes ; Evan Chapman ; Mikheil Prishvin ; Kevin O'Neill ; Fridon Shubitidze , The Crank-Nicolson FDTD Method is Cylindrical Coordinates and Its Application to Underwater UXO detection and Classification, Direct and Inverse Problems of Electromagnetic and Acoustic Wave Theory (*DIPED*), Tbilisi, Georgia, 2018, Page(s):1 -4.

10.0 References

[1]. Tamir Klaff, Underwater Advanced Time-Domain Electromagnetic System , MR-201313 PI- Tamir Klaff, Tomas Bell, Empirical Investigation of the Factors Influencing Marine Applications of EMI –MR-2409

[2]. Stephen Billings and S. Lin-Ping, SERDP-Project # MR-2412: "Determining Detection and Classification Potential of Munitions Using Advanced EMI Sensors in the Underwater Environment" Final report.

[3]. Barry Spargo, SERDP-Project MR-2500: Effects of Target Corrosion on Advanced EMI Signatures in Underwater Environments.

[4]. Mr. Jonathan Miller, ESTCP Project# MR-201614 "Underwater Dynamic Classification Technology"

[5]. Barry Spargo, ESTCP Project# MR-201610 "Underwater EMI Sensor Platform for Metallic Item Detection".

[6]. H. Frank Morison "Development and Testing of an Engineering Prototype for a Marine Version of the Berkeley Unexploded Ordnance Discriminator (BUD): Phase II", SERDP Project MR-2321 Final Report;

[7]. T . Bell ," Empirical Investigation of the Factors Influencing Marine Applications of EMI", SERDP MR-2409, https://www.serdp-estcp.org/Program-Areas/Munitions-Response/Munitions-Underwater/MR-2409/MR-2409.

[8]. F. Morrison, "Development and Testing of an Engineering Prototype for a Marine Version of the Berkeley Unexploded Ordnance Discriminator (BUD): Phase II, SERDP MR 2321, https://www.serdp-estcp.org/Program-Areas/Munitions-Response/Munitions-Underwater/MR-2321/MR-2321.

[9]. D. Steinhurst "Marine Towed Array for Advanced Geophysical Classification" . SERDP-STCP Webinar series. https://www.serdp-estcp.org/content/download/46104/429252/file/SERDP%20ESTCP%20Webinar%2064%20(MR%2011022017).pdf)

[10]. F. Shubitidze, K. O'Neill, S. A. Haider, K. Sun, and K. D. Paulsen, "Application of the method of auxiliary sources to the wide-band electromagnetic induction problem", *IEEE Transactions on Geoscience and Remote Sensing*, vol. 40, No. 4, pp. 928–942, Apr. 2002.

[11]. F. Shubitidze, K. O'Neill, K. Sun, K. D. Paulsen, "Investigation of broadband electromagnetic induction scattering by highly conductive, permeable, arbitrarily shaped 3-D objects", *IEEE Transactions on Geoscience and Remote Sensing*, vol. 42, pp. 540–555, Mar. 2004.

[12]. F. Shubitidze, K. O'Neill, K. Sun, I. Shamatava, and K.D. Paulsen, "A hybrid full MAS and combined MAS-TSA algorithm for broadband electromagnetic induction problem", *Applied computational electromagnetic society Journal*, pages: 112-126, March, 2004.

[13]. S.H. Ward and G.W. Hohmann, *"Electromagnetic methods in applied geophysics"*. Volume 1, Theory, Edited by Misac N. Nabighian. SEG, 2008.

[14]. F. Shubitidze, "EMI modeling for UXO detection and discrimination underwater", SERDP Project MR-1632 Final Report.

[15]. O'Neill, K., [Discrimination of Subsurface Unexploded Ordnance], SPIE Press, Bellingham, Washington (2016).

[16]. F. Shubitidze, "EMI modeling for UXO detection and discrimination underwater", SERDP Project MR-1632 Final Report.
[17]. F. Shubitidze, J. P. Fernández, B.E. Barrowes, I. Shamatava, A. Bijamov, K. O'Neill, D. Karkashadze, " The orthonormalized volume magnetic source model for discrimination of unexploded ordnance", *IEEE Transactions on Geo-Science and Remote Sensing, Digital Object Identifier 10.1109/TGRS.2013.2283346*.
[18]. A. Bijamov, J. P. Fernández, B. E. Barrowes, I. Shamatava, K. O'Neill, and F. Shubitidze "Camp Butner Live-Site UXO Classification using Hierarchical Clustering and Gaussian Mixture Modeling", IEEE Transactions on Geo-Science and Remote Sensing, Digital Object Identifier 10.1109/TGRS.2013.2287510
[19]. S. Cazares, M. Tuley, and E. Ayers, "The UXO Classification Demonstration at Former Camp Butner, NC," 2011 [Online]. Available: http://serdpestcp.org/content/download/12777/151554/version/1/file/IDA_Camp+Butner_Report_1-13.pdf.
[20]. T. M. Grzegorczyk, B. E. Barrowes, F. Shubitidze, J. P. Fernández, and K. A. O'Neill, "Simultaneous identification of multiple unexploded ordnance using electromagnetic induction sensors," *IEEE Transactions on Geoscience and Remote Sensing* 49, 2507–2517 (2011).
[21]. J. Song, "Scattering of arbitrarily-polarized EM waves by a discontinuity in a grounded dielectric sheet and propagation of EM pulses excited by an electric dipole in conducting media," Ph.D. Dissertation, Dept. Elec. Eng., Michigan State Univ., East Lansing, Michigan, **1993**.
[22]. J. R. Wait, "A transient magnetic dipole source in a dissipative medium," *J. Appl. Physics.*, vol. 24, pp. 340-341, 1953.
[23]. K. S Yee, "Numerical solution of initial boundary value problems involving Maxwell's equations in isotropic media," IEEE Transactions on Antennas and Propagation, vol. 14, pp. 302–307, 1966.
[24]. Y. Yang, R. S. Chen, and Edward K. N. Yung, **"**The unconditionally stable Crank–Nicolson method for three-dimensional Maxwell's equations**",** Microwave and Optical Technology Letters, vol. 48, no. 8, August 2006.
[25]. A. Taflove, S. C. Hagness Computational Electromagnetics: the finite-difference time-domain method, 3rd ed, Artech house, 2005.
[26]. EMCoS," https://www.emcos.com/. [Online]. Available: https://www.emcos.com.
[27]. Kaufman, A. A. and Hoekstra, P., [Electromagnetic Soundings], Elsevier, Amsterdam (2001).
[28]. Zhdanov, Michael S., [Geophysical Electromagnetic Theory and Methods], Elsevier, Amsterdam (2009).
[29]. Sower, G.D., "Eddy Current Responses of Canonical Metallic Targets," Ch. 8, [Detection and Identification of Visually Obscured Targets], C.E. Baum (ed), Taylor & Francis Press, Philadelphia (1999).
[30]. O'Neill, K., [Discrimination of Subsurface Unexploded Ordnance], SPIE Press, Bellingham, Washington (2016).
[31]. Kong, J.-A., [Electromagnetic Wave Theory], Ch. 4, EMW Publishing, Cambridge MA (2005).
[32]. Carslaw, H.S. and Jaeger, J.C., [Conduction of Heat in Solids], Oxford Univ. Press, New York (2000).

[33]. Song, L.P., Billings, S.D.,Pasion, L.R. and Oldenburg, D., "Transient electromagnetic scattering of a metallic object buried in underwater sediments," IEEE. Trans. Geosci. Rem. Sens., 54(2), 1091-1102 (2016).

[34]. Shubitidze, F., O'Neill, K., Haider, S.A., Sun,K. and Paulsen, K.D., "Application of the method of auxiliary sources to the wide-band electromagnetic induction problem," IEEE Trans. Geosci. Rem. Sens., 40(4), 928-942 (2002).

[35]. Shubitidze, F., O'Neill, K., Sun, K. and Paulsen, K.D., "Investigation of broadband electromagnetic induction scattering by highly conductive, permeable, arbitrarily shaped 3-D objects," IEEE Trans. Geosci. Rem. Sens., 43(3), 540-556 (2004).

[36]. Won, I., Keiswetter, D., Hanson, D., Novikova, E. and Hall, T., "GEM-3: a monostatic broadband electromagnetic sensor," J. Environ. Eng. Geophys., 2(1), 53-64 (1997).

[37]. Miller, J.T., Bell T.H., Soukup, J. and Keiswetter, D., "Simple phenomenological models for wideband frequency- domain electromagnetic induction," IEEE Trans. Geosci. Rem. Sens., 39(6), 1294-1298 (2001).

[38]. Wait, J. R., and Spies ,K . P., 1969, Quasi-static transient response of a conducting and preamble sphere, Geophysics, 34, Bo.5 789-792.

[39]. Thomson, D.J. & Weaver, J.T., 1975. The complex image approximation for induction in a multilayered earth, J. geophys. Res.,**80,** 123–129.

[40]. D. H. Boteler and R. J. Pirjola, "The complex-image method for calculating the magnetic and electric fields produced at the surface of the Earth by the auroral electrojet", Geophys. J. Int. (1998) **132,** 31–40.

[41]. S. G. Shepherd and F. Shubitidze, "Method of auxiliary sources for calculating the magnetic and electric fields induced in a layered earth", *Journal of Atmospheric and Solar-Terrestrial Physics*, volume 65, issue 10, pages: 1151-1160, July 2003.

[42]. J. R. WAIT and D. A. HILL, Transient magneticfieldsprodueedby a step-function excited loop buried in the earth, Elect. Letrs.8 (11), 294-295, 1972.

[43]. Newman, G. A., G. W. Hohmann, and W.L. Anderson, "Transient electromagnetic response of a three-dimensional body in a layered earth", GEOPHYSICS, VOL. 51, NO.8 (AUGUST 1986); P. 1608-1627, 24.

[44]. Boyce, R.E., "Electrical resistivity, sound velocity, thermal conductivity density porosity, and temperature, obtained and laboratory techniques and well logs: site 462 in the Nauru basin of the Pacific Ocean" Deep Sea Drilling Project, Volume 61, Scripps Institution of Oceanography, La Jolla, California.

[45]. L. R. Pasion and D. W. Oldenburg, "A Discrimination Algorithm for UXO Using Time Domain Electromagnetics," *Journal of Environmental and Engineering Geophysics*, vol. 6, pp. 91-102, 2001.

[46]. F. Shubitidze et al., "A complex approach to UXO discrimination: Combining advanced EMI forward models and statistical signal processing," SERDP MR-1572 Final Report, January 2012.

[47]. F. Shubitidze, J. P. Fernández, B.E. Barrowes, I. Shamatava, A. Bijamov, K. O'Neill, D. Karkashadze, " The orthonormalized volume magnetic source model for discrimination of unexploded ordnance", *IEEE Transactions on Geo-Science and Remote Sensing, Digital Object Identifier 10.1109/TGRS.2013.2283346*